CHARACTERIZATION OF POLYMER/CLAY NANOCOMPOSITES

by

VLADIMIR SHAPOVALOV

A dissertation submitted to the Graduate Faculty in Physics in partial fulfillment of the requirements for the degree of Doctor of Philosophy, The City University of New York

2003

UMI Number: 3075763

UMI Microform 3075763

ProQuest Information and Learning Company
300 North Zeeb Road
P.O. Box 1346
Ann Arbor, MI 48106-1346

This manuscript has been read and accepted for the Graduate Faculty in Physics in satisfaction of the dissertation requirement for the degree of Doctor of Philosophy.

11/25/02
Date

Steven A. Schwarz, Chair of Examining Committee

11/26/02
Date

Sultan Catto, Executive Officer

Miriam H. Rafailovich

Jonathan C. Sokolov

Alexander A. Lisyansky

Nan-Loh Yang

Supervisory Committee

THE CITY UNIVERSITY OF NEW YORK

Abstract

CHARACTERIZATION OF POLYMER/CLAY NANOCOMPOSITES

by

Vladimir Shapovalov

Adviser: Professor Steven Schwarz

In this dissertation a new method of physical characterization of nanolayers and nanocomposites in polymers at engineered interfaces has been developed. The method allows to determine fraction of the volume occupied by nanoparticles in polymer nanocomposites and homogeneity of their distribution and to investigate the filler crystal orientation in the volume of polymer matrix.

It is shown that filler crystals can be oriented in a polymer by means of hydrostatic extrusion. The angular dependence of the Fe^{3+} EPR spectrum in the polymer/kaolinite nanocomposite has been for the first time investigated. A preferred direction of the kaolinite-plate orientation is observed, made visible by the direction of maxima in the angular dependence of the resonance field of EPR spectral lines.

Research was conducted on determining the main experimental parameters affecting the thickness of nanocomposite films in order to develop a technique of creating nanocomposite films with preset parameters.

The dependence of spin-cast polystyrene film thickness on silicon substrates is examined as a function of concentration (in toluene) and molecular weight with the help of SIMS analysis. For very dilute concentrations, atomic force microscopy reveals that the films break up into a uniform distribution of voids or islands with submicron dimensions.

The effects of solute concentration (in toluene), spin rate and the time of spinning on polystyrene/clay nanocomposite film thickness were examined. For uniform films ranging in thickness from 0.2μm to 10μm, thickness follows a power-law dependence on spin rate and on spinning time. The relative influence of viscosity and evaporation rate on the final nanocomposite film thickness was examined. A simple numerical model

for nanocomposite film thickness prediction was developed.

Acknowledgements.

It is a great pleasure for me to express my gratitude to the people without whose influence and help this work would not have come to its fruition. First and foremost to my supervisor Prof. Steven Schwarz, who had the patience to guide me through all the efforts and challenges, remaining my good friend and a true mentor in life and science. I have special gratitude towards Prof. Miriam Rafailovich who constantly supplied me with fresh and fruitful ideas and advice. It gives me a great pleasure to thank Prof. Nan-Loh Yang for his great help and valuable comments. I thank wholeheartedly Prof. Jonathan Sokolov for a constant keen interest in my research and invaluable help in conquering the fundamentals of polymer physics. A hart felt thank to Prof. Alexander Lisyansky whose invaluable help and advice have sustained me along the way. My first graduate adviser Prof. Narciso Garcia will always stay in my heart for his precious support during the first stages of my Ph.D. studies. He was the one who introduced me to the group that later became the core of the NSF Center named after him. I thank Dr. Vladimir Zaitsev for all the time we spent together in long intellectual discussions and during short 'socializing' breaks. It was a joy to work next to my peers and co-authors Yuri Strzhemechny, Kungang

Zhou, Faiqa Choudhery, Sandhu Bhupinder, and Maryana Isakova. I must mention the name of Don van Duyne from Livsey Analytical, Inc. for all the wisdom he shared with me about hi-tech machinery for surface science.

This work was supported in part by the National Science Foundation, grant NSF/MRSEC-DMR-9632525.

Preface.

The term "nanocomposites" is used to describe materials in which one phase is dispersed in the second phase and one of its dimensions is in a nanometer range. There are two main types of nanocomposites studied in materials science: ceramics nanocomposites and polymers nanocomposites. We will consider only nanocomposites based on polymers. Addition of clay to polymers produces dramatic improvements of mechanical properties, barrier properties and thermal resistance. Such changes are controlled by relatively small amounts of added clay and are of great interest for science and industry. The variety of applications includs structural materials, high-performance coatings, auto parts, deodorizers, catalysts, electronics, photonics, and magnetic and biomedical materials. Surface coating alone presents a huge area for research and applications. The main efforts in research of coatings are concentrated on understanding of various parameter controlling film properties and how these parameters can be controlled in practice. Such research is the main direction of efforts for our Surface Studies Laboratory.

The structure of this graduate research implements a new National Science Foundation paradigm for graduate education and research within

the framework of the Garcia Center for Polymers at Engineered Interfaces. The Center is a collaboration of academic, industrial, and government laboratories funded by the National Science Foundation as part of its Materials Research Science and Engineering Center (MRSEC) program. In graduate education the Center pursues the stated NSF goal to develop a "new paradigm for training graduate students" in order to "meet the need for a cadre of broadly prepared Ph.D.s with multidisciplinary backgrounds and the technical, professional, and personal skills essential to addressing the varied career demands of the future." Since polymer science, and especially composite materials design, is an intrinsically interdisciplinary field which relies heavily on close collaboration between faculty in diverse disciplines and with industry, the MRSEC combines the instrumentation and expertise of the participating institutions into a coordinated research program on polymer interface science and creates problem oriented teams of experts, with complementary areas of expertise, who work together towards a common goal. This collaboration of the faculty extends to the graduate

students and shows that it is possible to produce a coordinated set of PhD theses in different disciplines with interrelated results, each thesis documenting and demonstrating how the science is enhanced through collaboration.

According to this concept the graduate research included but was not limited to the following experimental techniques: Secondary Ion Mass Spectrometry (SIMS, Queens College of CUNY-based), ellipsometry (CUNY-based and SUNY-based), X-ray reflectivity (Brookhaven National Laboratory-based), Electron Paramagnetic Resonance (EPR, College of Staten Island of CUNY-based, and equipment of our Ukrainian collaborators), Atomic Force Microscopy (AFM, SUNY-based and CUNY- based). The research concentrates on characterization of nanoparticle-filled polymers (nanocomposites) and nanolayers and their effect on properties of polymer interfaces. The logic of development of the research was the following. First, a new (SIMS-based) method of measuring thickness and surface coverage for nanolayers was developed and applied to an investigation of

nanostructure formation in ultrathin spin-cast films. There are several reasons for development of a SIMS-based method for measuring thickness. Standard ellipsometry method does not work well for nanocomposites since the films are not transparent. In addition, if the film is thick, ellipsometry does not measure it reliably even if it is transparent, since ellisometry gives multiple results for the measured thickness and requires a knowledge of approximate film thickness from other methods. Although it is not an obstacle for thin films, it becomes a definite obstacle for thick films measurements. Nanostructure formation in spin-cast polystyrene films was researched for the purposes of development of the method. Second, the SIMS method was developed further to investigate fraction of the volume occupied by nanoparticles in polymer nanocomposites and homogeneity of their distribution in the nanocomposite. In this stage the developed SIMS-based method showed that (a) particles of the filler turn depending on different technological conditions of sample preparation even in a nanoscale-thin composite film, (b) iron ions are present in the filler clay particles as an impurity.

These two results led to a search for an additional experimental method capable of characterization of orientation of clay particles in the nanocomposite. A new EPR-based method has been developed for this purpose. In the third stage the SIMS method was developed to further investigate and characterize the fraction of volume occupied with filler nanoparticles, size, orientation, and space distribution of the filler particles. In order to produce coatings with controllable parameters, we applied a variety of other techniques for research of role for evaporation and viscosity in the process of a coating formation from a solution. Our research shows that control over these two parameter brings control over the final films thickness.

Physical studies of nanostructures and nanocomposites in polymers at engineered interfaces is a rather urgent field of investigation. By the middle of the 80-ies the investigation of the properties of nanomaterials was developing rapidly as described in articles [1-4]. A method for producing nanomaterials was proposed by Gleiter H. [1]. In USA, this method was rather fruitfully applied by Siegel R. et al [3,4].

A distinctive feature of nanomaterials is the small in size crystals and phases as a structural basis. In this respect, much of the bulk is within a few gyration radii of a nanoparticle boundary. That's why our nanomaterials are of high structural sensitivity under various external influences exerted in this work.

The targeted topic is relatively fresh in view of both fundamental and applied aspects. Polymers are currently a place of extraordinary importance in everyday life. Their many fascinating properties are being extensively explored and utilized, yet still many issues remain open.

We used SIMS to investigate the behaviour of clay particles in thin polymer films. The results of preliminary measurements have shown that in such films the clay particles turn as a result of different influences (for example, after annealing). Besides, there were a number of uncertain questions, in particular, to what extent the clay particles are ordered in the investigated samples. The problem on the clay particle ordering and their diffusion into the polymer turned out to be so complex that it could not be solved by SIMS methods. So, we had to use additional methods

and investigations that are described below.

The investigated problem is of high scientific and engineering importance. For example, the investigation of the problem will help in the improvement of quality and lowering the cost of tires, etc.

The dissertation consists of the Introduction, Acknowledgements, Contents, List of Figures, seven Chapters and the Conclusion.

The first chapter describes experimental procedures: Secondary Ion Mass Spectrometry experimental technique and SIMS and TOF SIMS spectra, and experimental procedures for EPR studies of polymers.

The investigations described in the second chapter have resulted from a necessity of measuring the thickness and physical properties of ultrathin polymer films. With this purpose we have used the SIMS method to quantify sub-monolayer film coverage.

The third chapter develops the topic of the second chapter into a research of nanocomposite spin-cast film formation process, a problem of great importance for industrial applications.

The fourth chapter describes the current state of the problem of

model systems with the multiminimum potential. The EPR-spectrum of Cu^{2+}-ion in $LiGa_5O_8$-crystal was investigated at $\nu = 9.2407$ GHz and $\nu = 37.15$ GHz over a temperature range of 4.2 - 300 K. The parameters of the spin-Hamiltonian were received. The character of the temperature dependence of the integral intensity of both the anisotropic and isotropic spectra were studied. The distribution of static deformations of crystal were detected. The temperature dependence of the integral intensity of the isotropic EPR spectrum of Cu^{2+}-ion was manifested. On the basis of the dynamic cluster model of the Jahn-Teller effect the spin Hamiltonian parameters were calculated and the analysis of obtained experimental results was carried out. It was shown that the tunnelling splitting for Cu^{2+}-ion in $LiGa_5O_8$-crystal is smaller than 0.005 cm^{-1}. The obtained results lead to the conclusion that the mechanism of temperature variation of the EPR-spectrum due to population of excited vibronic states is sufficiently effective for $LiGa_5O_8$-crystals.

The fifth chapter describes the current state of the problem of filled polymers. A method of preparing samples used in the experiment is

given. A method of obtaining filler crystal orientation and techniques used to analyse the character and degree of orientation are described.

The sixth chapter gives the results of investigations of temperature-induced change of the EPR spectrum of the Fe^{3+} ion, which is the magnetic probe in kaolin-clay. The observed properties of the temperature dependence of the EPR spectrum are characteristic of systems with a multiminimum potential.

The seventh chapter gives the results of investigations of orientation of kaolinite crystal plates in ultrahigh-molecular polyethylene (UHMPE) induced by solid-phase extrusion by means of the X - ray diffraction and EPR spectroscopy methods. The obtained results allow us to conclude that the solid-phase extrusion results in the ordering of kaolinite plates in ultrahigh-molecular polyethylene.

Table of Contents

List of Tables

List of Figures

CHAPTER 1.

Experimental procedures.

§1. Secondary Ions Mass Spectrometry experimental technique and SIMS and TOF SIMS spectra.

1.1. Experimental procedures for SIMS and TOF SIMS studies of polymers.

The idea of Secondary Ion Mass Spectrometry is to induce emission of charged species (individual atomic ions and ionized clusters) from the surface under study by bombarding it with a beam of primary ions. The ejected secondaries are then discriminated over a wide range of masses inside a mass analyzer. The analysis may be performed in either static (the surface properties remain almost unaltered after bombardment), or dynamic mode (the material of the sample is being continuously sputtered away, revealing with time new subsurface layers). Although there exists a variety of different schemes of producing primary ion flow, a lot of ways to excite secondary ions from the surface, as well as a number of basic designs for a mass filter, all of them are incorporated into a general term - SIMS. SIMS finds extensive

use in many fields of materials science, with parts per billion sensitivity, high (<100A) depth resolution, decent (<1μm) lateral resolution, the ability to detect almost all elements and to be operated in different regimes (mass spectrum, depth profile, surface mapping, etc.). The most common types of mass analyzers employed in SIMS instruments are the magnetic sector, quadrupole, and TOF (Time-Of-Flight). In magnetic sector instruments, secondary ions enter a region with a magnetic field where their trajectories are split by the Lorentz force due to a difference in masses. The quadrupole mass detector employs filtering of particles' distance flown due to a combination of AC and DC electric fields applied inside of a four-rod configuration. TOF technique separates simultaneously emitted secondaries by the time they spend between emission and detection. All ions are initially given approximately the same kinetic energy, allowing lighter species to be detected ahead of the heavier ones.

At the present time dynamic SIMS finds increasing use in studies of polymer surface behavior [1, 2]. We operate the following instruments: "Atomica 3000-30 ion microprobe" and "Ion-ToF ToF SIMS IV".

In articles [1, 2] we describe the experimental technique and factors which affect resolution and quantitation. An Atomika 3000-30

ion microprobe was employed in these studies. For maximum depth resolution in polymers, optimal technological parameters were determined.

Dynamic secondary ion mass spectrometry (SIMS) has recently been employed to obtain high resolution depth profiles in polymer blend thin films and is now regarded as a key probe of surface and interfacial segregation in these systems [3].

Dynamic SIMS is employed at dozens of laboratories, worldwide, for diverse studies in the fields of microelectronics, metallurgy, geology and biology [4].

SIMS is demonstrated to occupy an important niche in the arsenal of spectroscopies for thin film polymer profiling. The key attributes of the technique are high depth resolution (~10nm), high sensitivity, simultaneous detection of multiple species, and ease of analysis and interpretation.

In the dynamic SIMS mode, selected secondary ions are monitored as a function of sputtering time, yielding a concentration vs. depth profile. The primary beam is typically rastered over a distance several times the beam focal width, forming a flat bottomed crater. Only ions emitted from the central region of the crater are detected, so as to

avoid a crater-edge contribution to the depth profile. Secondary ion intensities are influenced by the matrix (chemical environment), by the concentration of implanted primary ions, by sample charging during analysis, and by instrument instabilities. Depth resolution is degraded by bombardment induced mixing and knock-in of sample atoms, by surface roughening, and by enhanced diffusion or segregation effects. The depth scale may also be affected by beam instability and variations in sample composition.

In the present studies, a 2keV 20 nA Ar^+ beam at 30° off-normal incidence is typically employed [2]. The focal width of the 20 nA beam is ~0.1 mm and the beam is rastered over a 0.5 mm square region with ions accepted from a 0.15 mm square region in the center of the sputtered crater. These conditions yield a sputtering rate of ~1nm min^{-1} with a depth resolution of ~10nm in PS films [6]. Sputtering at off-normal incidence enhances the erosion rate and consequently improves the depth resolution. Ar bombardment is employed so as to minimize the effect of primary ion concentration on sensitivity. The Ar beam current in the instrument employed (an Atomika 3000-30 ion microprobe) is also stable to within 5% per day, due to feedback control of the source discharge current, which therefore allows for long

overnight analyses. Ar bombardment also reduces the probability of molecular interferences and allows the detection of oxygen (O) in the film. Negative ion detection is employed, with high sensitivity to species such as H, D, C, O, fluorine (F) and bromine (Br). N^- and N^+ species are undetectable; however, CN^- is readily detectable. In the positive ion mode, the D^+ signal suffers from a severe H^{2+} interference.

The sputtering yield behavior [3] indicates, for 30° incidence, a maximum yield in the 5-10keV energy range. At normal incidence, the maximum occurs at a significantly lower energy. This angular dependence is well known for secondary electron yields [7] and has a similar physical origin. The low energies at which these maxima occur are typical of light primary-light target combinations. The high yield values ($Y >> 1$) may suggest significant molecule emission or hydrogen liberation.

"ATOMIKA ADIDA 3000-30" is equipped with an ion gun, where the flux of primary ions may be extracted from a plasma of either oxygen or argon gas. These ions can then be accelerated to energies in the range 1 through 15 keV, focused and rastered across the surface of the sample. The sample is positioned on a carousel inside a main chamber with ultra-high vacuum conditions ($< 10^{-8}$ torr). The secondary

ionized species ejected from the sample are drawn into the secondary optics, followed by a quadrupole mass filter. The position of the sample relative to the detector opening can be adjusted by means of variation of the incline angle of a sample holder. An option of applying a constant voltage bias to the carousel stage is also available. An additional advantage in the setup is the presence of an electron gun that provides surface charge neutralization for samples while bombarded with primary ions. It has been found [2] that for most polymer species, a practical operation scheme is 2 keV 30°-off normal Ar^+ bombardment, which was primarily being employed throughout all the runs in this work.

Depth profiling is one of the operating modes of SIMS. The idea is to monitor the intensity of the secondary ions as a function of time. As the sputtering of the material proceeds (a beam of primary ions is rastered across a square area of about 1 mm^2) a crater is created. If, for some reason, a concentration of a certain element at the crater bottom is changing with depth it will show up as a distinct change of the yield with time. As a rule, depth scales with the time of sputtering. The dependence of the concentration vs. depth is the depth profile.

The observed charged secondaries can be atomic or molecular

(cluster) ions, both positive and negative. The choice of the masses to detect is based on a number of factors, empirical as well as fundamental. An important property of SIMS is the ability to distinguish between different isotopes of the same element. In conjunction with this, we shall mention that for polymers, isotope tagging (the most popular tag - a substitution of hydrogen with deuterium) opens almost unlimited experimental opportunities.

The SIMS technique involves certain difficulties though. The probability of ion formation is varying from element to element by orders of magnitude, thus making detection of some of them rather problematic. Also, there is an uncertainty in the species identification due to mass interference. For instance, ions of O_2 and S have the same mass 32 a.m.u., or CO and Si ions interfere at 28 a.m.u. Fortunately, there are ways to overcome these setbacks. TOF-SIMS detectors allow mass resolution well above the proton/neutron mass ratio, which effectively eliminates almost all the mass ambiguities. As far as the "ATOMIKA" instrument is concerned, it is equipped with an electron gun and a hemispherical energy analyzer. That provides an opportunity to run parallel energy detection of the secondary electrons. If the analyzer is tuned to the characteristic energies of the relevant Auger

peaks, another kind of depth profile (associated with the intensity of secondary electron flux) will be monitored. The two simultaneous runs - SIMS and Auger - complement each other. Another way of resolving mass detection ambiguities on the "ATOMIKA" is to apply a voltage bias to the stage. A change in the electric potential of the surface leads to a significant decrease in the escape probability for clusters, whereas for single atoms the ion yield is influenced only moderately.

At the crater edges, some signal uncertainty occurs due to a finite diameter of the ion beam. That may result in some unwanted background in the integrated yield. This problem of the edge effects is resolved by introducing electronic gating - the data is collected only in the central region of the crater.

When dielectric materials, polymers included, are treated in SIMS, they may gradually accumulate uncompensated charge. Usually it brings about an instability in the signal of secondaries - gradual decline alongside sharp jumps. But if an unfocused electron beam is directed into the vicinity of the crater, the surface may be effectively neutralized.

The materials studied have to be specially prepared. Polymer samples are thin mono- or multilayered films deposited onto a very smooth surface of a substrate (predominantly a Si wafer).

To get a film with desired qualities, a standard sample preparation routine is employed. First, a wafer is cleaved into relatively small pieces (ca. 1 cm^2, to fit a SIMS sample holder) Originally, the surface is covered with a native oxide layer, as well as some other contaminants. This fact alone can have a dramatic effect on the physical and chemical properties of the surface. If we wish to alter the attributes of the surface it has to be chemically processed. Relevant etching procedures are applied.

Polymers in a powder or granular state are dissolved in a solvent. Next, we spin cast our film from the polymer solution onto the surface of the wafer. The high rotation speed of a spinner spreads the droplet quickly as the solvent evaporates. As a result we have a smooth and rather uniform layer of the solute. The thickness of the layer obtained depends on many parameters, like concentration of polymer solution, time and speed of spinning, etc. Thus, we can easily adjust the desired thickness, which can be measured afterwards with an ellipsometer.

When preparing multilayered samples, spinning of the next film on top of the previous is usually not acceptable, since the solvent may destroy the interface between the two. Instead, the next layer is first spun on a piece of glass, and then floated in deionized water onto the

lower coating. With many polymeric solutions this standard procedure works fine.

Often, a thermal treatment of the samples is required. They are placed inside an evacuated (pressure ca. 10^{-2} Pa) oven for various times at certain fixed temperatures in the range above the glass transition temperature and below the decomposition temperature for the given polymers.

1.2. Experimental procedures for nanostructure formation in spin-cast polystyrene films.

The samples under investigation are, primarily, thin (tens to hundreds of nanometers) films of both common and specially synthesized polymers. These films and the wafers are treated in various chemical and thermal environments, and their properties are being monitored as a function of treatment parameters.

Deuterated polystyrene (MW=690,000,Polymer Source) and polystyrene (MW = 9,000 to 8,500,000, Polymer Laboratories) were used as received. For the dPS films, silicon (100) samples received a modified Shiraki etch [8] to produce a uniform hydrophobic surface. The PS films were

prepared on as-received silicon (100) samples. Toluene solutions of deuterated polysterene were spin cast at 2000 rpm for 30 sec, while the PS films were spin cast at 2500 rpm for 30 sec. For the relatively thick films, thickness was measured with a Rudolph AutoEl-II ellipsometer.

SIMS profiles employed a 2 keV 20 nA argon beam at 30° off-normal incidence, in an Atomika 3000-30 quadrupole ion microprobe. Negative secondary ions were monitored, permitting detection of D without concern for H_2 interference. A ~200 A thick PS layer was floated onto samples in de-ionized water, to obtain steady state sputtering conditions, while protecting the surface from contamination. The depth resolution of the SIMS technique (~100 A [2]) does not allow the thickness of ultrathin films to be accurately assessed. The parts per million sensitivity of the technique, however, allows trace remnants of dPS to be detected, as observed below. The deuterium signal was normalized to the carbon signal, and a thick dPS standard was employed for calibration of concentration. The SIMS technique employed here is described in reference [2]. The

integrated number of deuterium counts in the region of the silicon surface is converted to an equivalent film thickness, matching ellipsometer data for thick samples. The equivalent thickness is calculated assuming that the film is continuous everywhere. Thus, for uniform films the equivalent and the true thickness are equal while for non-uniform films (i.e., with voids or islands), the equivalent thickness is the thickness the sample would have if all its material were spread uniformly on the substrate. Atomic force microscopy was performed with a Digital Nanoscope IIIA in the contact mode, to obtain topographic and friction force images.

§2. Ellipsometry technique and experimental procedures.

The ellipsometer is an optical instrument measuring the changes in polarization of monochromatic polarized light reflected form a surface of interest. The comparison of the azimuth angles of polarization is performed for the incident and reflected beams. As a result, the information obtained allows a direct calculation of the real and imaginary part of the refractive index of the surface, and for the case of a reflective substrate covered with a transparent thin film, the thickness

of the film. The advantageous characteristics of ellipsometry are its high (fraction of a nanometer) thickness resolution, capability of determining the index of refraction of an unknown substance, and the ability to yield results in various environments, open air included.

The thin polymer samples we investigate are usually transparent and permit rather straightforward and precise ellipsometric measurements. When a depth profile is generated, and a certain interface is reached (e.g. the boundary between the film and the solid substrate), subsequent ellipsometry data can be used for the direct rescaling of the number of SIMS raster cycles needed to reach the interface. Throughout these studies we used the Rudolf Research AutoEL-II ellipsometer to obtain the depth scales of the profiled specimens.

When the surface is opaque for visible light, and ellipsometry cannot be used, we employ local cross-sectional mechanical profiling. The general term of this approach is surface profilometry. The studied surface with non-uniformities on it is being moved beneath a diamond-tipped stylus attached to a piezoelectric sensor. Surface variations translating the stylus vertically are recorded with high precision as the scan progresses. In such a manner the cross-section of the SIMS crater

can be restored and the SIMS data properly scaled. In our studies we used a Sloan profilometer, model "Dektak IIA".

§3. X-ray reflectivity technique and experimental procedures.

X-ray reflectivity(XR) was used to measure thickness of ultrathin polymer layers. Figure 1.1 shows the typical geometry used for XR. The z, x, y directions are defined by the normal to the sample surface, and the in-plane and out-of plane vector perpendicular to the z direction, respectively. The wavevector transfer, $\mathbf{q} = \mathbf{k_f} - \mathbf{k_i}$, with $\mathbf{k_f}$, $\mathbf{k_i}$, the incident and scattered wave vector respectively, was controlled by varying the incident (α_i) and exit (α_f) angles with $q_z = k(\sin\alpha_i + \sin\alpha_f)$. The mean value of the wave vectors **k** is given by $k = 2\pi / \lambda$. The specular reflectivity is defined as the intensity taken at $q_x=0$ as a function of q_z by varying α_i and α_f while maintaining $\alpha_i=\alpha_f$. Since the specular reflectivity detects the variation of the electron density $\rho(z)$ in the direction to surface normal, averaged in the (x,y)-plane, it is sensitive to the layer thicknesses (d), the density contrasts and the interfacial roughnesses (σ_1, σ_2) defined by the probability density.

The measurements were performed at beamline X10B, National Synchrotron Light Source, Brookhaven National Laboratory.

§4. Atomic Force Microscopy technique and experimental procedures.

The Atomic Force Microscope (AFM) is being used to solve processing and materials problems in a wide range of technologies affecting the electronics, telecommunications, biological, chemical, automotive, aerospace, and energy industries. The materials being investigating include thin and thick film coatings, ceramics, composites, glasses, synthetic and biological membranes, metals, polymers, and semiconductors. The AFM is being applied to studies of phenomena such as abrasion, adhesion, cleaning, corrosion, etching, friction, lubrication, plating, and polishing. By using AFM one can not only image the surface in atomic resolution but also measure the force at nano-newton scale. The publications related to the AFM are growing speedily since its birth.

The force between the tip and the sample surface is very small, usually less than 10^{-9} N. How to monitor such small forces is another story. The detection system does not measure force directly. It senses

the deflection of the microcantilever. The detecting systems for monitoring the deflection fall into several categories. The first device introduced by Binnig was a tunneling tip placed above the metallized surface of the cantilever. This is a sensitive system where a change in spacing of 1 A between tip and cantilever changes the tunneling current by an order of magnitude. It is straightforward to measure deflections smaller than 0.01 A. Subsequent systems were based on the optical techniques. The interferometer is the most sensitive of the optical methods, but it is somewhat more complicated than the beam-bounce method which was introduced by Meyer and Amer. The beam-bounce method is now widely used as a result of the excellent work by Alexander and colleagues. In this system an optical beam is reflected from the mirrored surface on the back side of the cantilever onto a position-sensitive photodetector. In this arrangement a small deflection of the cantilever will tilt the reflected beam and change the position of beam on the photodetector. A third optical system introduced by Sarid uses the cantilever as one of the mirrors in the cavity of a diode laser.

Motion of the cantilever has a strong effect on the laser output, and this is exploited as a motion detector.

According to the interaction of the tip and the sample surface, the AFM can be classified as repulsive or Contact mode and attractive or Noncontact mode. Now the Tapping mode shows a prosperous future to image the micro-world.

The principles on how the AFM works are very simple. An atomically sharp tip is scanned over a surface with feedback mechanisms that enable the piezo-electric scanners to maintain the tip at a constant force (to obtain height information), or height (to obtain force information) above the sample surface. Tips are typically made from Si_3N_4 or Si, and extend down from the end of a cantilever. The nanoscope AFM head employs an optical detection system in which the tip is attached to the underside of a reflective cantilever. A diode laser is focused onto the back of a reflective cantilever. As the tip scans the surface of the sample, moving up and down with the contour of the surface, the laser beam is deflected off the attached cantilever into a

dual element photodiode. The photodetector measures the difference in light intensities between the upper and lower photodetectors, and then converts to voltage. Feedback from the photodiode difference signal, through software control from the computer, enables the tip to maintain either a constant force or constant height above the sample. In the constant force mode the piezo-electric transducer monitors real time height deviation. In the constant height mode the deflection force on the sample is recorded. The latter mode of operation requires calibration parameters of the scanning tip to be inserted in the sensitivity of the AFM head during force calibration of the microscope. In our research we used a Digital Instruments Multi Mode Scanning Probe Microscope.

§5. Experimental procedures for EPR studies.

The electron paramagnetic resonance is the radio-frequency effect involving the quantum transitions between the energy levels of the paramagnetic ion spin multiplet in a static magnetic field. The transition energy is equal to the electromagnetic radiation quantum.

The EPR method enables one to determine the valency of magnetic

ions in a crystal lattice, the local symmetry of the crystalline field as well as the distortions of the cubic symmetry. Also, it can be used to specify the magnetic axes of paramagnetic ions, as well as the number of magnetically nonequivalent positions of ions and the character of their distribution in crystal lattice [9]. The EPR method makes it possible to directly observe the Jahn-Teller effect that is inaccessible to another investigation techniques.

The EPR spectrum intensity indicates the number of atomic carriers of magnetism. The g-factor anisotropy gives information on crystal-lattice symmetry.

A paramagnetic ion, being implanted into a crystal, is not free, it is under the action of the intracrystalline electric field. This field is conditioned by charges from its nearest neighbors whose electron densities partially overlap with the paramagnetic ion. The exact calculation of charge distribution is a problem of high difficulty. Therefore to interpret the EPR spectra of paramagnetic ions located in the crystal lattice the use is made of such approximations as the crystalline-field method and formalism of the spin Hamiltonian.

A general theory of the EPR spectra in crystals has been developed by Abraham A and Pryce H.M.L. [10, 11]. A rather good relation

between theory and experiment is realized by using a spin Hamiltonian, which is a reduced form for writing down the interaction energies for the paramagnetic ion. If the symmetry of the crystalline field and the electronic configuration of the ion are known, the interaction energies could be found. In practice, the reverse problem is usually solved. By using the experimental constants, real energy levels of the paramagnetic ion in the ground state are restored.

The experimental procedure and tecnique of measurement of the EPR spectra are specified by the physical problem. For a successful solution of the problem a number of requirements as to experimental setup should be met. For investigation of the EPR spectra the requirements are:

1. selection of the operation frequency;

2. stable magnetic field smoothly varying from zero to the maximum which is needed for the principal resonance condition (in the case of S=1/2: $h\nu = g\beta H$);

3. sensitivity and resolution of the setup;

4. a possibility of performing the experiment in a wide temperature range (T = 4.2-300K) under many-hour measurements;

5. stable operation of the equipment should provide reproducibility

and reliability of the results.

The EPR spectra were investigated by using an X-band radiospectrometer. For orientation of the magnetic axes the resonator has a device for rotation of the samples and a limb to read the angles. A sample is pasted onto a rotating table at point of the maximum vertical microwave magnetic field H_1. Since under rotation of the magnet the constant magnetic field H_0 is of horizontal direction, the condition of $H_1 \perp H_0$ is always met.

Prior to making measurements of the EPR spectrum it is necessary to adjust the radio spectrometer for the maximum sensitivity and stability. The measurement is made of the following quantities:

1. microwave generator frequency;

2. the resonance values of the magnetic field with which the EPR lines are observed;

3. the angle between the magnetic axis of the crystal and magnetic field direction. These quantities are measured to a definite accuracy.

Directions of magnetic axes of the crystal are determined during the rotation of the sample and electromagnet. An error in setting the angle by this method is not in excess of 1^0. Such error results in a change of EPR spectrum position with respect to the field within the limits of 0.2-

1.0 Oe. The largest error occurs under the measurement of the resonance magnetic fields, since the sample and the magnetic field transducer are located in different fields because of magnetic field non-uniformity. The difference in the measured magnetic fields can be controlled by comparing the measured magnetic field and the field calculated by the frequency of a signal klystron for a well-known substance.

One can't start identifying the spectrum and writing the spin Hamiltonian down if the type of the local symmetry of the electrical crystalline field is not known. The type of the crystal field symmetry is determined from the angular dependence of the EPR spectrum. This is the dependence of positions of spectral resonance lines on angles. These are the angles between directions of the constant magnetic field H and magnetic axes X, Y and Z. The system of three magnetic axes X, Y and Z is always orthogonal in contrast to the system of crystallographic axes.

When studying the angular dependence of the EPR spectrum one can find such an extreme position of the spectrum by two angles (φ and θ), when the distances between spectrum components will be maximum. Such extreme orientation, along which the magnetic field H_0

most frequently influences the splitting of energy levels, is generally called the Z-orientation. With a fixed Z-axis, the X- and Y-axes are adjusted to a maximum possible accuracy by turning φ and θ through an angle of 90°.

§6. References

1. S.A. Schwarz, R.A.L. Jones, E.J. Kramer, M.H. Rafailovich, and J.C. Sokolov. SIMS depth profiling study of surface enrichment in blends of deuterated and protonated polystyrene. In book Proceedings of the Seventh International Conference on Secondary Ion Mass Spectrometry (SIMS VII). P.P.355-358 (1989).

2. S. A. Schwarz, B. J. Wilkens, M. A. A. Pudensi, M. H. Rafailovich, J. Sokolov, X. Zhao, W. Zhao, X. Zheng, T. P. Russell, R. A. L. Jones. Studies of surface and interface segregation in polymer blends by secondary ion mass spectrometry. Molecular physics, Vol. 76, No. 4, 937-950 (1992).

3. E. J. Kramer. Physica B, Vol. 173, 189 (1991).

4. P. J. Mills, P. F. Green, C. J. Palmstrom, J. W. Mayer and E. J. Kramer. Appl. Phys. Lett., Vol. 45, 958 (1984).

5. J. Sokolov, M. H. Rafailovich, R. A. L. Jones and Kramer. Appl. Phys. Lett., Vol. 54, 590 (1989).

6. S. K. Sinha. Physica B, Vol. 173, 25 (1991).

7. R. Chujo. Polym. J., Vol. 23, 367 (1991).

8. Y. M. Strzhemechny, S. A.; Schwarz, J. Schachter, M. H. Rafailovich, J. Sokolov. Secondary Ion Mass Spectrometry Study of Silicon Surface Preparation and the Polystyrene/Silicon Interface *J. Vac. Sci. Technol.*, A 15: 894-898 (1997).

9. Abragam A. and Bleaney B. Electron Paramagnetic Resonance of Transitions Ions. Clarendon Press, Oxford (1970).

10. Pryce H.M.L. Proc. Phys. Soc., A63, 25 (1950).

11. Abragam A. and Pryce H. M. L. Proc. Phys. Soc., A205, 135 (1951).

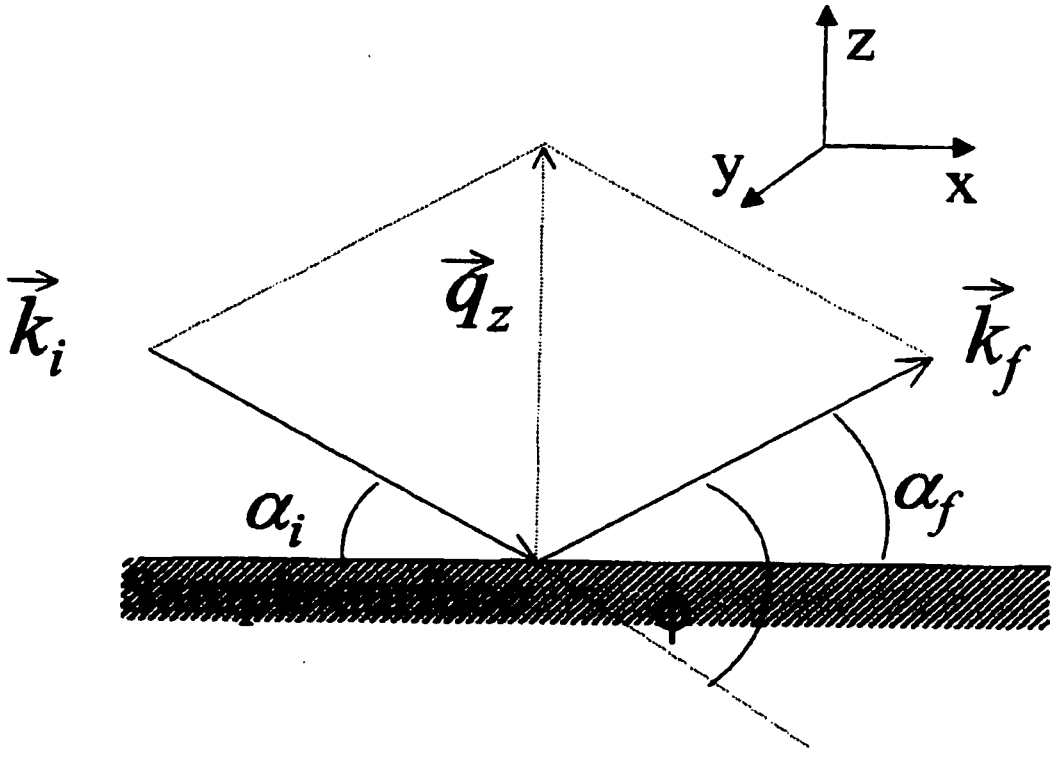

Figure 1.1. The scattering geometry of the x-ray reflectivity experiments. The momentum vector transfer is defined by $\mathbf{q_z}=\mathbf{k_f}-\mathbf{k_i}$ where $\mathbf{k_i}$ and $\mathbf{k_f}$ are the wave vectors of the incident and the reflected electro-magnetic waves respectively.

Chapter 2

Nanostructure Formation in Spin-Cast Polystyrene Films.

§1. Introduction.

The investigations described in this chapter have resulted from a necessity of measuring the thickness and physical properties of ultrathin polymer films. With this purpose we have used the SIMS method and have developed a novel method of investigation.

The dependence of spin-cast polystyrene film thickness on silicon substrates is examined as a function of concentration (in toluene) and molecular weight. For uniform films ranging in thickness from 100 Å to 1 μm, thickness follows a power law dependence on concentration, with the power varying from 1.25 at low molecular weights, to greater than 2 at the highest molecular weights examined. For very dilute concentrations, atomic force microscopy reveals that the films break up into a uniform distribution of voids or islands with submicron dimensions, as has been observed previously. The apparent film thickness (at molecular weight 690,000), is determined by secondary ion mass spectrometry, and is found to vary linearly with concentration for film thicknesses below ~30 Å, the thickness at which the film begins to

break up. At this molecular weight, X-ray reflectivity results indicate that the limiting thickness of the remnant polymer regions is ~30 Å. Effects of annealing are also investigated.

Numerous studies address the properties of thin polymer films prepared by the spin-casting technique [1-3], and some recent articles have examined very thin polymer films (less than 100 Å) which break up into uniform distributions of polymer islands and voids [4,5]. The present study was undertaken to examine the thickness and morphology of polystyrene (PS) films spin cast onto silicon from a wide range of solution concentrations, employing secondary ion mass spectrometry (SIMS), atomic force microscopy (AFM), ellipsometry, and X-ray reflectivity to monitor thickness and surface morphology. The effect of molecular weight on the thickness of uniform films is examined. By employing deuterated polystyrene (dPS) solutions, SIMS can be utilized to detect trace amounts of remnant polymer on the silicon surface. AFM, SIMS, and X-ray reflectivity studies indicate that, at a dPS molecular weight of 690,000, the films approach a limiting thickness of approximately 30 Å, and then develop

holes, or microvoids, with diameters on the order of 0.1 μm. Silicon is exposed within these microvoids. Spin casting represents an economical and straightforward means of creating such a nanostructured film.

§2. Experimental.

Deuterated polystyrene (MW=690,000, Polymer Source) and polystyrene (MW = 9,000 to 8,500,000, Polymer Laboratories) were used as received. For the dPS films, silicon (100) samples received a modified Shiraki etch [6] to produce a uniform hydrophobic surface. The PS films were prepared on as-received silicon (100) samples. Toluene solutions of deuterated polysterene were spin cast at 2000 rpm for 30 sec, while the PS films were spin cast at 2500 rpm for 30 sec. For the relatively thick films, thickness was measured with a Rudolph AutoEl-II ellipsometer.

SIMS profiles employed a 2 keV 20 nA argon beam at 30° off-normal incidence, in an Atomika 3000-30 quadrupole ion microprobe. Negative secondary ions were monitored, permitting detection of D without concern for H_2 interference.

A ~200 Å thick PS layer was floated onto samples in de-ionized water, to obtain steady state sputtering conditions, while protecting the surface from contamination. The depth resolution of the SIMS technique (~100 Å [7]) does not allow the width of ultrathin films to be accurately assessed. The parts per million sensitivity of the technique, however, allows trace remnants of dPS to be detected, as observed below. The deuterium signal was normalized to the carbon signal, and a thick dPS standard was employed for calibration of concentration. The SIMS technique employed here is described in reference [7]. The integrated number of deuterium counts in the region of the silicon surface is converted to an equivalent film thickness, matching ellipsometer data for thick samples. The equivalent thickness is calculated assuming that the film is continuous everywhere. Thus, for uniform films the equivalent and the true thickness are equal while for non-uniform films (i.e., with voids or islands), the equivalent thickness is the thickness the sample would have if all its material were spread uniformly on the substrate. Atomic force microscopy was performed with a

Digital Nanoscope IIIA in the contact mode, to obtain topographic and friction force images.

§3. Results.

A power law dependence of PS film thickness on polymer concentration, measured by ellipsometry over a range of molecular weights, is demonstrated in Fig.2.1. The slopes of the least-square fits vary from 1.26 (MW = 9,000) to 2.10 (MW = 8,500,000). The dependence of film thickness on rotation speed and solvent evaporation rate is described elsewhere [3, 4, 8]. SIMS depth profiles of several films, each covered by a protective PS overlayer, are illustrated in Fig. 2.2. As a control, a sample treated with pure toluene was also examined and is shown in the figure. The integrated area under the interfacial deuterium peaks is easily converted to an apparent film thickness, and for the thinnest film examined, the signal to noise ratio is still high. Equivalent film thicknesses at each concentration are shown as a function of solution concentration in Fig.2.3. The thickness of the 2 and 4 mg/ml samples were determined by SIMS and by ellipsometry. The thickness of the 10 and 20 mg/ml samples

were determined only by ellipsometry. Experimental errors arise primarily from processing variations, rather than counting statistics. The slope of the least-squares fit to the data (excluding the two highest concentrations) is 1.0, indicating a linear dependence of equivalent thickness on concentration. At higher concentrations, the thickness varies approximately as the 1.5 power of the concentration, consistent with the results of Fig. 2.1. The overlap concentration of PS at molecular weight 690,000 is approximately 1 mg/ml [9]. The change in slope (from 1.0 to 1.5) appears to occur near this concentration, where the solutions are changing from the dilute to the semi-dilute regime. This change in slope occurs at a thickness below the radius of gyration, comparable to the thickness (~30 Å) at which the film begins to break up.

Figures 2.4a, 2.4b, and 2.4c show AFM topographic and friction force images at concentrations of 2.0, 0.4, and 0.0002 mg/ml respectively. The film illustrated in figure 4a has a uniform thickness of 103 Å, as determined by SIMS, and displays a surface roughness on the order of 5 Å, with no visible contrast in the friction force image.

Microvoids of approximately 0.1 μm in diameter are observed for film prepared with 0.4 mg/ml polymer solution. The high contrast in the friction force image indicates that silicon is exposed within the voids. The scans of height variation across these surfaces show polymer regions with a uniform thickness of ~30 Å, much less than the radius of gyration of ~200 Å [10].

The limiting thickness determined by AFM is consistent with X-ray reflectivity measurements performed at the Brookhaven NSLS facility, which yielded thicknesses of 33 Å and 20 Å, for concentrations of 0.04 mg/ml and 0.0002 mg/ml respectively (see Fig. 2.5). X-ray reflectivity results indicate that the refractive indexes of all three films in Fig. 2.5 are within 1% of each other, and within 5% of the measured bulk for PS. The illustrated curve at a concentration of 4 mg/ml indicates a thickness of 238 Å, consistent with the ellipsometer measurement of 220 Å.

At the most dilute concentration examined here, the film has undergone a transition from voids to islands. Ring-shaped structures were observed in films prepared at a polymer concentration of 0.2 mg/ml (Fig. 2.6, top), which are not altered by annealing (Fig. 2.6, bottom).

These could be transitional from the connected to the disconnected ring-shaped structures observed by Stange, et al. [5].

§4. Conclusions.

Very thin polymer films were prepared from dilute toluene solution of deuterated polystyrene (MW = 690,000) on HF etched silicon surfaces by spin-casting at 2000 rpm for 30 s. Atomic force microscopy reveals that the most dilute solutions examined result in the formation of ultrathin films with microvoids or islands of submicron dimension. The polymer thickness in these ruptured films is approximately 20 - 30 Å, as determined by X-ray reflectivity and AFM. The surface coverage is determined by employing deuterated spin-cast films, and measuring the integrated deuterium signal by secondary ion mass spectrometry. The SIMS results indicate that the surface coverage varies linearly with the concentration of dPS in solution over a wide range of dilute concentrations, changing to a 1.5 power law dependence for thicknesses greater than ~30 Å. In the thicker films examined, 150°C anneals had negligible effect on the film thickness. In thicker polystyrene films, the power law

dependence is shown to increase markedly with molecular weight.

§5. Acknowledgments.

These studies are supported by the National Science Foundation (NSF/MRSEC-DMR-9632525).

§6. References.

1. C. W. Frank, V. Rao, M. M. Despotopoulou, R. F. W. Pease, W. D. Hinsberg, R. D. Miller, and J. F. Rabolt, Structure in Thin and Ultrathin Spin-Cast Polymer Films. *Science* **273**: 912-15 (1996)

2. C. W. Extrand, Spin Coating of Very Thin Polymer Films. *Polym. Eng. Sci.* 34: 390-394 (1994)

3. L. L. Spangler, J. M. Torkelson, and J. S. Royal, Influence of Solvent and Molecular Weight on Thickness and Surface Topology of Spin-Coated Polymer Films. *Polym. Eng. Sci.* **30**: 644-653 (1990)

4. D. B. Hall, P. Underhill, and J. M. Torkelson. Spin Coating of Thin and Ultrathin Polymer Films. *Polym. Eng. Sci.* 38: 2039-2045 (1998).

5. T. G. Stange, R. Mathew, and D.F. Evans. Scanning Tunneling Microscopy and Atomic Force Microscopy Characterization of Polystyrene Spin-Coated onto Silicon Surfaces. *Langmuir* **8**: 920-926 (1992).

6. Y. M. Strzhemechny, S. A.; Schwarz, J. Schachter, M. H. Rafailovich, J. Sokolov. Secondary Ion Mass Spectrometry Study of Silicon Surface Preparation and the Polystyrene/Silicon Interface *J. Vac. Sci. Technol.*, **A 15:** 894-898 (1997).

7. S.A. Schwarz, B.J. Wilkens, M.A.A. Pudensi, M.H. Rafailovich, J. Sokolov, X. Zhao, W. Zhao, X. Zheng, T.P. Russell, and R.A.L. Jones. Studies of Surface and Interface Segregation in Polymer Blends by Secondary Ion Mass Spectroscopy. *Molec. Phys.* **76:** 937-950 (1992).

8. J. Gu, M. D. Bullwinkel, and G. A. Campbell. Measurement and Modeling of Solvent Removal for Spin Coating. *Polym. Eng. Sci.* **36:** 1019-1026 (1996).

9. G. R. Strolb. The Physics of Polymers. Springer -Vetrlag , New York. p 64-65 (1996).

10. M.Daoud, J.P.Cotton, B.Farnoux, G.Jannink, G.Sarma, H.Benoit, R.Duplessix, C.Picot, and P.G. de Genne. Solution of Flexible Polymers. Neutron Experiments and Interpretation. *Macromolecules* 8: 804-818 (1975).

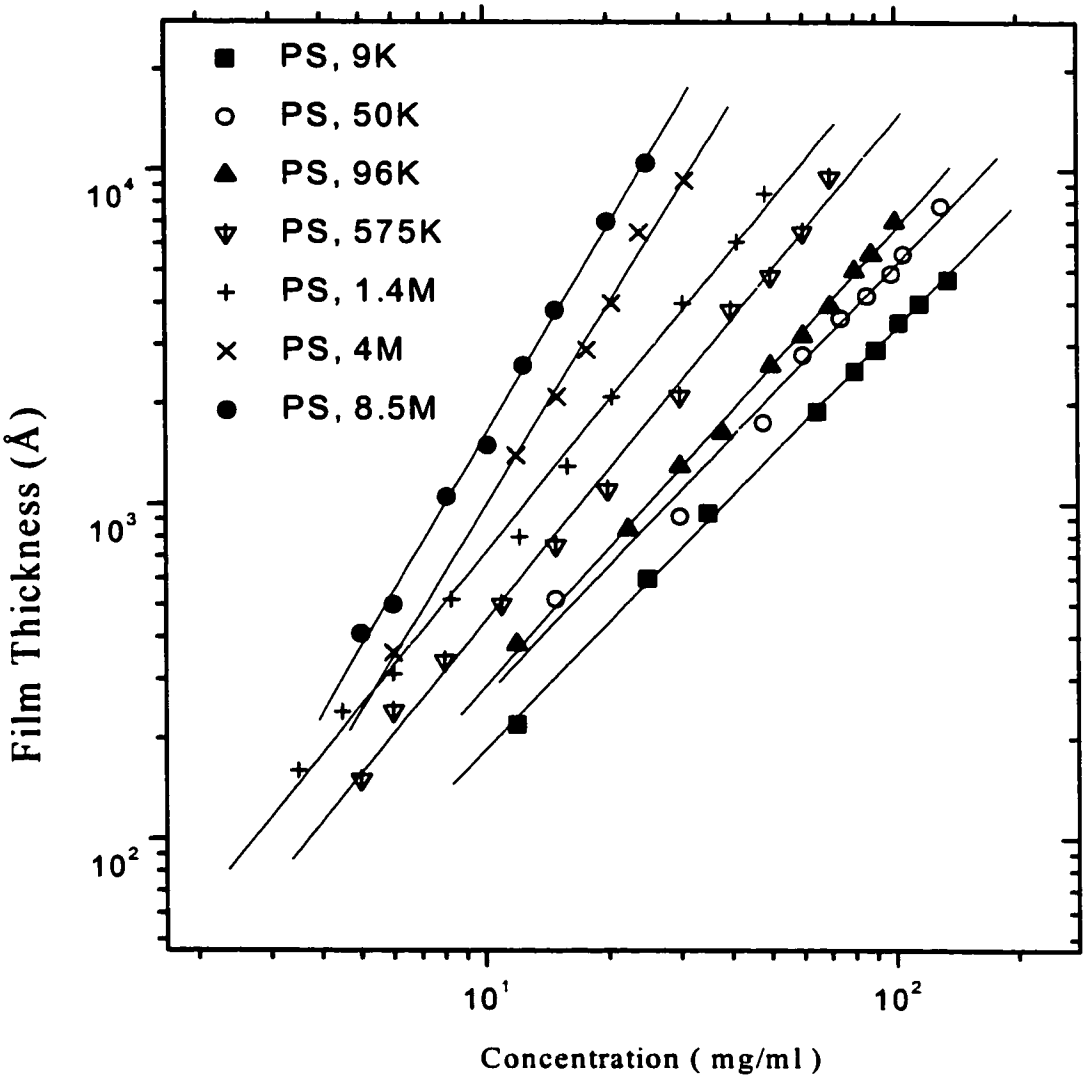

Figure 2.1. Film thickness of spin-cast PS films (2500 rpm, 30 s, on unstripped Si (100) substrates) vs. Concentration in toluene, as determined by ellipsometry.

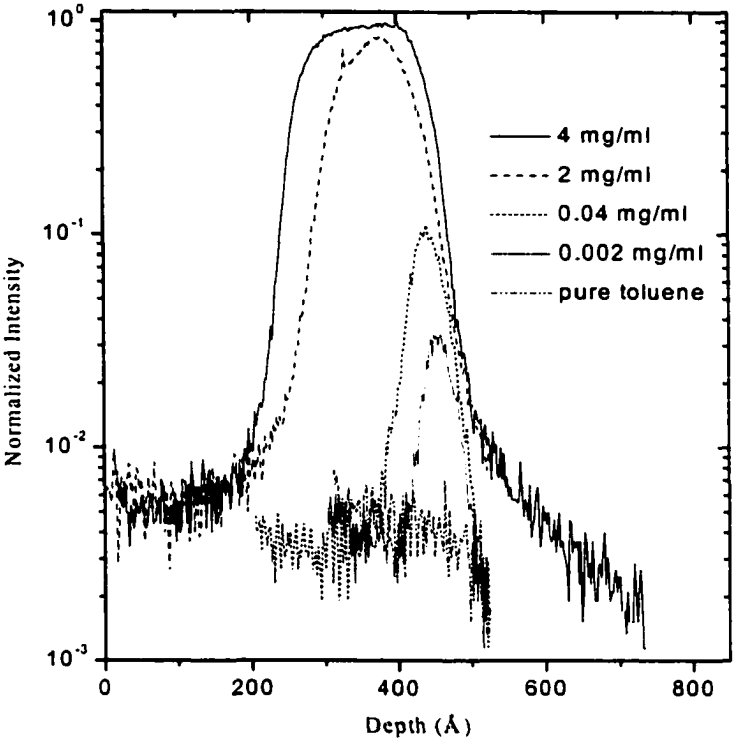

Figure 2.2. Normalized deuterium (D^-) SIMS intensity vs. depth for five concentrations of dPS in toluene, spin-cast on stripped silicon, and coated with a protective PS overlayer. The integrated area under each peak is converted to an apparent film thickness.

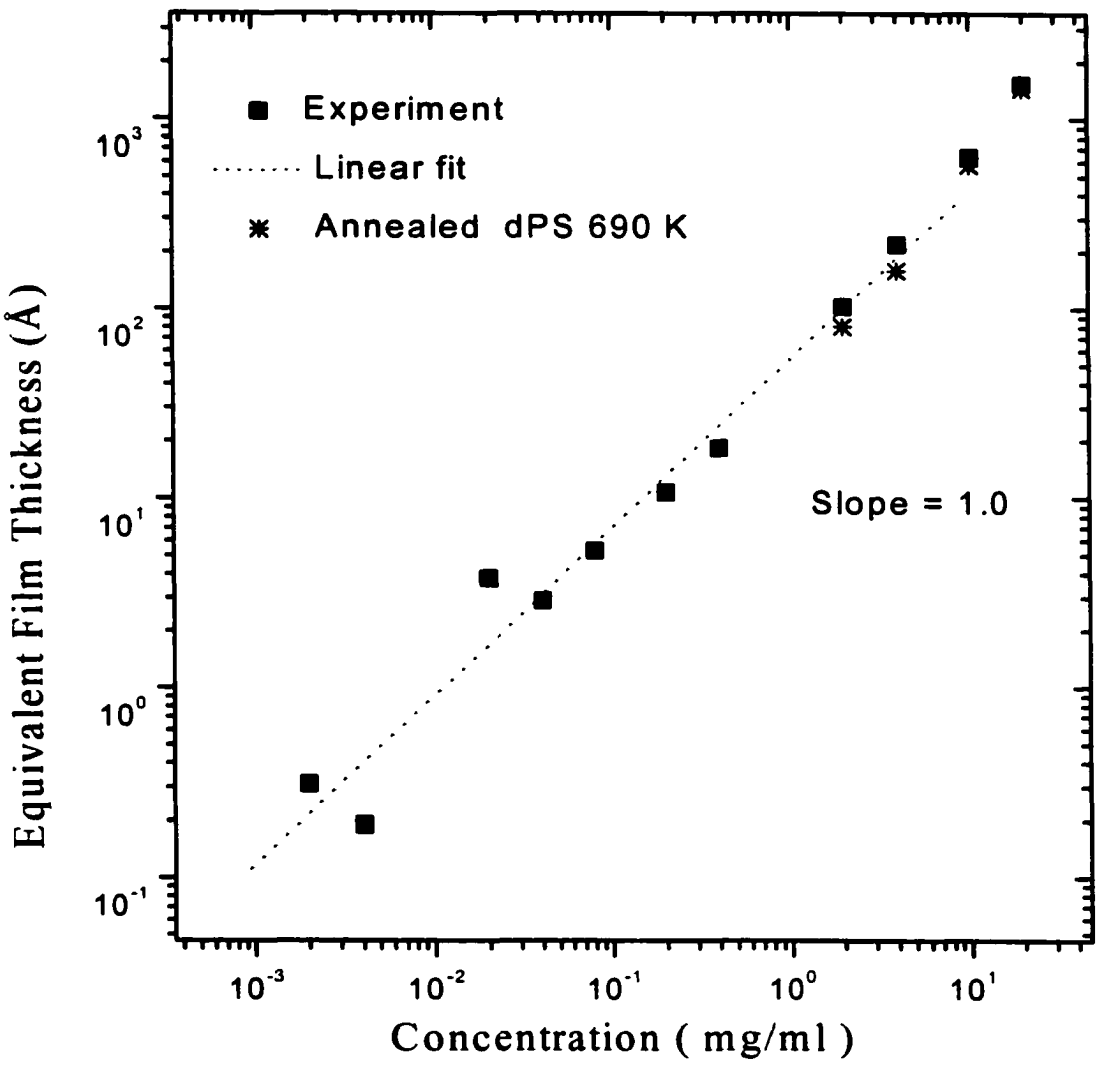

Figure 2.3. Equivalent film thicknesses of spin-cast dPS films vs. concentration in toluene, as determined by SIMS (for concentrations less than 10 mg/ml) and by ellipsometry (for the two highest concentrations).

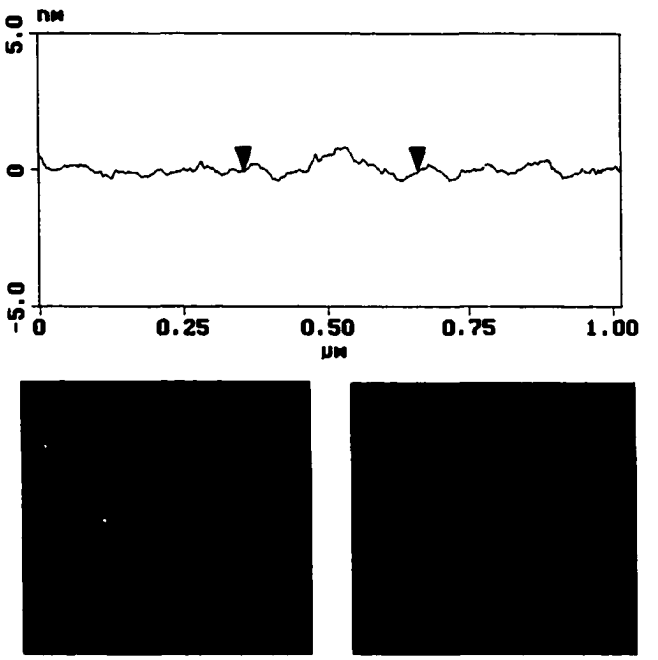

Figure 2.4a. AFM topographic (left) and friction force (right) images, and corresponding cross-section plot of height variation, for three spin-cast films: a) 2, b) 0.4, and c) 0.0002 mg/ml.

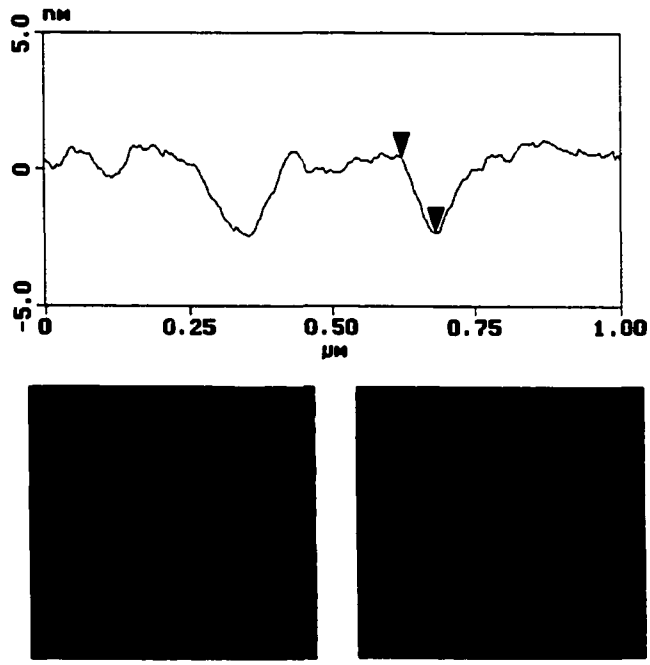

Figure 2.4b. AFM topographic (left) and friction force (right) images, and corresponding cross-section plot of height variation, for three spin-cast films: a) 2, b) 0.4, and c) 0.0002 mg/ml.

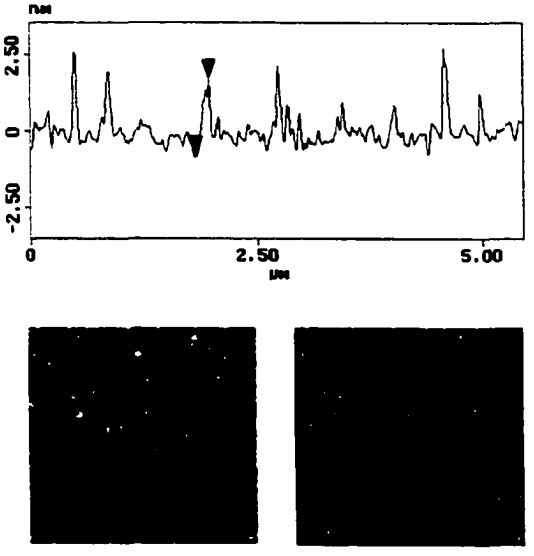

Figure 2.4c. AFM topographic (left) and friction force (right) images, and corresponding cross-section plot of height variation, for three spin-cast films: a) 2, b) 0.4, and c) 0.0002 mg/ml.

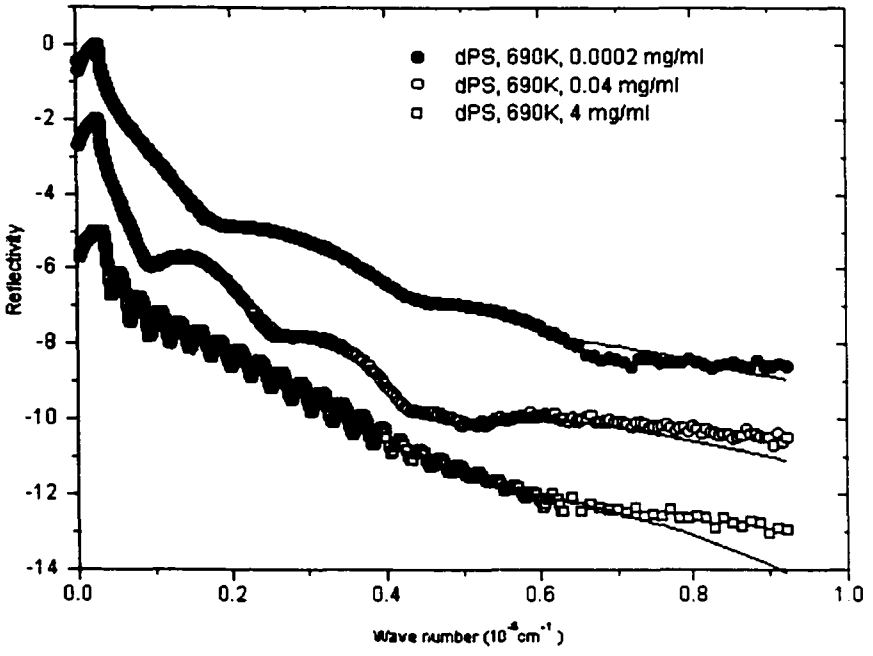

Figure 2.5. Measured X-ray reflectivity of polystyrene thin films on (100) stripped silicon obtained at 11 keV incident energy. The solid lines are the best fits to the experimental data, for concentrations of 0.0002 mg/ml, 0.04 mg/ml, and 4 mg/ml, yielding thicknesses of 20 A, 33 A, and 238 A, respectively.

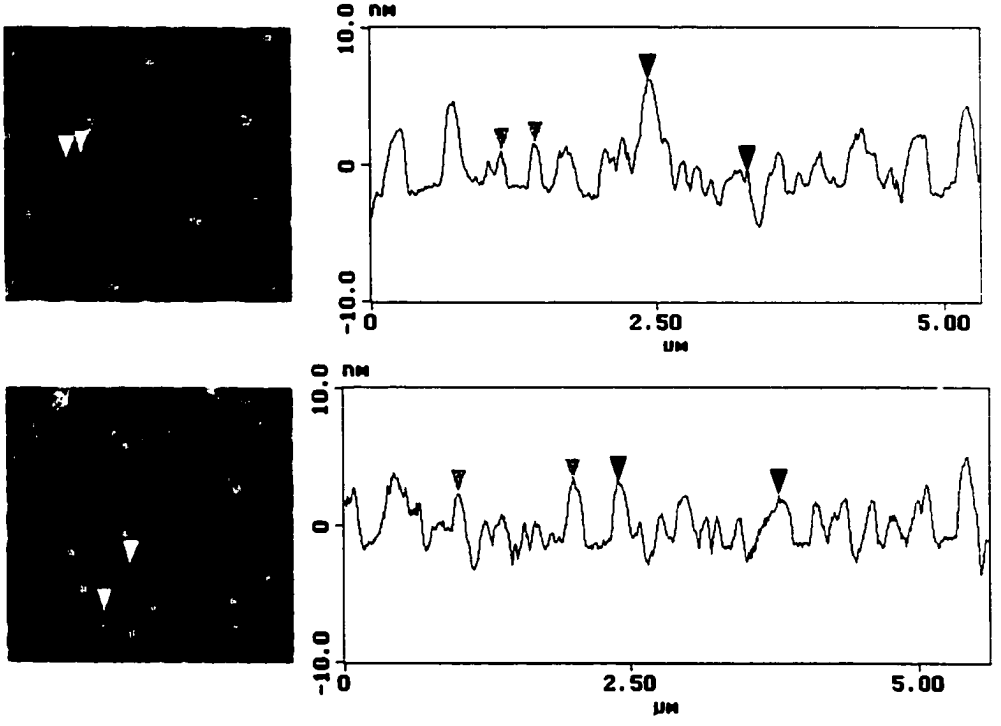

Figure 2.6. AFM topographic (left) and cross-section (right) plot of height variation for two spin-cast films: top - 0.2 mg/ml, unannealed, bottom - 0.2 mg/ml, annealed at 150 °C for 1 hour (Tg≈110°C).

Chapter 3.

Silicate Nanocomposite Spin-coated Film Formation.

§1. Introduction.

The blending of polymers with certain fillers can produce desirable behavior in the composite, such as toughness, thermal stability, resistance to abrasion, improved conductivity, weight reduction, or insulating properties. Polystyrene/clay nanocomposite films can be prepared by spin-coating on silicon substrates. The effects of solute concentration (in toluene), spin rate and the time of spinning on film thickness were examined. For uniform films ranging in thickness from 0.2μm to 10μm, thickness follows a power-law dependence on spin rate and on spinning time. For thickness versus spin rate, the power varies from -7×10^{-5} to -5×10^{-5} at low concentrations of clay and varies around -1×10^{-4} at high concentrations of clay. The experimental time dependence of the film thickness demonstrates that solutions without clay form a dry film within 15 seconds, and for solutions with clay the drying process takes more than a minute. The dependence of solution viscosity on spin rate and on polystyrene and clay concentrations, as well as the dependence of solvent evaporation rate on polystyrene concentration, were also investigated. Viscosity-concentration dependence indicates the

presence of two physically different regimes (dilute and concentrated solutions). Evaporation rate-concentration dependence shows two modes of evaporation (free surface evaporation and through-crust evaporation). A simple numerical model was employed to explain the trends of film thickness. When the model was applied for no-clay solutions, it was modified taking into account our research obtained for the evaporation process and viscosity dependence outlined above. The model, which was initially developed for no-clay solutions, provides a good agreement with the experimental data. However, its discrepancies with the data obtained for solutions with clay indicate that the theory underlying the model needs to be developed further.

Thin films of polymeric nanocomoposites may be prepared by the spin-coating, or spin-casting, technique [1-5]. In this method the nanocomposite solution is spun on a silicon substrate at rotational speeds as high as 8000 revolutions per minute (rpm) for up to two minutes. In the spinning process, the solution spreads out and thins, while the solvent evaporates. The product is a thin nanocomposite film on the order of 10^3 Å. The thickness of the film is measured by profilometry, a method in which a piezoelectric needle passes over the scratched film on the silicon substrate recording the change in depth around that scratch. From these two

techniques, data concerning the effect of spin rate or spinning time on film thickness can be obtained. However, several factors, such as the concentration, density, and viscosity of the nanocomposite solution, as well as the evaporation rate of the solvent while the film is spinning, are known to affect the film thickness [6]. Yonkoski and Soane's theoretical model for the spin-coating process of pure polymer solutions, which takes into account these factors, presents a useful equation for the rate of change of the film thickness [6], slightly simplified below.

$$\Delta h/\Delta t = (2/3)\,(\rho\omega^2 h^3/\eta) - \hat{e}, \qquad (1)$$

where h is the film thickness, t is the time, ρ is the density of the solution, ω is the spin rate, η is the viscosity of the solution, and $\hat{e}$ is the evaporation rate of the solvent.

Therefore, the viscosity of the solution and the evaporation rate of the solvent during spinning are two important variables that define the rate of change of film thickness during spin-casting. The more viscous the solution, the thicker is the film. Since the evaporation rate of the solvent depends on the amount of the solvent available at the surface of the film, solvent evaporation rate decreases as the film spreads out during spinning and eventually the film dries up.

The mechanical properties of thin polymer films and nanocomposites prepared by the spin-casting technique [1-5] are analyzed in many studies. This study examines the effect of clay, used as a filler, on the thickness of uniform polystyrene (PS)/clay films spin cast from a wide range of solution concentrations. Clay is a hydrous aluminum silicate filler that causes polymeric composites to become stronger, more resistant to heat, less permeable to gas, and less flammable [4]. During spin-coating, the large clay particles in solution exfoliate into numerous thin platelets, or sheets of clay and line up. The current study aims to create a model of the behavior of PS-clay nanocomposite films during spin-coating and define which of the key parameters, solution viscosity or solvent evaporation rate, affects film thickness most. For manufacturers of such nanocomposite materials, this would provide a better understanding of the dependence of film thickness on such important factors and the effect of clay on the formation of spin-cast films.

§2. Experiment and Model.

Monodisperse polystyrene (PS), of molecular weight 280K (Aldrich Chemical Company, Inc.), and montmorillonite cloisite 6A powder, with platelets under 20 Å in thickness and a few micrometers in length, were used

to make solutions in toluene. Solution concentrations ranging from 30 mg/ml of PS to 960 mg/ml of PS, with clay weight fractions of PS varying from 0% to about 80%, were prepared for viscosity measurements. For evaporation rate measurements, the initial PS concentration was 60 mg/ml, and various clay weight fractions, from 0% to 80%, were added.

The PS/clay nanocomposite films were spin cast at 2000, 4000, 6000, and 7720 rpm on silicon substrates, and profilometry measurements, made on a Dektak IIA profilometer, yielded the thickness of each film.

The viscosities of PS-only and PS-and-clay solutions in toluene were obtained as a function of shear rate on an ARES Rheometer from Rheometric Scientific at room temperature for the cone-and-plate geometry. Each solution was run five consecutive times to observe any effect of solvent evaporation, and viscosity measurements were plot for shear rates of 1 s^{-1} to 100 s^{-1}, and in one case for higher rates (up to about 4000 s^{-1}), as well.

Evaporation rate measurements for pure toluene, pure ethanol, and the PS-and-clay solutions in toluene were obtained by placing the sample onto a scale in a stationary, open, round glass container, 50 mm in diameter. The changes in the mass of the sample were recorded along with the time. The evaporation rate, e was calculated as $e = [1/(\rho\pi r^2)] \times (\partial m/\partial t)$, where ρ is the

density of the solvent (toluene), r is the radius of the container, m is the mass of the sample and t is the time.

As the toluene, evaporates, the solution on the spinning wafer becomes more concentrated. For the purposes of numerical modeling we employ a model equation for concentration of PS which, as a first approximation neglects any volume change resulting from mixing. For a small interval of time, Δt, the concentration of PS, measured in mg of PS per ml of toluene, $C_{PS} = \rho_{PS}V_{PS}/V_{tol}$, changes to C_{new}, which is derived below. (V_{tot} is the total volume of the solution; V_{PS}, V_{cl}, and V_{tol} are the volumes of PS, clay and toluene, respectively; C_{PS} is the concentration of PS; f is the clay/PS weight ratio; M_{PS} is the mass of PS; ρ_{PS} and ρ_{cl} are the respective densities of PS and clay (in mg/cm^3); ΔV_{tol} is the volume of evaporated toluene; h is the thickness of the solution layer on the wafer; e is the evaporation rate of toluene; and t is the time.)

$$C_{new} = (C_{PS}) / [1 - (e\Delta t/h)(1+C_{PS}/\rho_{PS} + fC_{PS}/\rho_{cl})]. \quad (2)$$

The simple equation that fits e, the evaporation rate for a still PS and clay solution in toluene, was based on the idea that, at high concentrations, the evaporation rate is proportional to the fraction of free toluene at the surface of the container: $e = e_0[(V_{tol}-V_{trapped}) / (V_{tol}+V_{PS}+V_{cl})]^{2/3}$, where e_0 is a scaling constant, V_{tol} is the total volume of toluene in solution, $V_{trapped}$ is

the amount of toluene that will remain trapped in the film, V_{PS} is the volume of PS in solution, and V_{cl} is the volume of clay in solution. The power 2/3 comes from the relation between the surface area and volume of the container. The scaling constant, e_0, is chosen in such a way that when C, the concentration of PS in solution, is zero, the evaporation rate, e, is close to the evaporation rate of pure toluene, as can be seen from the simplified form in equation (3) below. Since the evaporation rate of toluene was found experimentally to be 0.075 μm/s, e_0 is equal to this value. Following is the equation for e, where C is the current PS concentration, and C_f is the final solution concentration.

$$e = e_0 [(1-C/C_f) / (1+C/\rho_{PS} + CM_{cl}/M_{ps} \times 1/\rho_{cl})]^{2/3}. \quad (3)$$

Therefore, the formula for e has two fitting parameters: e_0 and C_f, which are well determined by experiment.

The model should take into account the dependence of the evaporation rate on spin rate, described by the formula, $e = C_e\omega^{1/2}$, where e is the evaporation rate when the sample is spinning, C_e is the scaling constant, and ω is the spin rate [10]. When ω is small or zero, the evaporation rate is not zero but is equal to the evaporation rate of the solution when it is stationary. Thus, at some spin rate, ω_0, the evaporation rate of the still solution, e_s, is equal to $e_s = C_e \times \omega_0^{1/2}$. Then the equation for e becomes:

$$e = e_s \times (\omega/\omega_0)^{1/2} \quad (4)$$

The measurements of the evaporation rate for ethanol ($e_{ethanol} = 8.25681 \times 10^{-8}$ m/s) and the scaling constant, C_e, of ethanol ($C_{e\text{-}ethanol}$=0.04 μm/s* $rpm^{-1/2}$), found by D.E. Haas et al [10], were used to determine the value of ω_0 to be 4 rpm for ethanol. The use and modification of this value for ω_0 is explained in the Results section.

For the purposes of numerical modeling the total density of the solution, ρ_{tot} , was calculated as shown below with the following notations: M_{tot} is the total mass of the solution, V_{tot} is the total volume of the solution, M_{tol} is the mass of toluene, and $C=M_{PS}/V_{tol}$ is the concentration of PS in solution.

$$\rho_{tot} = [(C) + (M_{cl}/M_{PS})(C) + (\rho_{tol})] / [(C/\rho_{PS}) + (C)(M_{cl}/M_{PS})(1/\rho_{cl}) + 1] \quad (5)$$

The surfactant content is ignored here, but the variation in ρ is small and has little effect in the simulation. Thickness versus spin rate dependence and thickness versus spin time dependence were modeled using equation1. In this model, η and e are functions which we found experimentally. The algorithm of the program is based on calculation of a new film thickness, a new concentration, and new values for ρ_{tot}, η, and e after each time step.

§3. Results.

Plots of film thickness versus spin rate, shown in Fig. 1A and Fig. 1B, were fit on a semi-logarithmic scale. The empirical equations fitting the data were of the form $h = 10^{[A + B \times S]}$, where h is the film thickness in Angstroms, S is spin rate in rpm, and coefficients A and B, provided in Table 1, are functions of PS and clay weight fractions. Plots of film thickness on a semi-logarithm scale as a function of spinning time for PS, 60 mg/ml, with different clay amounts and for different spin rates, exhibited a power dependence, with a power of around 0.7 – 0.8 [6].

An example of viscosity measurements data is provided in Fig. 2, where the concentration of PS was 480 mg/ml and the clay weight fractions of PS shown were 0% and 40%. The viscosity values used for each solution in graphing viscosity as a function of PS concentration and clay weight fraction of PS were those at 100 s^{-1}, since during spin-coating, the shear rate is high. An example of viscosity dependence on shear rate at high shear rates is provided in Fig. 2B for a solution with 60 mg/ml PS and no clay. It demonstrates that at higher shear rates the graph levels off and viscosity change from the value at 100 s^{-1} does not exceed 20%. In addition, numerical modeling efforts demonstrated that even if the viscosity changes

by an order of magnitude, the final film thickness changes by about 20%, which is not a lot compared to an order of magnitude change in film thickness as a result of an order of magnitude change in evaporation rate, which is discussed in more detail below.

The viscosity plot against PS concentration and clay concentration (Fig. 3 and Fig. 4) reveals two physically different regions of behavior, that of dilute solutions and that of concentrated solutions, each of which could be described with a different equation for viscosity. From the data for PS-only solutions (Fig. 3), a critical PS concentration was determined to be the point of intersection of the two straight lines fitting dilute-solution data points and concentrated-solution data points [7]. This concentration was 237 mg/ml of PS. For solutions with concentrations of PS, C, at or below this critical concentration, the equation for viscosity is $\eta=10^{[-2.11991 + 0.01381\times C]}$; for solutions with PS concentration, C, above this critical point, $\eta=10^{[-0.59133 + 0.00231\times C]}$. In order to take into account the effect of the added clay on solution viscosity, a correction factor that relates the solution viscosity to the amount of clay in the solution can be included into these empirical formulas. This factor can be obtained from the slopes of the fits for solution viscosity as a function of clay weight fraction of PS, shown in Fig. 4 and in Table 2. Since the slopes are nearly the same for various solution concentrations,

their average signifies the correction factor for the viscosities of solutions with clay. This correction factor, found to be 0.01, was added to the empirical equations for viscosity, modifying them in the following way, where f is the clay weight fraction of PS: $\eta=10^{[-2.11991 + 0.01381\times C + 0.01f]}$, when C is less than or equal to 237 mg/ml; and $\eta=10^{[-0.59133 + 0.00231\times C + 0.01f]}$, when C exceeds 237 mg/ml. With this modification, the numerical model is able to predict the system behavior taking into account the effect of clay on viscosity. This two line behavior is frequently observed in the literature.

Plots of the evaporation rates of the solutions versus their PS concentrations, shown in Fig. 5, display two distinct regimes of evaporation having different physical characteristics: free-surface evaporation and through-crust evaporation [9, 10]. During free-surface evaporation, the toluene exposed at the surface of the sample evaporats at a constant rate. At a certain critical PS concentration, however, the evaporation rate of toluene decreases exponentially, characterizing the through-crust evaporation regime. In between the two modes of evaporation, there is a gradual transition.

The evaporation data were fit with theoretical equation (3) as shown in Fig. 5. The value used for the final PS concentration is C = 5000 mg/ml, the same value entered in the numerical model and the final PS

concentration of the solutions for which evaporation measurements were conducted. Shown are the model's fits for 0% and 80% clay weight fractions. The fits follow the trends of the experimental data, from the constant free-surface evaporation mode to the steep downhill through-crust mode, and the main advantage of this model for e_0 is that it gives a good fit of the gradual transition from free-surface to through-crust evaporation.

An alternative model gives a more obvious demonstration of the presence of two evaporation regimes. Fitting the evaporation data in this model involves fitting each experimental curve with two straight lines (on logarithmic scale), one for free-surface evaporation mode and the other for through-crust evaporation mode, the threshold PS concentration can be determined as the cross-point, marking the transition from free-surface to through-crust evaporation. The model would be based on the use of four fitting parameters for these lines, A_{fs}, B_{fs}, A_{tc}, and B_{tc}. These parameters, as well as the threshold PS concentration, C_{th}, can be plot and fitted as functions of clay weight fraction of PS for use in an equation for each evaporation regime. Then, for free-surface evaporation, when the PS concentration, C_{PS}, is below C_{th}, the rate of evaporation, e, is: $e = 10^{(A_{fs}+B_{fs}\times C_{PS})}$; and for through-crust evaporation, when C_{PS} exceeds C_{th}, the evaporation rate is: $e = 10^{(A_{tc}+B_{tc}\times C_{PS})}$. The alternative model fitting the

evaporation data shows the asymptotic behavior of the two distinct evaporation regimes, free-surface and through-crust, and explains peculiarities of asymptotic behavior for the main model in Fig. 5. The disadvantage of this model is that it fails to account for the gradual transition from free-surface to through-crust evaporation regime. Therefore, the first model was used to fit the experimental data for evaporation rate and to provide the theoretical predictions in the numerical modeling.

In order to take into account the effect of the spinning during spin-casting on solvent evaporation rate, the evaporation rate for still solutions, e_s, obtained from the model fitting experimental data was adjusted by use of equation 4. When applying this adjustment to the numerical program, it was found that $\omega_0 = 4$ rpm gives incorrect values for the drying times observed experimentally in films containing clay (Fig.6): no-clay solutions become dry in about 15 seconds and high clay concentration solutions become dry in more than a minute. In order to obtain correct drying times for no-clay solutions, ω_0 was increased to 50 rpm. This value produced reasonable agreement with the experimental data for thickness-spin rate and –spin time dependences (Fig. 1B and 6B) for solutions without clay, for which the model was initially developed. Therefore, the formula for the evaporation

rate, e, of the PS and clay solutions in toluene is $e = e_s \times (\omega/\omega_0)^{1/2}$, where ω_0 = 50 rpm.

The predictions of the simple numerical model, which was initially developed for pure polymer solutions [6], agree with the experimental data for film thickness-spin rate and –spin time dependence for no-clay solutions, as shown in Fig. 1B and 6B, respectively. Its failure to correspond with the data obtained for solutions with clay, however, suggests the need to further develop the theory underlying the model so that it incorporates the behavior of film thickness for nanocomposite films. Nevertheless, the model provides important information about the factors affecting the trends of film thickness. When the equation for viscosity was changed by an order of magnitude, the final film thickness produced by the program changed only by about 20%. Changing ω_0 for the evaporation rate by an order of magnitude, from 4 rpm to 50 rpm, produced almost an order of magnitude change in the final film thickness. Therefore, viscosity does not have a major effect on the film thickness, whereas the evaporation rate affects it considerably.

§4. Conclusion.

Thin polymer nanocomposite films were prepared from toluene solutions of polystyrene (MW = 280,000) and clay 6A on silicon surfaces by spin-casting at spin rates varying from 2000 rpm to 7720 rpm and for time intervals from 30 seconds to two minutes. Profilometry reveals a power-law dependence of the film thickness on spin rate with a weak dependence of the power on clay concentration. Viscosity measurements indicate the presence of two physically different regimes (dilute solution and concentrated solution) having power-law dependences where the power varies from -2 for dilute solutions to –0.6 for concentrated solutions. Evaporation rate-concentration dependence also indicates the presence of two regimes (free-surface evaporation and through-crust evaporation). The through-crust evaporation process causes the evaporation rate to change from a constant value to an exponentially small quantity.

In order to explain the trends of film thickness-spin rate dependence based on the conducted viscosity and evaporation rate measurements, a simple numerical model was applied. The model is found to be in good agreement with the experimental data for no-clay solutions for which it was initially developed. However, the theory behind the model needs further development incorporating the effects of fillers, such as silicates, so that it

can account for the trends of film thickness for nanocomposites. The numerical model also demonstrated that an increase or decrease in viscosity by an order of magnitude leads to only a 20% change in the final film thickness. More influential are changes in the ω_0 parameter for the evaporation rate by one order of magnitude (from 4 rpm to 50 rpm), which lead to a change of just a little less than one order of magnitude in the film thickness for high clay concentrations (compatible with PS concentration). Therefore this simple theoretical model, although imperfect for solutions with clay, still indicates an important conclusion on the physics of the process: solvent evaporation plays by far a more important role in film formation than solution viscosity.

Further experimentation should attempt to explain the adjustment of the evaporation rate-spin rate dependence (equation 4) using $\omega_0 = 50$ rpm so that the numerical model's predictions correspond with the experimental data for no-clay solutions and account for non Newtonian behavior due to low shear rates in the thicker films.

§5. References.

1. V. Shapovalov, V. S. Zaitsev, Yu. Strzhemechny, F. Choudhery, W.Zhao, S. A. Schwarz, S. Ge, K.-W. Shin, J. C. Sokolov, M. H.Rafailovich. Nanostructure Formation in Spin-Cast Polystyrene Films. *Polymer International* **49**: 432-436 (2000)

2. C. W. Frank, V. Rao, M. M. Despotopoulou, R. F. W. Pease, W. D. Hinsberg, R. D. Miller, and J. F. Rabolt, Structure in Thin and Ultrathin Spin-Cast Polymer Films. *Science* **273**: 912-15 (1996)

3. L.L.Spangler, J.M.Torkelson, and J.S.Royal, Influence of Solvent and Molecular Weight on Thickness and Surface Topology of Spin-Coated Polymer Films. *Polym.Eng.Sci.* **30**: 644-653 (1990)

4. M. Alexandre, P. Dubois. Polymer-layered silicate nanocomposites: preparation, properties and uses of a new class of materials. *Materials Science and Engineering*, **28:** 1-63 (2000).

5. R.K. Yonkoski, D.S. Soane. Model for spin coating in microelectronic applications. *J. Appl. Phys.* **72** (2), 725-740

6. J.R. Fried. *Polymer Science and Technology*. Prentice Hall, NJ, 1995. pp. 392-394, 412.

7. P.C. Painter, M.M. Coleman. *Fundamentals of Polymer Science*. Technomic Publishing Company, PA, 1994. pp. 387-391

8. P. D. de Gennes. Solvent evaporation of spin cast films: "crust" effects. *The European Physical Journal E.* **7:** 31-34 (2002)

9. D.E.Haas, J.N. Quaijada, S.J. Picone, D.P. Birnie. Effects of solvent evaporation rate on "skin" formation during spin

coating of complex solutions. In SPIE Proc. **3943**, Sol-Gel Optics V, B.Dunn, E. Pope, H. K. Schmidt, and M. Yamane, Editors, (2000) 280- 284

10. D.Meerhofer. Characteristics of resist films produced by spinning. *J. Appl. Phys.*, 49(7), July 1978, pp. 3993-3997.

11. C.W.Extrand, Spin Coating of Very Thin Polymer Films. *Polym.Eng.Sci.* **34:** 390-394 (1994)

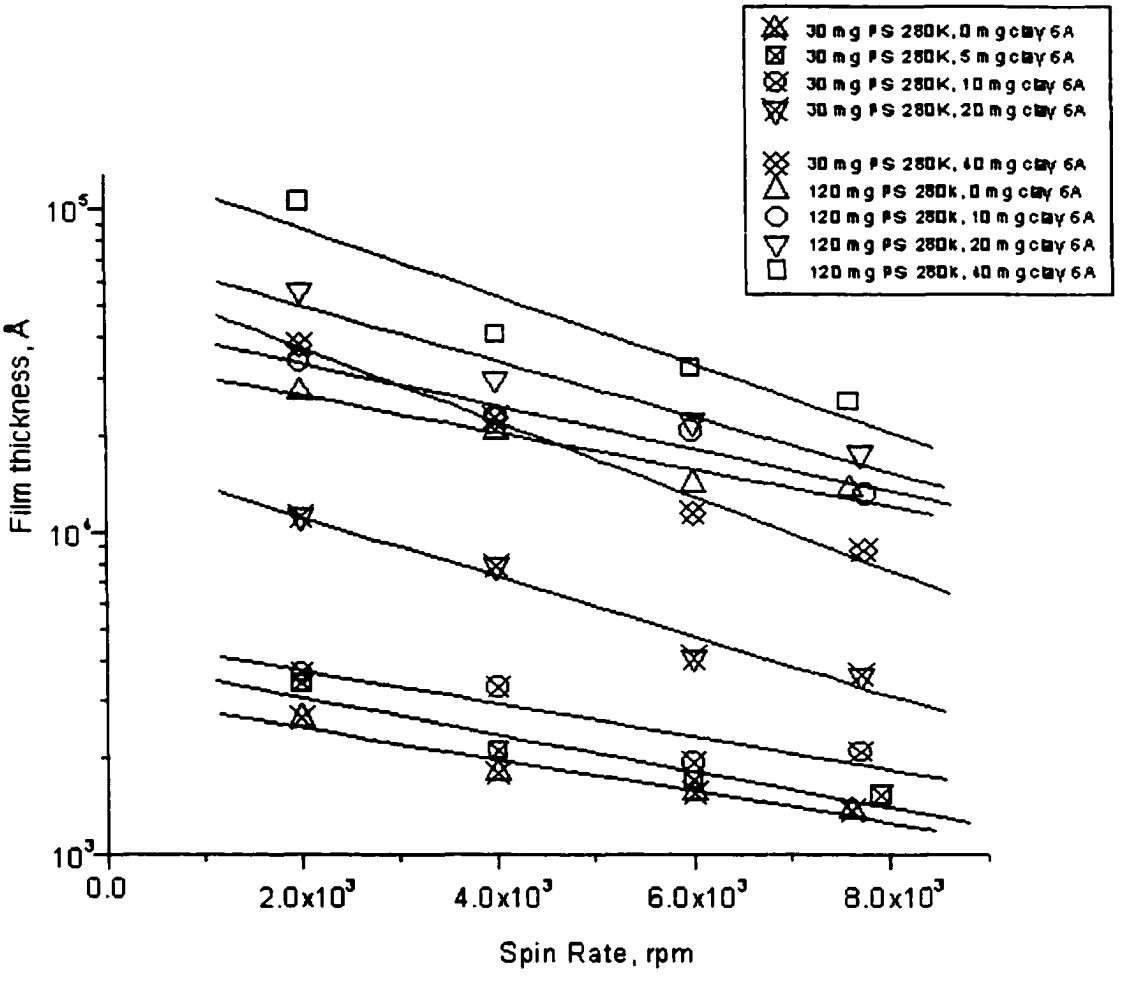

Figure 3.1A Nanocomposite spin cast film thickness versus spin rate.

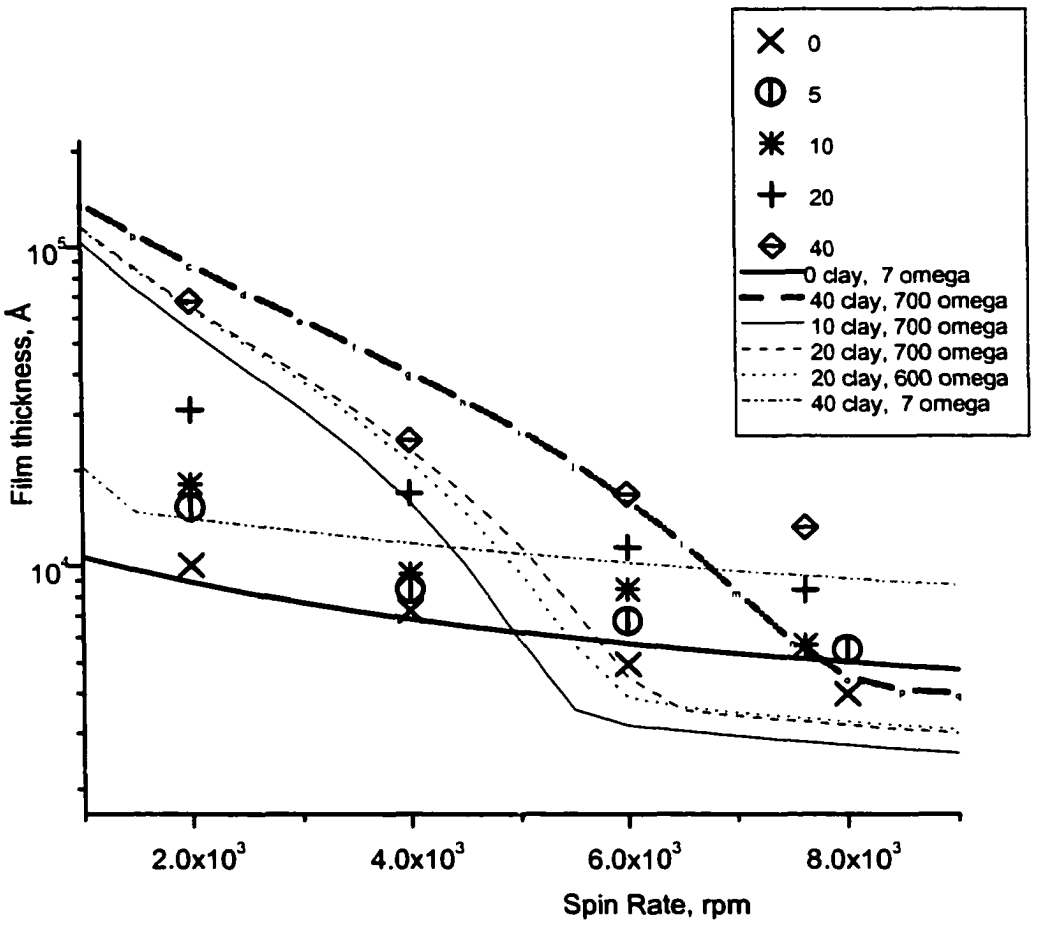

Figure 3.1B Nanocomposite spin cast film thickness versus spin rate. (e_0=0.075μm/s).

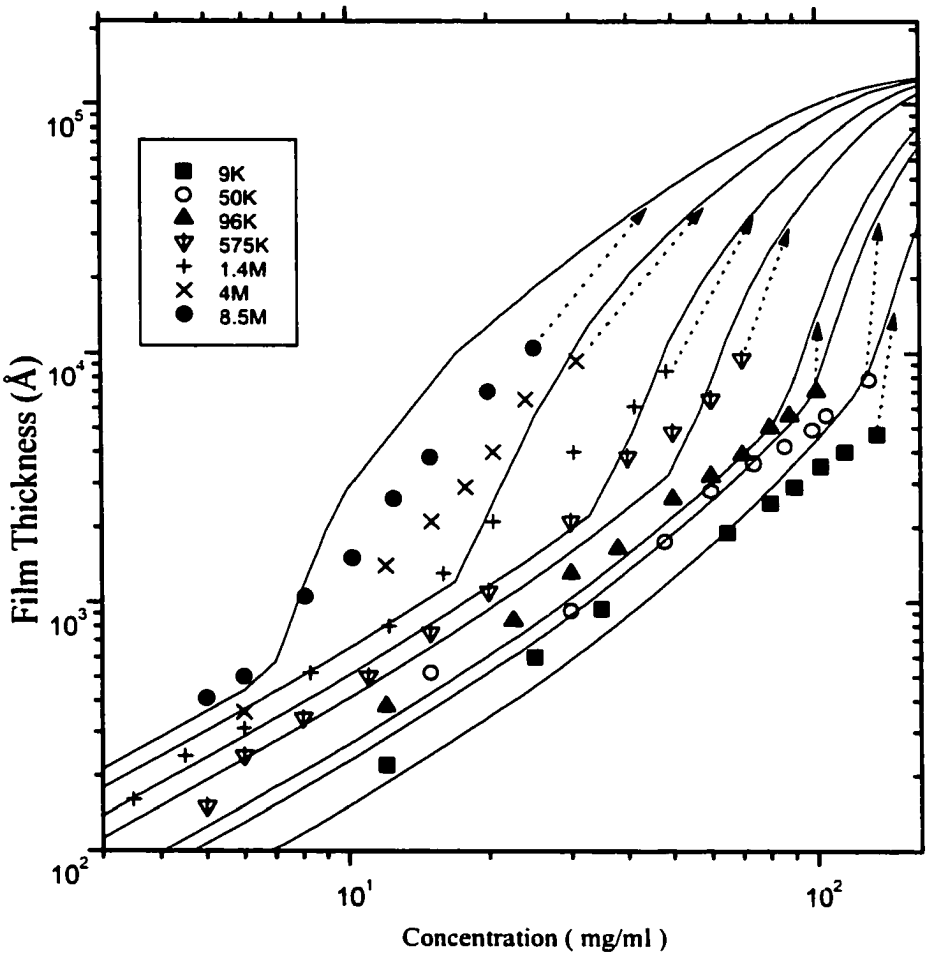

Figure 3.1C. PS spin cast film thickness versus spin rate. Experimental data and numerical modeling predictions. Fitting parameters: w_0 = 200 rpm, viscosity was multiplied by a factor of 0.4 .

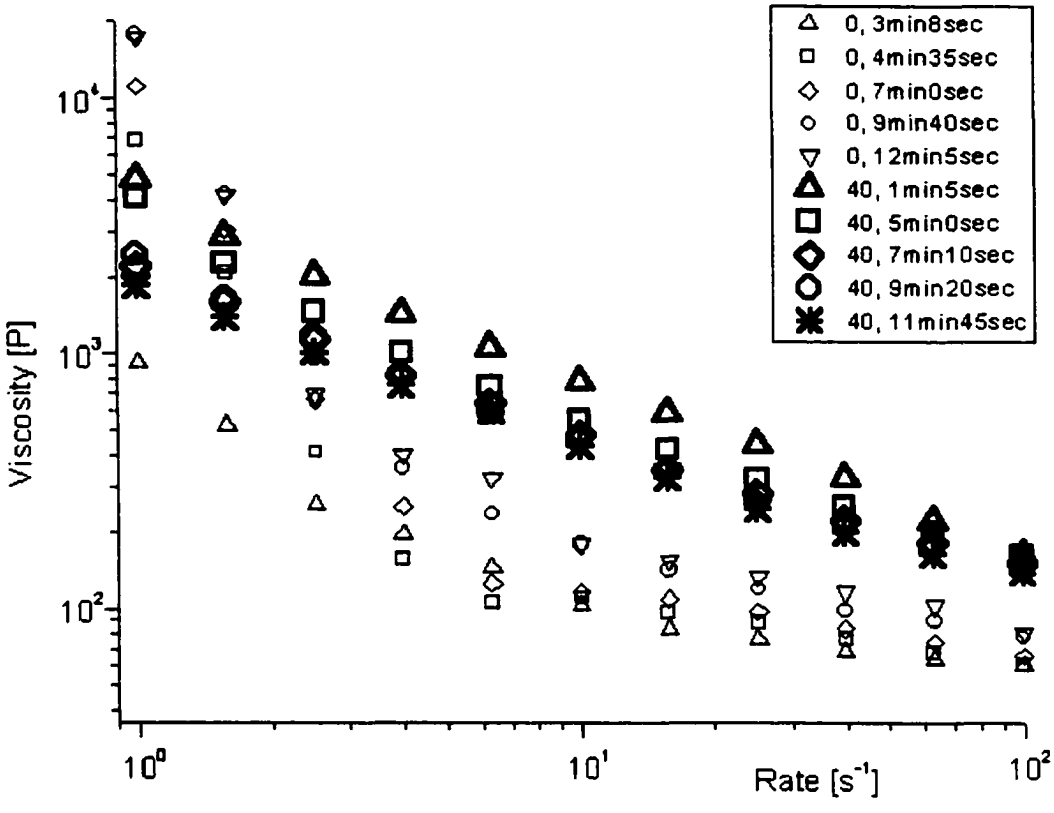

Figure 3.2A A typical set of raw rheometry data: viscosity of 480 mg/ml PS 280K and clay 6A solution in toluene versus shear rate (measured in cone-and-plate geometry set). The measurements were obtained at ARES Rheometer from Rheometric Scientific at room temperature for cone-and-plate geometry. Clay weight fraction of PS in percent is indicated in the legend, followed by the run times. The duration of each run was 87 or 88 seconds. The data can be fit with the Carreau model equation [6]: $\eta=\eta_f(1+\lambda^2 I_2)^{(n-1)/2}$, where η_f and λ are constants that depend only on solvent weight fraction; I_2 is the second invariant of the deformation tensor, a measure of the shear rate. Similar rheometry data were obtained for different PS and clay weight fractions, and empirical equations for viscosity as functions of PS and clay weight fractions were obtained (shown in Fig. 3 and 4).

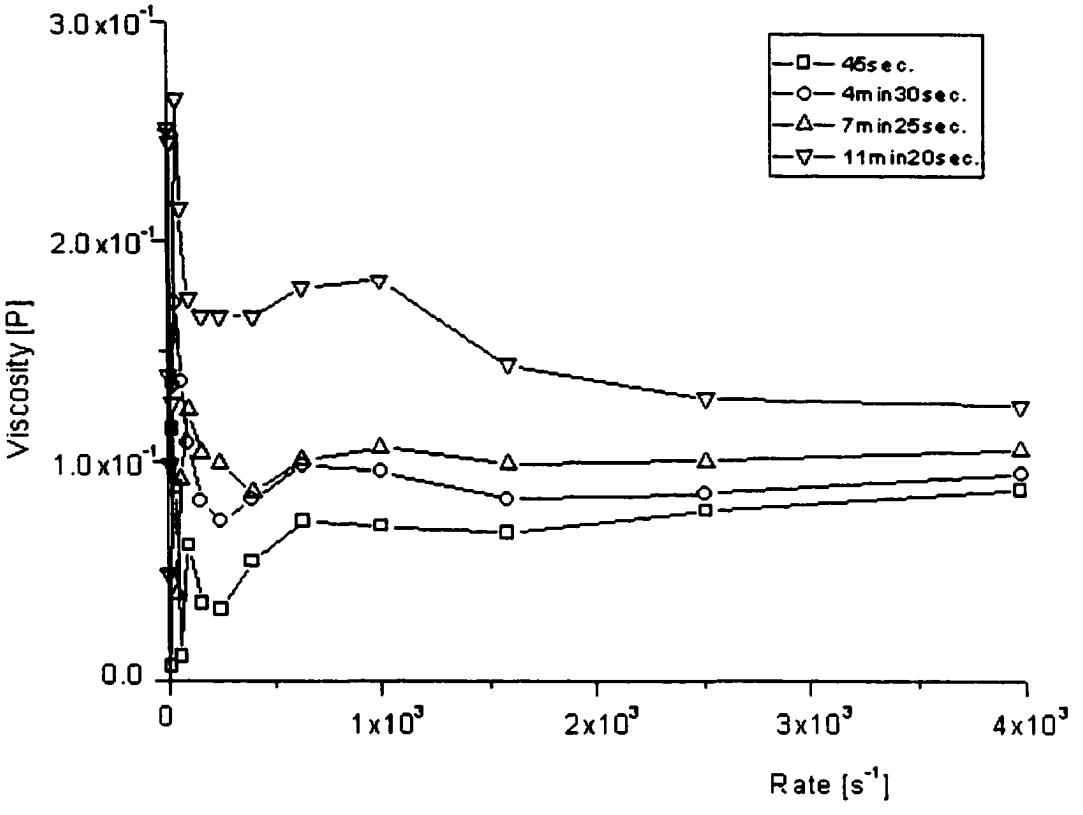

Figure 3.2B Raw rheometry data obtained at ARES Rheometer from Rheometric Scientific, at room temperature and for cone-and-plate geometry, for the viscosity-shear rate dependence of a solution with 60 mg/ml PS 280K and no clay 6A, spun at high shear rates. The run times are indicated in the legend, and the duration of each run was 145-146 seconds. At higher shear rates, the graph levels off, and the difference between viscosity at this plateau and viscosity at 100 s^{-1} does not exceed 20%.

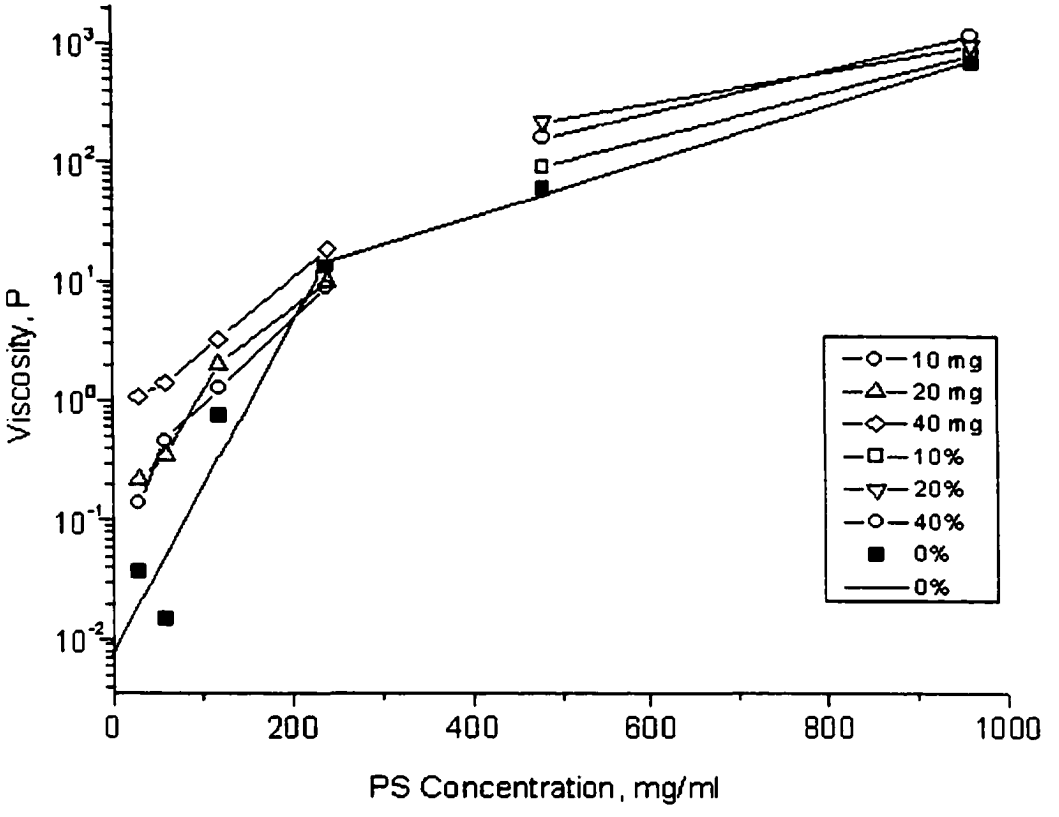

Figure 3.3 Viscosity of PS 280K and clay 6A solutions in toluene versus PS concentration. The graphs are plot for shear rate 100 s^{-1}, since during spin-coating shear rates are high. The measurements were obtained at ARES Rheometer from Rheometric Scientific at room temperature for cone-and-plate geometry. The amount of clay present in each solution, by mass or by weight fraction of PS, is indicated in the legend. The fitting data for viscosity of PS-only solutions yield the equations for viscosity. There are two regions of physically different behavior: dilute solutions and concentrated solutions [7]. Each region is described with a different equation. If the concentration of polystyrene, C, is less than or equal to 237 mg/ml, then the viscosity of the PS solution in toluene is $\eta=10^{[-2.12+0.01\times C]}$; if the concentration of polystyrene, C, is more than 237 mg/ml, then the viscosity of the PS solution in toluene is $\eta=10^{[-0.59+0.0021\times C]}$.

The data for solutions with clay tend to follow the dependence of PS-only solution viscosity, with a small correction factor. The dependence of viscosity on clay weight fraction of PS is illustrated in the Fig. 4.

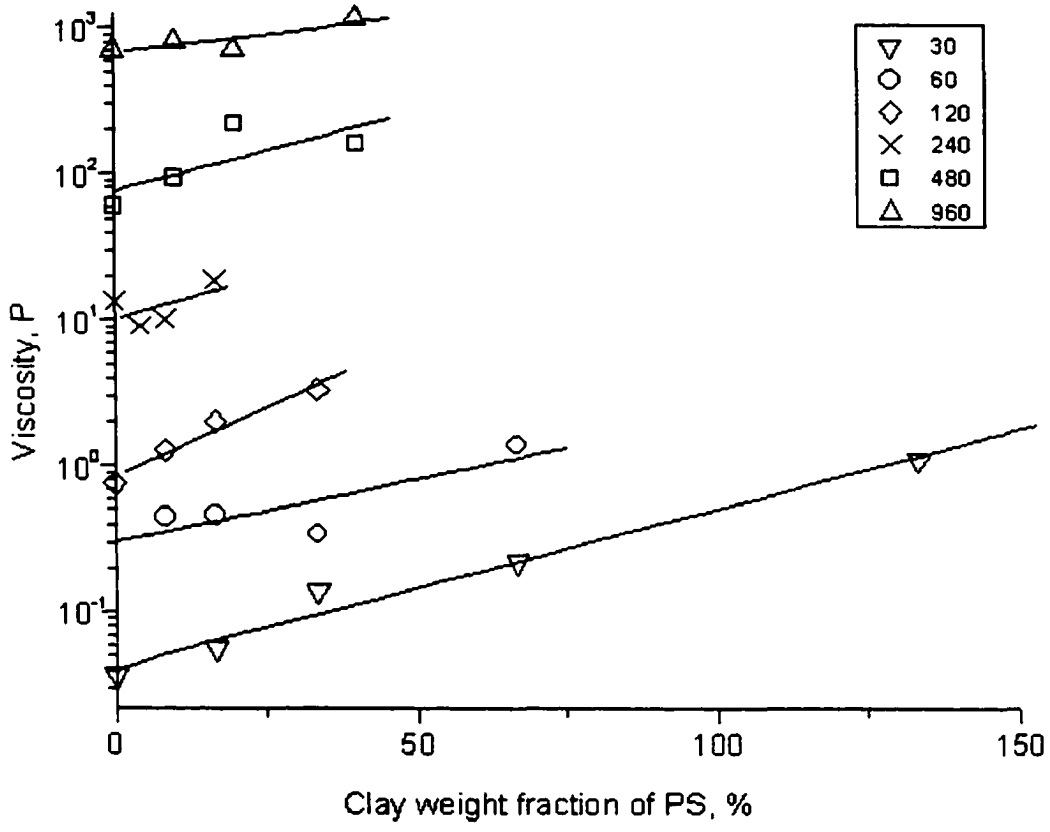

Figure 3.4 Viscosity of PS 280K/clay 6A solutions in toluene as a function of clay weight fraction of polystyrene. The graphs are plot for shear rate 100 s^{-1} and for the first run of each solution. PS concentrations, in mg/ml, are indicated. The measurements were obtained at ARES Rheometer from Rheometric Scientific at room temperature for cone-and-plate geometry. The data for solutions with clay have a tendency to follow the dependence of PS-only solution viscosity (Fig. 3) with two clear-cut regimes: dilute solution and concentrated solution [7]. This graph illustrates this tendency.

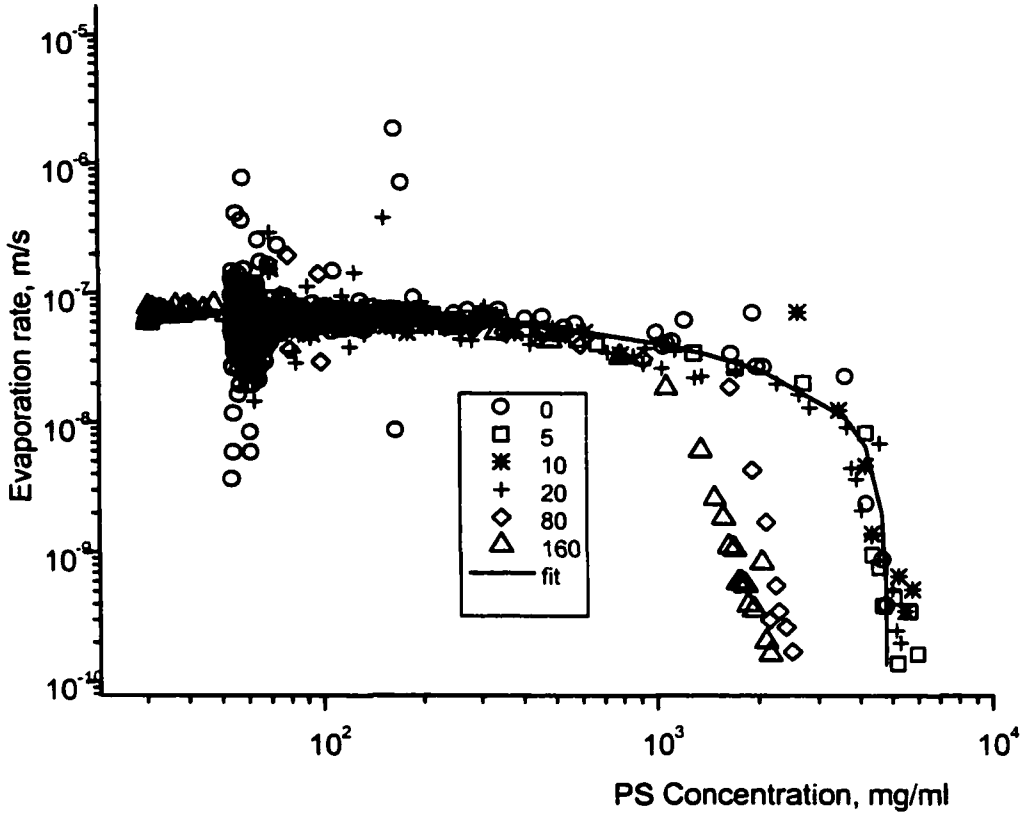

Figure 3.5 Evaporation rate for toluene solution of 60 mg/ml PS 280K and different clay 6A weight fractions in %, indicated in the legend, versus PS concentration with theoretical fits to experimental data. The graph indicates the presence of two physically different regimes of evaporation: free surface evaporation and through-crust evaporation [9, 10]. The through-crust evaporation is characterized by an exponential decrease of evaporation rate. In between the two regimes, there is a gradual transition from free-surface to through-crust evaporation. The theoretical models fitting the evaporation data were based on the equation (3) for evaporation rate.

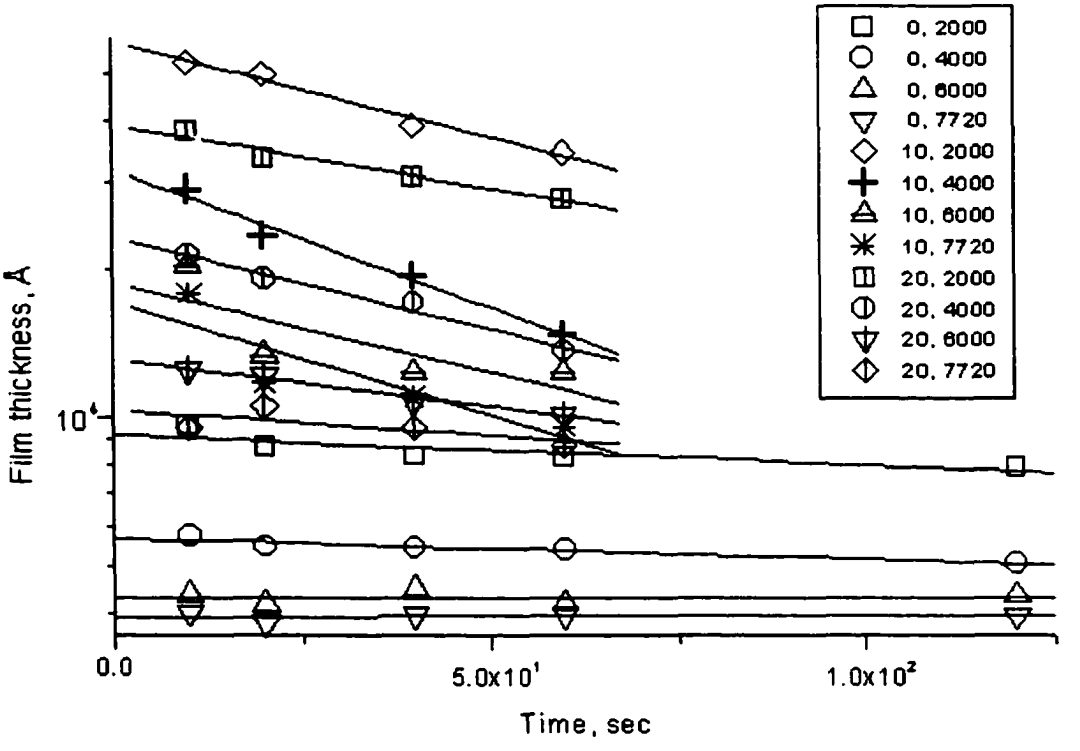

Figure 3.6A Thickness of the nanocomposite films for different spin times. The graphs are plot for PS 280K, 60mg/ml with the different clay amounts (in mg/ml), followed by different spin rates (in rpm), indicated in the legend. The graphs permit the analysis of the power dependence of film thickness on spin time (with the power reported to be around 0.7 – 0.8 [6]). Also, the graphs show that solutions without clay dry up within 15 seconds of spinning, while those with clay have drying times of more than a minute.

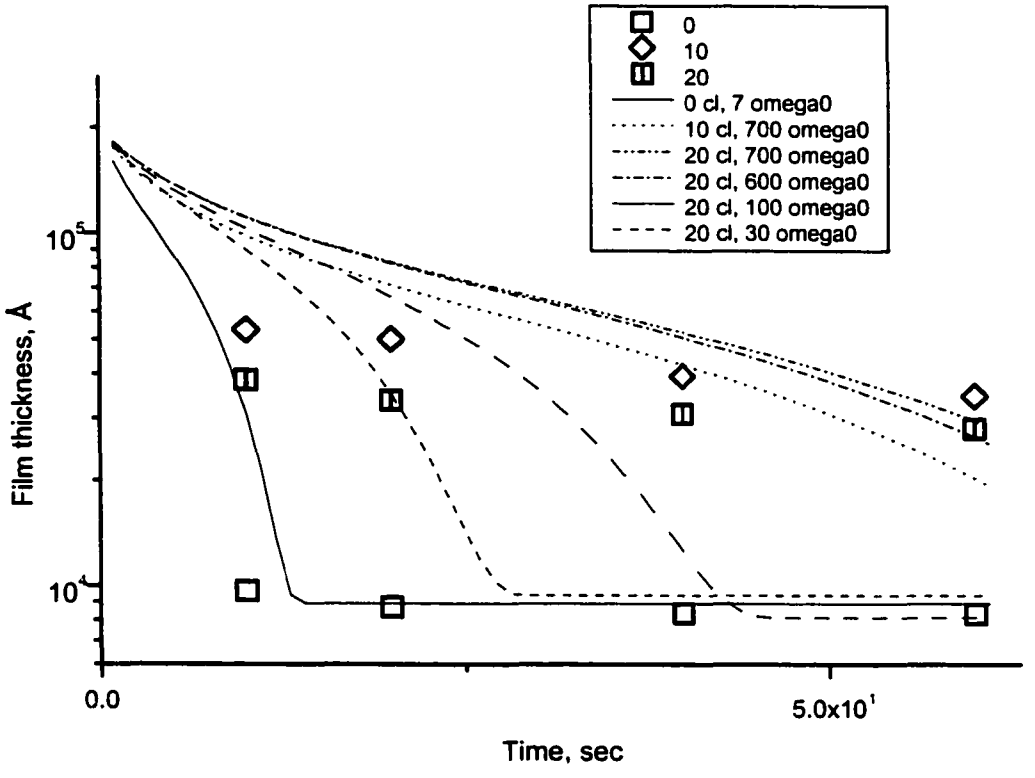

Figure 3.6B Film thickness-spin time dependence with numerical model's predictions. Experimental data are provided for 60mg/ml PS 280K with different clay amounts (in mg/ml), as indicated in the legend, and for a spin rate of 2000 rpm. The numerical model's predictions are the solid and dashed lines for which the clay amount (mg/ml) followed by ω_0 (rpm) is indicated in the legend. The simple numerical model[6] (Eq. 1 in Introduction) initially developed for no-clay solutions describes well the spin time dependence of the film thickness for no-clay solutions. It allows for the determination of a correct value for the ω_0 in evaporation rate dependence on the spin rate (Eq. 4 in Materials and Methods) based on observations for drying time: a parameter of ω_0 = 50 rpm (e_0=0.075μm/s) produces a film thickness-spin time dependence in which no-clay solutions become dry in about 15 seconds. Other values for ω_0, such as ω_0 = 4 rpm (for ethanol), do not produce good agreement with the experimental data for no-clay solutions. However, even when ω_0 = 50 rpm, the model's predictions do not agree with the experimental data for solutions with clay, as the dotted line shows.

Table 3.1. Fitting parameters for nanocomposite spin cast film thickness versus spin rate dependence. Corresponding graphs are provided in Fig. 1A, 1B. Empirical equations are obtained from fitting the experimental data. The empirical equations are of the form $h = 10^{[A(C_{PS}, C_{clay}) + B(C_{PS}, C_{clay}) \times S]}$, where h is the film thickness in Angstroms, S is spin rate in rpm, coefficients A and B are functions of polystyrene and clay weight fractions and are provided in this table.

PS mass per ml of toluene, mg	Clay mass per ml of toluene	A	B
30	0	3.49043	-4.88E-05
	5	3.60117	-5.71E-05
	10	3.67196	-5.09E-05
	20	4.23295	-9.24E-05
	40	4.80273	-1.15E-04
60	0	4.13296	-6.87E-05
	5	4.2797	-7.18E-05
	10	4.38407	-8.27E-05
	20	4.66485	-9.95E-05
	40	4.9993	-1.23E-04
120	0	4.53688	-5.68E-05
	10	4.6554	-6.58E-05
	20	4.87656	-8.63E-05
	40	5.15718	-1.06E-04

Table 3.2. Fitting parameters for viscosity of polystyrene and clay solutions in toluene as a function of clay weight fraction of polystyrene. The molecular weight of polystyrene is 280K.The graphs were plot for shear rate 100 s^{-1}. The functional dependence is $\eta=10^{[A + B\times f]}$, where η is viscosity in P, and f is the weight fraction of clay from PS in %. The average of all the slopes, except for that of the solution with 120 mg/ml PS, which deviates from the rest of the slopes, is found to be 0.009516. This number is the factor added to the empirical equations for solution viscosity in order to incorporate the effect of clay in solution. When this factor is added, the equations for solution viscosity become:
$\eta=10^{[-2.11991 + 0.01381\times C + 0.009516]}$, if the concentration of polystyrene, C, is less than or equal to 237 mg/ml; and $\eta=10^{[-0.59133 + 0.00231\times C + 0.009516]}$, if the concentration of polystyrene, C, is more than 237 mg/ml.

PS concentration, mg/ml	A	B
30	-1.37159	0.0108
60	-0.52076	0.00863
120	-0.07559	0.01894
240	1.00389	0.01188
480	1.88212	0.01099
960	2.82727	0.00528

Table 3.3. Fitting parameters for film thickness versus time.
$H=10^{[A+\ B\times T]}$Å, where H is the film thickness in Å, and T is the time in seconds. The fitting data for slope B indicate that addition of clay brings more non-linearity into the dependence, but it can still be considered linear within the experimental errors.

Clay concentration, mg/ml	Spin Rate, rpm	A	B
0	2000	3.96329	-6.03E-04
	4000	3.75489	-4.27E-04
	6000	3.63299	1.33E-05
	7720	3.59391	2.11E-05
10	2000	4.76718	-0.00389
	4000	4.50551	-0.00559
	6000	4.27353	-0.00362
	7720	4.23605	-0.00461
20	2000	4.59519	-0.00254
	4000	4.36787	-0.00373
	6000	4.11825	-0.00192
	7720	4.01475	-0.00103

CHAPTER 4.

Model inorganic systems with the multiminimum potential.

§1. Introduction.

The investigated transition-metal complexes, with the $3d^n$ group of iron among them, are the systems with the multiminimum potential. The quantum-mechanical approach used for studying such systems is rather fruitful, it helps in explaining the properties. The properties depend mainly on the interaction of this magnetic center with its first coordination sphere.

The investigated magnetic complexes are the systems whose potential energy has several minima separated by low potential barriers. Such a peculiarity of the potential energy leads to identical temperature dependences of the parameters of systems having different physical origins. As a rule, such systems display low-temperature as well as high-temperature peculiarities in their physical properties.

Among various systems of this type, a crystal with a Jahn-Teller Cu^{2+} ion is studied most thoroughly both from the theoretical and experimental point of view, and hence can be treated as a model system. A detailed analysis of regularities in the behavior of this system will

make it possible to generalize the obtained results for sample of ultrahigh-molecular polyethylene with kaolin-clay.

Moreover, to investigate the EPR spectrum it is the most convenient to use the Fe^{3+} ion as the paramagnetic probe since it is always present in kaolin mineral as an impurity.

The EPR-spectrum of Cu^{2+}-ion in $LiGa_5O_8$-crystal was investigated at $\nu = 9.2407$ GHz and $\nu = 37.15$ GHz over a temperature range of $4.2 \div 300$ K. The temperature dependence of the integral intensity of both the anisotropic and isotropic spectra was studied. On the basis of the dynamic cluster model of the Jahn-Teller effect the spin Hamiltonian parameters were calculated and the analysis of obtained experimental results was carried out. It was shown that the tunnelling splitting for Cu^{2+}-ion in $LiGa_5O_8$-crystal is smaller than 0.005 cm^{-1}. The obtained results lead to the conclusion that the mechanism of temperature variation of EPR-spectrum due to population of excited vibronic states is effective for $LiGa_5O_8$-crystals.

The Jahn-Teller effect is the most vividly manifested in case of the two-fold degenerate ground state of magnetic ion. The Cu^{2+}-ions in octahedral environments are the most wide-spread magnetic center of this type. The action of the Jahn-Teller effect results in lowering of local

symmetry of a magnetic center. The EPR-spectrum of Cu^{2+}-ions is a superposition of the "static" low-temperature spectrum and the "dynamic" high-temperature one. Intensities of these components of the spectrum vary with temperature. The temperature dependence is usually explained in terms of the dynamic averaging model [3, 4], which qualitatively explains the transition from the static to dynamic spectrum as well as parameters of these spectra. The problem of transition from the low-temperature spectrum to the high-temperature one distracted attention from the more detailed investigation of the low-temperature EPR-spectrum. At liquid-helium temperature for majority of crystals, the dynamic averaging process is practically absent and EPR-spectra are determined only by the Zeeman energy and the properties of ground vibronic states. This makes it possible to study the properties of ground vibronic states in their most "pure" form. This makes it possible to define the limits for using the cluster model [5, 6] more accurately. The last model is widely applied to interpret experimental results [7] as well as for computation of states for new systems [8].

The second reason to study the low-temperature spectrum is the interest to the frequency dependence of EPR-spectrum. Already in one of the first papers which considered the "tunnel" splitting [5] it was

found that the vibronic energy levels show a non-linear dependence relative to the external magnetic field. This non-linearity in experiment can lead to the dependence of the g-values on frequency of microwave field. Unfortunately, this striking feature of the Jahn-Teller effect has not been attracted much attention.

In [9] the EPR-spectrum of Cu^{2+}-ion in the $ZnSiF_6 \times 6H_2O$-crystal was investigated at several frequencies. The coincidence of g-values, within experimental error, is excellent. Whether this is a feature characteristic of only Cu^{2+} in $ZnSiF_6 \times 6H_2O$ or of all Jahn-Teller centers, is a question which is still to be answered. This investigation makes it possible to check proposed models and outline new ones.

The paper presents results of a study of the EPR-spectrum of Cu^{2+}-ions in $LiGa_5O_8$ at $\nu = 9.2407$ GHz and $\nu = 37.15$ GHz in a temperature range T = 4.2K-300 K.

§2. Experiment.

$LiGa_5O_8$-crystal with 0.1% of Cu^{2+}-ions was grown by spontaneous crystallization method from solution of oxides in melted salts. The size

of optically homogeneous crystals is 8 mm^3. $LiGa_5O_8$-crystals are of spinel structure [10].

For the investigations X-band EPR-spectrometer was used. The EPR-spectrum is given in Fig.4.1. Curve 1 in Fig.4.1 presents the experimental EPR spectrum for the temperature T= 4.2 K. It is produced with using of the phase detection. Line 1 has unusual form for crystals. Such form is typical of the EPR spectrum of the Cu^{2+} ions in powder. This spectrum can be represented as a superposition of two spectra: anisotropic and isotropic one. At helium temperature the anisotropic EPR-spectrum is in a turn a superposition of three axial spectra, their axes are mutually orthogonal and directed along three four-fold axes (C_4) of the octahedron of oxygen ions forming the first coordination sphere of the magnetic ion [10]. The magnetic field is along one of the C_4 axes of octahedron ligands.

For the study of temperature dependence of integral intensity of spectrum it is convenient to present the EPR data in the form of the absorption spectrum, rather than its derivative. In Fig.4.1 this spectrum is represented by curve 2 obtained by numerical integration of curve 1. The low-field group of four lines of hyperfine splitting corresponds to

the EPR-spectrum of the Jahn-Teller center, whose distortion coincides with direction of the magnetic field. This spectrum can be referred to as "parallel spectrum". The high-field peak represents a superposition of the spectra from two centers, in which the deformation is perpendicular to the magnetic field (referred to as "perpendicular spectrum"). The hyperfine structure of the "perpendicular spectrum" is not resolved.

Between the first (low-field) hyperfine line of the parallel spectrum and the perpendicular spectrum one observes an intense line of isotropic spectrum similar in shape to a "dynamic" EPR-spectrum even at 4.2K. In Fig. 4.1 this absorption line is represented by curve 3, which does not depend on the orientation of the magnetic field. To determine the resonance field and the line width of the absorption line corresponding to the "isotropic" spectrum we carried out numerical modeling of the shape of the absorption line and decomposition into parts for every resonance curve. The result proved that the position in the magnetic field of the "isotropic" EPR-spectrum does not depend on the orientation of the magnetic field, and the g-factor of this line is $g = 2.18 \pm 0.01$.

The anisotropic spectrum presented in Fig. 4.1 by curve 4 is a superposition of three spectra of axial symmetry with mutually

orthogonal symmetry axes. Each spectrum may be described by the spin Hamiltonian with effective spin S = 1/2 and nuclear spin I = 3/2.

$$H = g_{//} \cdot \beta \cdot (H_z S_z) + g_{\perp} \cdot \beta \cdot (H_x S_x + H_y S_y) + A \cdot I_z S_z + B \cdot (I_x S_x + I_y S_y) \quad (1)$$

The axis of symmetry of the magnetic center coincides with the C_4-axis of the octahedron of ligands. The parameters of the spin-Hamiltonian describing the EPR-spectrum of Cu^{2+}-ions in $LiGa_5O_8$-crystals at T = 4.2 K and $\nu = 9.2407$ GHz are $g_{//} = 2.379 \pm 0.005$; $g_{\perp} = 2.074 \pm 0.005$; $A = (100 \pm 2) \cdot 10^{-4}$ cm^{-1}; $B = (25 \pm 2) \cdot 10^{-4}$ cm^{-1}, respectively.

To study the possible frequency dependence of the low-temperature EPR-spectrum the additional investigation of EPR-spectrum at $\nu = 37.15$ GHz was carried out. The parameters of the spin-Hamiltinian obtained at $\nu = 37.15$ GHz are $g_{//} = 2.386 \pm 0.005$; $g_{\perp} = 2.082 \pm 0.005$; $A = (123 \pm 3) \cdot 10^{-4}$ cm^{-1}; $B = (25 \pm 2) \cdot 10^{-4}$ cm^{-1}, respectively.

Increasing of temperature results in a decrease of the integral intensity of the anisotropic EPR-spectrum and the growth of the integral intensity of the isotropic spectrum. The temperature dependence of the

integral intensity of the isotropic EPR-spectrum is given in Fig. 4.2, it can be described by relation:

$$J = J_0 + (1 - J_0) \cdot \exp(-E_0 / kT) \qquad (2)$$

Here $J_0 = 0.63$, $E_0 = 10\ cm^{-1}$. J_0 is an integral intensity of the isotropic spectrum of the Cu^{2+} ion in $LiGa_5O_8$ at T = 0 K.

The effective activation energy E_0 is determined by the height of the potential barrier between the minima of the potential surface of the Jahn-Teller system.

The reason for the appearance of the isotropic line with g-factor equal to 2.18 at T = 4.2 K is associated with the feature of $LiGa_5O_8$-crystal involving cation distribution over sublattices. In the reversed spinel, two-valence metal ions occupy octahedral sites and in the normal one they occupy tetrahedral ones. The structure of a real $LiGa_5O_8$-crystal is intermediate between the normal and reversed spinel structures. Cation disorder of a $LiGa_5O_8$-crystal results in a static deformation distribution. The distribution of static deformations over sites occupied by such impurity as Cu^{2+}-ions results in partial averaging of the anisotropic low-temperature EPR-spectrum. It seems that, the reason for

this is not the dynamic Jahn-Teller deformation of the environment, but the scatter of static deformations.

§3. Discussion.

In [11, 12] it is shown that calculation of the vibronic states of a Jahn-Teller ion in terms of the cluster model [6] gives an expression for the g-value which involves the dependence on the "tunnelling" splitting $\delta E = E_A - E_E$:

$$g_{\parallel} = g_1 + g_2 \cdot C_E / 2 + g_2 \cdot (\sqrt{(C_E - R)^2 + 4 \cdot C_A^2} + \sqrt{(C_E + R)^2 + 4 \cdot C_A^2}) / 4$$

$$R = \frac{2 \cdot (E_A - E_E) \cdot g_{\parallel}}{g_2 \cdot h\nu} \qquad (3)$$

Here $g_1 = g_s - 4\lambda/\Delta$, $g_2 = -4\lambda/\Delta$, g_s is the spectroscopic splitting factor of a free electron, λ is the spin-orbit coupling constant, Δ is the splitting of the ion ground state by an octahedral crystalline field, E_E is the energy of the ground vibronic state transformed by irreducible representation Γ_3 of group O_h, E_A is the first excited vibronic state of symmetry Γ_1. The computation of parameters C_A and C_E, determined in [6], was carried out in [11].

From relation (3) it is seen that the g-value functionally depends on $\delta E / h\nu$. The smaller ν , the greater R in (3) and the greater the contribution of the tunnelling splitting to g-value.

The experimental results obtained by us and presented here show that the g-values of Cu^{2+}-ions in $LiGa_5O_8$-crystals obtained at different frequencies coincide practically within the error of the experiment.

According to our experimental results it may be assumed that the contribution to g-value proportional to $\delta E / h\nu$ does not exceed the error of the measurement $\delta g = 0.005$. This condition allows one to obtain the upper limit for the value of the tunnel splitting δE. Relationship (3) is the dependence $g(\delta E / h\nu)$. Tunnel splitting value $\delta E < 0.005\ cm^{-1}$ is obtained by solving inequality $g(\delta E / h\nu) - 2.38 < 0.005$.

The estimated value of δE is of principal importance, since the parameters of the cluster model [6] are interrelated. According to [6] vibronic states are described by:

$$-\alpha \frac{\delta^2 \phi}{\delta \varphi^2} - \beta \cos(3\varphi)\, \phi = E\phi \qquad (4)$$

$$E = \alpha \cdot \varepsilon$$

Here β determines the barrier height between the minimuma, a determines the difference between the energies of vibronic states.

Function $\phi(\varphi)$ describing the motion along coordinate φ satisfies the equation (4). E is the energy of vibronic states. The reduced energy ε depends only on the ratio β/α.

The form of the dependence $\varepsilon(\beta/\alpha)$ for the several lower vibronic states is given in [11]. The carried out computation gives the dependence $\delta\varepsilon(\beta/\alpha)$ presented in Fig.4.3. ε and $\delta\varepsilon$ are reduced values. The tunnelling splitting δE is related to $\delta\varepsilon(\beta/\alpha)$ as

$$\delta E = \alpha \cdot \delta\varepsilon(\beta/\alpha) \qquad (5)$$

The effective activation energy E_0 is determined by the barrier height between the minimuma of the potential surface. This permits us to estimate the order of the barrier height $\beta \cong E_0 = 10\ cm^{-1}$. If values β and δE are known then $\alpha\delta\varepsilon(\beta/\alpha)$ in relation (5) depends only on parameter α. By solving inequality $\alpha\delta\varepsilon \leq 0.005\ cm^{-1}$ one obtains $\alpha < 0.4\ cm^{-1}$.

With such value of α the vibronic doublet Γ_2 will be distant from the ground state for less than $20\ cm^{-1}$. Increasing the temperature more than ten degrees would populate this level.

On the basis of our results we conclude that the mechanism of transition from the low-temperature spectrum to the high-temperature spectrum induced by population of excited vibronic states is realized for

all crystals, in which g-value of Cu^{2+}-ions in octahedral environments does not depend on the frequency.

The real value of the tunnel splitting δE may be less than the obtained in this work value $\delta E = 0.005 cm^{-1}$. If the order of magnitude of the real value δE is smaller than $0.005 cm^{-1}$ then one needs to take into account all vibronic states.

§4. References.

1. Shapovalov V., Szymczak H., Piechota C., Borowiec M. Jahn-Teller effect in $LiGa_5O_8$ spinel. Molec. Phys. Rep. **5**, 256-260 (1994).

2. Bersuker I.B. Spin inversion levels in a magnetic field and the EPR spectrum of octahedral Cu^{2+} ion complexes. Zh. Exp. Theor. Phys. **44**, 1239-1247 (1963).

3. Ham F. S. : Effect of Linear Jahn-Teller Coupling on Paramagnetic Resonance in ^2E State. Phys.Rev. **166**, 307 (1968).

4. Abragam A., Bleaney B. : Electron paramagnetic resonance of transition ions. (Clarendon Press, Oxford), **V.2**, P.P.350 (1970).

5. Bersuker I. B. : Spin Inversion Levels in a Magnetic Field and the EPR Spectrum of Octahedral Cu^{2+} Ion Complexes. Zh. Exp. Theor. Phys. **44**, 1239 (1963).

6. O'Brien M. C. M. : The Dynamic Jahn-Teller Effect in Octahedrally Co-ordinated d^9 ions. Proc. Roy. Soc. **281**, 323 (1964).

7. Lukin S. N. : Influence of linear compression and temperature at EPR of the Jahn-Teller's sistem Cu^{2+}: $ZnSiF_6 \times 6H_2O$. FTT **339**, 47 (1991).

8. Moate C. P., O'Brien M. C. M., Dunn J. L., Bates C. A., Liu Y. M. and Polinger V. Z. : $H \otimes h$ a Jahn-Teller Coupling that Really does Reduce the Degeneracy of the Ground State. Phys. Rev. Lett., **77**, 4362 (1996).

9. Kozhukhar A. Yu., Lukin S. N. and Tsintsadze G. A. : Exchange pairs of Cu^{2+} ions in zinc fluosilicate. Fiz. Nizk. Temp., **1**, 1535 (1975).

10. Joubert J. C., Brunel M., Waintal A.: A. Durif Comp. Rend. **256**, 5324 (1963).

11. Vasyukov V. N.: Dependence of the Low Temperature EPR Spectrum of Cu^{2+} Ion on the Microwave Field Frequency and Temperature. Phys. stat. sol. (b) **137**, 623 (1986).

12. Vasyukov V. N., Suharevskij B. Ya. : The Energy Spectrum of Vibronic States of Jahn-Teller's Ion. Fiz. Nizk. Temp. **20**, 821 (1994).

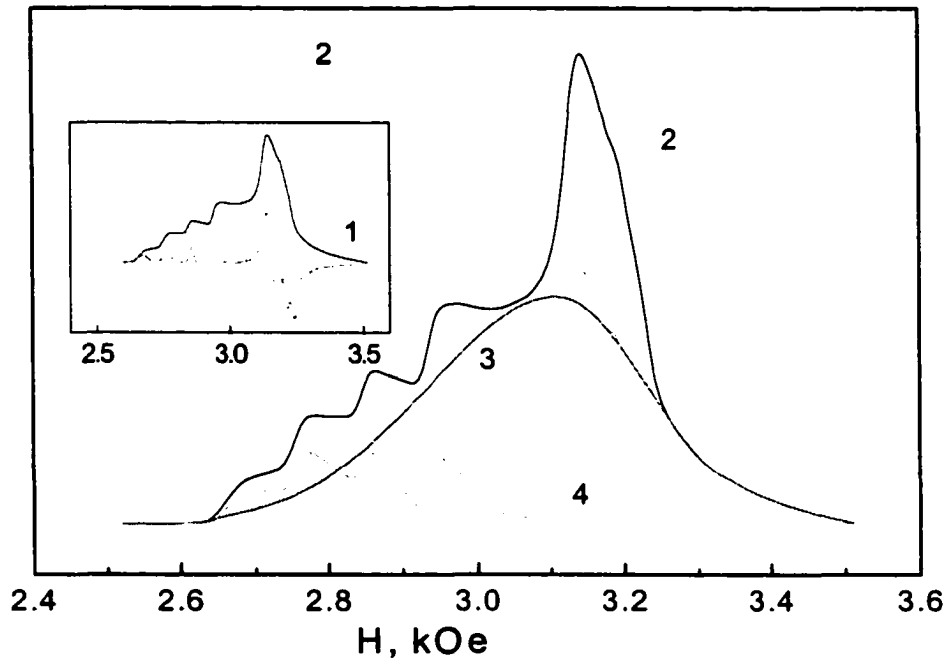

Figure 4.1. EPR spectrum of Cu^{2+} ion in $LiGa_5O_8$ crystal at T=4.2K; $H//C_4$: 1-experimental spectrum; 2-integrated spectrum; 3-isotropic spectrum; 4-anisotropic spectrum.

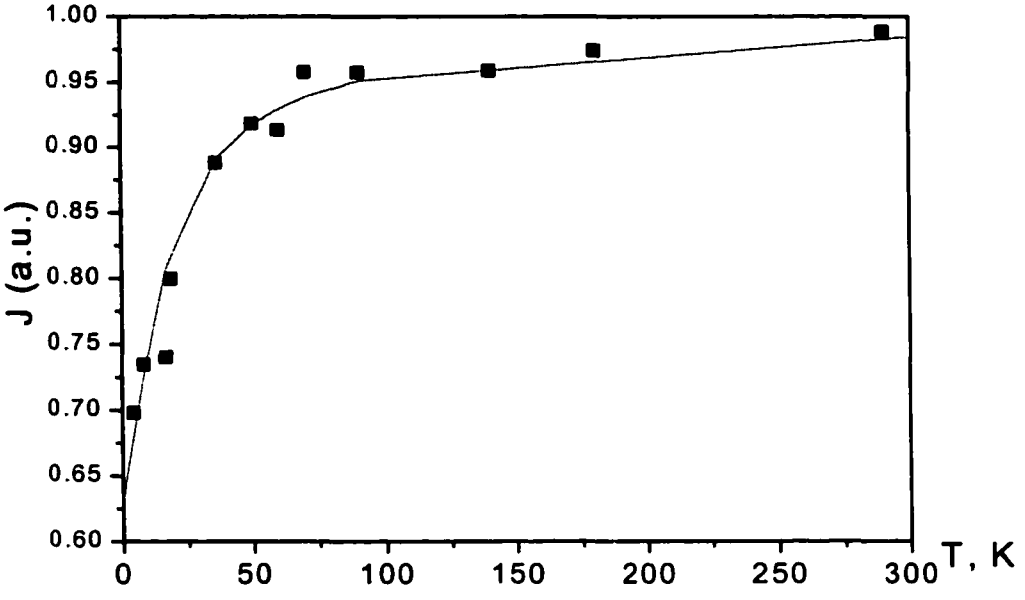

Figure 4.2. Temperature dependence of the integral intensity (J) of EPR isotropic spectrum of $LiGa_5O_8 : Cu^{2+}$; $H//C_4$.

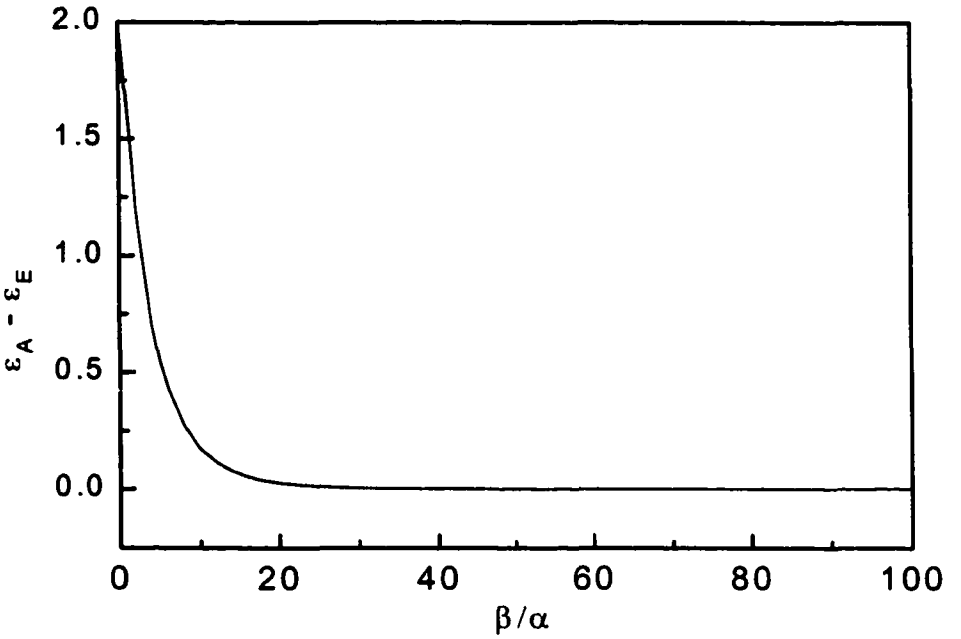

Figure 4.3 Dependence of "tunnel" splitting on β / α.

Chapter 5.

Problem of the kaolinite-plate ordering in polyethylene

§1. Material for specimens.

We used SIMS to investigate the behavior of clay particles in thin polymer films. The results of preliminary measurements have shown that in such films the clay particles turn as a result of different influences (e.g. after the annealing). Besides, there were a number of uncertain questions, in particular, to what extent the clay particles are ordered in the investigated samples. The problem on the clay particle ordering and their diffusion into the polymer turned out to be so complex that it could not be solved by SIMS methods. So, we have to use additional methods and investigations that are described below.

The investigated problem is of high scientific and engineering importance. For example, the investigation of the problem will help in the improvement of quality and lowering the cost of tires, etc.

Polymer systems, which are polymeric compounds and filled compositions, offer high potentialities for the control of physical and mechanical properties. Due to this feature of polymer systems there has been an increased interest in those materials during recent years. Kaolin is widely used in producing the filled polymeric compositions [1-4]. The

"Dupon" company (USA) has published a number of articles on polymerization filling of ultrahigh-molecular polyethylene with inorganic fillers [1]. Kaolin addition to a polymer reduces the relative fraction of the latter in final product, thus reducing its cost and enabling one to produce materials with new complex of properties. We investigate a composition (ultrahigh-molecular polyethylene + 27% of kaolin) which possesses high wear resistance, high impact strength and hardness. It also resists radiation and attack by acids, alkalies and many organic solvents. The material can be used in a wide temperature range. It is frost- and impact-proof. The material is notable for the improved antiadhesive and anticorrosive properties, reduced cold flow, creep and friction coefficient. After aging for 1500 hours at 90^0C the rupture strength and plasticity were preserved at a former level. Compositions of a thermosetting plastic material with a filler containing crystal water possess reduced combustibility and the ability of self-extinguishing. Kaolin is a finely dispersed clayey rock. It is in the form of aggregates of pseudohexagonally outlined thin kaolinite plates of several microns in size and possessing rather perfect cleavage. The physical properties of the composite and final product highly depend on the character and degree of the kaolinite plate ordering. In powder sample, the kaolinite

plates are disordered to the maximum. An alternative is the sample in which the whole of kaolinite plates are superimposed with their cleavage planes one onto another to form a three-dimensional crystal structure.

The development of methods for the producing of composite polymeric materials with different degree of the kaolinite plate ordering is of high interest. One of the most prospective methods of producing such materials is the solid phase extrusion under which the polymer is at a time influenced by high pressure and shear stresses [4, 5]. To compare the physical properties of the produced material with the character and degree of the kaolinite plate ordering one has to develop methods making the investigation of the ordered plates possible.

The present work is aimed at studying the extruded specimens of kaolin-filled high-molecular polyethylene. This study is needed to determine a relationship between physical properties of specimens and the character and degree of the kaolinite plate ordering. We are planning to use the methods of electron paramagnetic resonance (EPR) spectroscopy and X-ray diffraction. When investigating an EPR spectrum it is more convenient to use the Fe^{3+} ion as a paramagnetic probe. It is always present in mineral kaolin as an impurity.

Moreover, to investigate the EPR spectrum it is the most convenient to use the Fe^{3+} ion as the paramagnetic probe since it is always present in kaolin mineral as an impurity.

The investigated transition-metal complexes, with the $3d^n$ group of iron among them, are the systems with the multiminimum potential. The quantum-mechanical approach used for studying such systems is rather fruitful, it helps in explaining the properties. The properties depend mainly on the interaction of this magnetic center with its first coordination sphere.

The investigated magnetic complexes are the systems whose potential energy has several minima separated by low potential barriers. Such a peculiarity of the potential energy leads to identical temperature dependences of the parameters of systems having different physical origins. As a rule, such systems display low-temperature as well as high-temperature peculiarities in their physical properties.

Widely used composite material (CM) consisting of ultrahigh-molecular polyethylene and kaolin is taken as the investigation object. It is planned to use kaolin of dry enrichment having the following characteristics: content of the water-soluble salts - not higher than 0.1%, reaction of aqueous extract pH=5.5-6.5; moisture content- not higher

than 0.7%; bulk density -220 kg/m^3. Kaolin plates are 5-15 microns in size.

Kaolin is based on kaolinite $Al_2[Si_2O_5]\cdot(OH)_4$. Kaolinite crystalline structure consists of two-layer packets containing one tetrahedral silicon-oxygen layer of composition $[Si_{2n}O_{5n}]^{2n-}$ and one alumo-oxygen-hydroxylic layer of composition $[Al_{2n}(OH)_{4n}]^{2n+}$ [6, 7]. The both layers form a packet by means of common oxygen atoms from the silicon-oxygen layer.

Kaolinite is a mineral from the class of silicates $Al_4[Si_4O_{10}]\cdot(OH)_8$. It is in the form of loose latent crystalline aggregates consisting of separate small plate-like pseudohexagonal crystals of 0.2 to 15 microns. The density makes 2630 kg/m^3. Small crystals are in the form of thin scales. Cleavage along (001) is rather perfect [6, 7]. The layers are superimposed one onto another the same as in micas. Natural kaolinite minerals have impurities usually in the form of iron. Kaolinite lattice is of the typical layer type. And also, the 2/3 of the octahedral free space is occupied by Al^{3+} which is partially substituted by Fe^{3+}. The tetrahedral free space of kaolinite is only occupied by Si^{4+}.

Kaolin single crystal is a two-layer silicate of alumina containing hydration water and consisting of chemically bonded layers of silicon

dioxide and hydrated aluminium oxide. Under formation, some single crystals can join together thus forming relatively large particles. The particles with the equivalent-sphere diameter (ESD) of about 10 microns and more are packs of plate-like crystals of the height approximately equal to their average diameter. For particles of smaller size the length-to-diameter ratio depends on ESD and grinding method. The particles with ESD of about 2 microns and less are thin plates having diameter, which is 4-10 times as much as their thickness. Finely ground kaolin has scales which are 0.05 micron thick and of 0.3-0.4 micron diameter, but diameter of the particles varies more frequently from 1 to 10 micron. The agglomerating of kaolin particles is the consequence of its two-layer structure and highly active radicals originating when the bonds of lateral surfaces of the crystals are broken. The smaller the particle size, the more intensive the agglomeration.

§2. Method of polymerization filling.

The conventional method of filling the polymer composites is in the mechanical mixing of components. However, a material produced by mechanical mixing has, as a rule, the modulus of elasticity that is lower as compared with a material produced by the polymerization filling

technique. Such material fails under large temperature differences.

One of the prospective methods of introducing fillers is the polymerization filling when the polymer compositions are formed just during polymer synthesis. For its realization there should be active centers on filler surface [8]. This method is of high advantage over the conventional mechanical mixing. It enables one to produce materials possessing new properties and filler being uniformly distributed in the polymer matrix. In a number of cases, the material can be only produced due to the polymerization filling technique. For example, in case of temperature rise the fillers oxidize easily and lose their properties. The strongly bound polymer cover around each filler particle can bring some new physical phenomena in composite materials. This cover makes it possible to considerably improve the parameters of materials as compared to those obtained by conventional mechanical mixing and to extend the range of application for the composite polymer materials.

The essence of the method is in the producing of filled polymer composites by polymerization of monomers or monomer mixture on the surface of catalytically activated fillers, i.e. directly during the polymer synthesis.

There are three main stages in the process of producing the

polymerization-filled CM. They are the preparation of filler, the creation of active centers on filler surface, and the polymerization of monomers on filler surface resulting in the covering of filler particles with polymer layer of controllable thickness.

Under the polymerization filling the matrix polymer is distributed over filler particles. The uniform surface distribution of the polymer results in the uniform distribution of filler in polymer matrix even in highly filled polymer materials. During the polymerization, the polymer is formed not only on the outer surface of the filler but inside the pores and microcracks. As a result, the area of filler-polymer matrix contact increases considerably.

Polymerization can take place by the ion-coordination, radical or ionic mechanism depending on the character of active centers used.

Preparation of fillers for the polymerization filling by ion-coordination method consists in removing compounds such as H_2O, O_2, CO_2, CO, SO_2, NH_3 and others, which inhibit the polymerization process, from the surface or bulk of the fillers. For this purpose a special drying, the vacuum treatment and the inert-gas blowing under different temperature conditions are used.

Presence of surface reactive groups in silicate structures allows

one to chemically modify those compounds. The chemical modification of silicates consists in a complete or partial substitution of reactive atoms and groups for organic groupings. The modification occurs on the surface, the inner structure of the silicate remained conserved. The polymer and the added silicate filler form a unified heterogeneous system with the polymer (organic) and silicate (inorganic) phases uniformly distributed over the volume. This system is called a composite material. Next, the polymerization of any selected vinyl monomer, e.g. styrene, is performed in the presence of silicate with unlimited surface groupings bonded to its surface. As a result, due to polymerization the organic polymer chains are connected to alkenyl groups, i.e. a grafted copolymer of silicate and organic polymer is formed.

The polymerization filling by ion-coordination polymerization is realized by means of complex metallic or organometallic catalysts bonded to filler surface. Complex catalysts are fixed on the filler surfaces by a physical or a chemical method. In the first case, on filler surface or in its pores the solid phase of transition-metal derivatives is formed by precipitating the transition-metal compounds in different ways. With such technique, the catalytic solid phase can be formed on

surface of fillers free from the functional groups. The chemical methods of bonding are based on the interaction between transition-metal compounds or organometallic compounds with the reactive groups on filler surface, in particular, with the hydroxyl groups which could be transformed to active polymerization centers by means of corresponding reactions.

The deficiency of free hydroxyl groups and a considerable amount of the alkali-metal compounds (K_2O, Na_2O) on filler surface prevent the obtaining of the catalyst, which is active at polymerization. The very nature of filler surface inhibits the polymerization process when producing PE-containing composite materials by polymerization filling. The excessive OH-groups or high acidity of filler surface can also negatively influence the polymerization process and retard the process. The concentration of OH-groups on filler surface is controlled by thermal and chemical preparation.

The activation of filler, i.e. fixing of polymerization catalyst at filler particles can be done from catalyst's vapor phase in vacuum in the stream of an inert carrier gas or from solution in the medium of an organic solvent.

In the case of CM (UHMPE+kaolin) under consideration, the pre-

dried kaolin was specially treated to be used in the polymerization process. The catalysts were petrol solutions of $TiCl_4$ and $Al(C_2H_5)_2Cl$. Polymerization of ethylene was done in petrol in the presence of kaolin.

§3. A technique of the kaolinite-plate ordering in polyethylene.

The main principle of producing superoriented specimens is in the longitudinal deformation of the polymer. The solid-phase extrusion under which the polymer is at a time influenced by high pressure and shear stresses is one of the most effective methods of producing such materials [4, 5].

Under the process, the billet is fed through a narrowing die under the action of high pressure transmitted by liquid or specimen itself. To estimate a degree of pressure effect, the nominal extrusion ratio λ is usually used. This is the ratio between cross section area of the billet and the die opening.

The investigation specimens will be prepared by the plunger extrusion method with a setup mounted on a 100-ton vertical hydraulic press. The setup includes a high-pressure vertical container, a plunger and a deforming die located in the bottom of container bore. The plunger velocity is 2 mm/s. Powder of the ultrahigh-molecular

polyethylene with kaolin filler content of 27% was compacted in a mould to produce billets for the extrusion. The produced specimen is fed to high-pressure container. Container with the specimen and the die are heated to 393K that corresponds to $0.9 \cdot T_m$ ($0.9 \cdot T_m$ is the temperature of UHMPE melting) and is fitted experimentally. Under hydroextrusion at temperature lower than 393 K the specimen failed. At a higher temperature ($0.9 \cdot T_m$) the specimen lost its shape. The extrusion ratio is calculated by the formula

$$\lambda = d^2_c / d^2_d ,$$

where d_c and d_d are diameters of container and die, respectively. It is expected that λ will be in the limits of 1 to 7.

The shaping of specimens is as follows. Polymer block specimen is transformed to plastic state due to heating to $0.9 \cdot T_m$. At the next stage the specimen is transformed to a viscous filament, which is to be solidified next. Viscous filament is a labile system, so it should be quickly solidified (fixed). As a result, the viscosity is simply increased to a value providing very low irreversible deformation with a preset load for the filament.

The kaolinite plates become oriented due to the orientational

pressure along container axis. At low pressure, i.e. at low shear stresses the specimen preserves its perfect cylindrical shape (Fig. 4.1a). The angle of misorientation of the plates with respect to cylinder axis is rather large. Misorientation value limit approaches the chaotic orientation inherent in powder. With the increase in pressure and extrusion ratio, on cylinder surface there occur aperiodic nonuniformities (Fig. 4.1b). A subsequent increase in the extrusion ratio results in spiral- or wave-like distortions (Fig. 4.1c). Finally, at very high shear stresses the cylinder breaks into separate fragments (Fig. 4.1d).

A general mechanism of the kaolinite plate orientation is in the following. It is known [5] that for orientation along certain axis of any anisometric element of the structure the system should be deformed. After the obtaining of a necessary orientation it is fixed. In our case, such a fixation occurs due to natural cooling when polymer goes out of the die.

§4. Techniques used to analyze the character and degree of the kaolinite-plate ordering.

We are planning to apply the EPR spectroscopy and the X-ray

diffraction methods to study the character and degree of the kaolinite-plate ordering. This gives us a possibility to estimate misorientation of kaolinite single crystals with respect to cylindrical specimen axis.

It is prospective to apply the electron paramagnetic resonance for studying the character and degree of the kaolinite-plate ordering in the extruded specimen because of a number of reasons. First, it is important that polymeric matrices do not, as a rule, contain magnetic impurities. As a result, the polymer itself does not at all contribute to the EPR spectrum or the EPR resonance line is low intensive. As a rule, the resonance line of polymer EPR spectrum is due to the presence of free radicals. The line is, as a rule, described by the effective g-factor approximately equal to 2.0. On the other hand, Fe^{3+} magnetic impurities are always present in kaolin. The iron content of kaolin makes usually 0.3 to 0.I% depending on a deposit [9]. Those impurities substitute the Al^{3+} ions, which are the components of kaolinite structure. The Fe^{3+} ions are paramagnetic probes enabling one to investigate the electric crystalline field acting on them. Symmetry of the crystalline field acting on the magnetic ion characterizes the structure of the nearest crystalline environment. Study of the dependence of EPR spectrum on orientation of the external magnetic field helps in determining the direction of the

axis of symmetry for the magnetic center. Direction of the axis of symmetry of the magnetic center is, in turn, related to the crystalline structure of kaolinite. The crystalline structure is dependent upon kaolinite plate cut. Thus, the study of Fe^{3+} EPR spectrum in the extruded specimen makes it possible to determine the orientation of kaolinite plates.

The angular dependence of the EPR spectrum enables one to study not only the character of the kaolinite plate ordering but a degree of the ordering. The character of ordering is associated with a preferable direction of the kaolinite-plate orientation, it will become apparent owing to the direction of maxima in the angular dependence of the resonance field of EPR spectral line. The degree of ordering is found as a ratio between a number of kaolinite plates oriented in the selected direction and a total number of plates. This information can be obtained by resolving the resulting EPR line into components. The integrated intensity of line component which is independent of magnetic-field orientation defines the number of magnetic centers in kaolinite disordered plates. The integrated intensity of the resonance line component which is dependent upon the external magnetic field orientation defines the number of magnetic centers in kaolinite plates

oriented in a preset direction.

The using of Fe^{3+} ion as a paramagnetic probe makes the problem of studying the kaolinite-plate orientation to a considerable degree simpler. The matter is that the low-temperature Fe^{3+} EPR spectrum is a resonance line described by the effective g-factor approximately equal to 4.3. It is much higher than the g-factor value of 2.0, which is characteristic of the resonance line of radicals. If in the specimen there are the polymer radicals, then their resonance line does not overlap the resonance line of Fe^{3+} ion and so it does not interfere with studying the angular dependence of the EPR spectrum.

Investigations of Fe^{3+} EPR spectrum in kaolinite done in articles [10, 11] show that at low temperature the crystalline environment of the magnetic ion is highly distorted. Parameter of spin Hamiltonian D describing the axial distortion of crystalline environment is much larger than quantum hν of the high-frequency field ($D >> h\nu$). Under such condition a variation in external magnetic field orientation results in a considerable change in the resonance field of the EPR-spectrum line.

The application of the X-ray diffraction to study the orientation of kaolinite plates becomes simpler since the structure of kaolinite itself has been already investigated [6, 7]. Studies of diffraction from the

lateral layer of extruded-sample cylindrical surface and from the end face layer provide the information on the character of the kaolinite plate orientation near specimen surface. Comparison of the so-obtained information with that obtained by the EPR method provides a more useful picture, since the EPR spectrum contains the contribution not only from the magnetic centers of the near – surface kaolinite crystals, but from those in the bulk of the extruded specimen.

§5. References.

1. E. G. Howard, R. D. Lipscomb, R. N. MacDonald, B. L. Glazar, C. W. Tullock and J. W. Collete, Homogeneous Composites of Ultrahigh Molecular Weight Polyethylene and Minerals. 1.Synthesis, Ind. Eng. Chem. Product. Research and Development **20**, 421-428 (1981).

2. Y. T. Lim and O. Ok Park, Rheological evidence for the microstructure of intercalated polymer/layered silicate nanocomposites, Macromol. Rapid Commun. **21**, 231-235 (2000).

3. M. Alexandre and P.Dubois, Polymer – layered silicate nanocomposites: preparation, properties and uses of a new class of materials, Materials Science and Engineering **28,** 1-63 (2000).

4. V. A. Beloshenko, G. V. Kozlov, V. N. Varyuhin and V. G. Slobodina, Properties of ultra - high-molecular polyethylene and related polimerization-filled composites produced by solid-state extrusion, Acta Polimer **48,** 181-187 (1997).

5. Ultra – high modulus polymers. Edited by a Ciferri and I. M. Ward. Applied Science Publishers. London. (1979).

6. Hugo Strunz, Mineralogische tabellen, Leipzig, Academische Verlagsgesellschaft Geest, Portig K.-G., P.P. 532 (1957).

7. Alexander Newton Winchell and Horace Winchell. The microscopical characters of artificial inorganic solid substances: optical properties of artificial minerals. Academic Press, New York and London, P.P. 402 (1964).

8. R. L. Adelman, E. G. Howard, Pat. 41511226, USA.

9.V.V. Mank, F.D. Ovcharenko, L.V. Golovko, N.G. Vasilyev and A.Ya. Karushkina, On nature of stable radicals in kaolin, DAN SSSR **223**, 389-392 (1975).

10. V. N. Vasyukov, V. V. Shapovalov, S. A. Schwarz, M.H.

Rafailovich, J. C. Sokolov, V. A. Shapovalov, V. A. Beloshenko. Temperature-induced changes in the EPR spectrum of the magnetic center in kaolin. Journal of Magnetic Resonance **154**, 15-21 (2002).

11. V. V. Shapovalov, V. N. Vasyukov, M. H. Rafailovich, J. C. Sokolov, S. A. Schwarz, Nan-Loh Yang, V. A. Shapovalov, V. A. Beloshenko. Plastic deformation-induced orientation of kaolinite crystals in ultrahigh-molecular polyethylene. (Journal Magnetic Resonance, in press-2002).

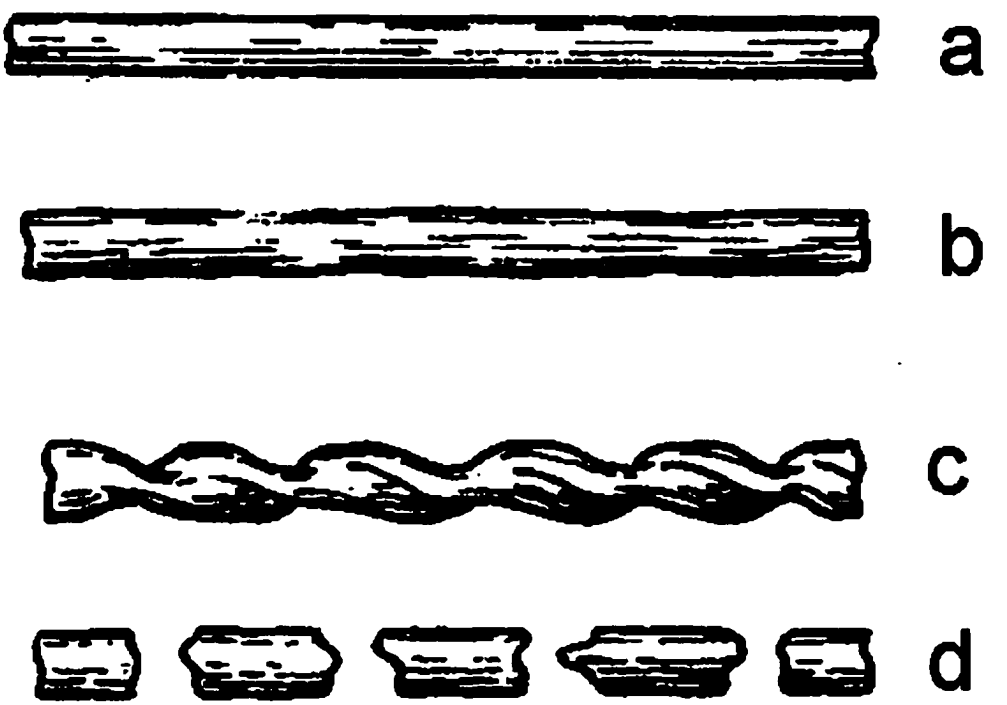

Figure 5.1. Transformation of sample shape with the increase in the extrusion ratio.

Chapter 6

Temperature-induced changes in the EPR spectrum of the magnetic center in kaolin and montmorillonite.

§1. Introduction.

Studies of kaolin have revealed an effect characterized by an unusual temperature-induced change of the EPR spectrum of Fe^{3+} ion, which is the magnetic probe in kaolin-clay. At low temperature (T=4.2K) a resonance line with an effective g value $g_1 = 4.13 \pm 0.16$ is observed. At high temperature (T=288K) one observes a resonance line with the effective g factor $g_2 = 2.15 \pm 0.1$. The transition from the low- to high-temperature spectrum is gradual and it is accompanied by a redistribution of the absorption intensity. The observed properties of the temperature dependence of the EPR spectrum are characteristic of systems with a multiminimum potential.

Kaolin is widely used in the formation of filled polymeric composites [1-4]. The addition of kaolin to a polymer reduces the relative fraction of the latter in the final product, thus reducing its cost and enabling one to obtain materials with a new complex of properties. One method of polymer loading with filler is polymerization filling,

where the polymeric compositions are formed directly during synthesis of polymer. For its realization there should be active centers on the filler surface. Kaolin, which is widely distributed in nature, possesses such centers; iron in particular.

A peculiarity of the Fe^{3+} magnetic centers is the presence of a nontraditional temperature dependence of the EPR spectrum. Recently [5], such a temperature dependence has been observed in organic materials essentially differing in composition and structure. Their EPR spectrum is a superposition of low- and high-temperature spectra. When the temperature is changed, the absorption intensity is redistrubuted between the low-temperature and high-temperature spectra. This is evidence of unusual dynamics of the molecules surrounding the Fe^{3+} ion whose presence can substantially influence different properties of the substance.

Research on these dynamic transitions is of additional interest, since the systems exhibiting such properties are, as a rule, systems with multiminimum potentials. The motion of molecules occurs in the potential well with several minima. Such systems have not been adequately investigated experimentally. The best studied is the Jahn-Teller system of a divalent copper ion in an octahedral environment [6,

7]. In that case, the three potential wells of equivalent energy are determined by the Jahn-Teller interaction of the doubly - degenerate orbital state with the tetragonal deformations of the octahedral environment. Crystalline methane is an example of a physically different kind of system with a multiminimum potential [8].

The peculiarities of the EPR spectrum described in paper [5] have been investigated in materials with the described molecular structure. One may believe that the above peculiarities are only typical of organic compounds. Therefore, in this paper, the Fe^{3+} EPR spectrum has been investigated in kaolin, a typical inorganic substance. The investigated kaolin, with a particle size of 5 to 15 μm, is the filler in ultra-high-molecular polyethylene. The conditions for obtaining this composite, as well as its physical and mechanical properties, are described in paper [4].

Kaolin is based on kaolinite $Al_2[Si_2O_5](OH)_4$ with the crystalline structure consisting of two-layer packets containing one tetrahedral silicon-oxygen layer of composition $[Si_{2n}O_{5n}]^{2n-}$ and one octahedral alumo-oxygen-hydroxylic layer of composition $[Al_{2n}(OH)_{4n}]^{2n+}$ [9]. Both layers form a packet by means of common oxygen atoms from the silicon-oxygen layer. The kaolinite space group is C_i^1 ($P\bar{1}$) with the unit

cell parameters $a_0 = 5.14$; $b_0 = 8.93$; $c_0 = 7.37$ Å; $\alpha = 91.8^0$; $\beta = 104.5^0$. The iron content of kaolin is 0.3 to 1.1%, depending on the deposit of origin [10].

Fig. 6.1 shows the nearby environment of Al^{3+} ions. It is in the form of octahedrons of two types consisting of two oxygen atoms and four OH groups. The magnetic Fe^{3+} ion substitutes the Al^{3+} ion isovalently. It is seen from Fig.6.1 that the magnetic Fe^{3+} ion can be in two nonequivalent positions.

§2. Results.

The spectrum of powder samples was studied on an EPR spectrometer with the frequency of the microwave field $\nu = 9.247 \pm 0.001$ GHz in the temperature interval T=4.2-288K.

The EPR spectrum for T= 4.2 and 288K is shown in Fig.5.2. It consists of a set of narrow and broad lines. The narrow line (ΔH=I7 Oe) with the effective g value g=3.5 pertains to the Cr^{3+} ion which was used to calibrate the magnetic field. The narrow line with $g \approx 2$ corresponds, according to [11], to the O_2^- ion existing on the cleavage plane of the mineral. Two broad lines with $g_1 \approx 4.1$ and $g_2 \approx 2.1$ pertain to the Fe^{3+} ion, which is usually present in mineral kaolin as an impurity. A partial

splitting of line 1 observed in Fig.6.2a is apparently connected with the two nonequivalent positions of the magnetic ion. The g value of line 1 at T=4.2K is $g_1 = 4.13 \pm 0.16$. That of line 2 at T=288K is $g_2 = 2.15 \pm 0.1$.

Lines in the EPR spectrum of Fe^{3+} are of appreciable width, changing with temperature in an unusual manner, so it is more convenient to represent the EPR spectrum in the form of the absorption curve, rather than its derivative. The latter is usually recorded using phase detection. Fig.6.3 shows such an EPR spectrum for seven values of the temperatures T=4.2, 9.26, 50, 100, 202, 288K. It is seen that when the temperature is increased, the intensity of resonance line 1 decreases, whereas line 2 becomes more intense. The g values for the resonance lines do not depend strongly on temperature. When the temperature is changed from 288 to 4.2K, g_2 decreases from 2.15 ± 0.1 to 2.0.

The temperature dependence of the total integral intensity of both resonance lines in the EPR spectrum of Fe^{3+} is shown in Fig. 6.4. The solid line describes the dependence $J(T) = J_0 \tanh(h\nu/2kT)$. When comparing the experimental values of the total integral intensity with the dependence $J(T) = J_0 \tanh(h\nu/2kT)$, one can conclude that in kaolin, the temperature dependence of the Fe^{3+} EPR spectrum is determined by two mechanisms. The first mechanism leads to a usual decrease of the

integral intensity of both resonance lines when the temperature is growing. It is determined by the temperature dependence of the difference of the population in the resonance states. The second mechanism results in a redistribution of the absorption intensity between lines 1 and 2 (Fig.6.3).

The process of intensity redistribution is more clearly shown in Fig.6.5. The figure demonstrates the temperature dependence of the reduced integrated intensities J_1, J_2. For each value of the temperature their sum is constant $J_1 + J_2 = 1$. These dependences can be described as

$$J_1 = 0.33 \cdot (1 - \exp(-E_0 / kT)) \qquad (1)$$

$$J_2 = 1 - J_1$$

where k is the Boltzmann constant, $E_0 = 40 \pm 10\ cm^{-1}$ is the effective activation energy.

It should be noted that the intensity of line 2 at T=4.2K is greater than zero, unlike the results of [5]. The mechanisms of initiation of the temperature-independent and temperature-dependent contributions are, possibly, of a different physical nature.

In [5], line 1 is referred to as the "low-temperature" EPR spectrum of the Fe^{3+} ion and line 2 as the "high-temperature" spectrum. In the case of kaolin, these terms can only be used for the temperature-dependent

contribution of each line. The temperature change results in a redistribution of the absorption intensity between the low- and high-temperature spectra.

The unusual change of the spectral line intensities is not the only peculiarity. Fig.6.6 shows the temperature dependence of the line widths at half-height. According to Fig.6.6, the width of line 1, ΔH_1 does not depend within the measurement error on temperature and equals 0.55 ± 0.1 kOe. At T=288K, the width of line 2, H_2=1.58k0e. When the temperature is decreased, the width of line 2 grows exponentially to a value of 2.26 k0e at T=4.2. The broadening of line 2 is accompanied by the lowering of the integral (and peak) intensities. It should be stressed that the ordinary mechanism of the EPR-spectrum resonance line broadening, due to the relaxation spin-lattice processes, results in the increase of line width when the temperature is increased. The inverse temperature dependence of this parameter, observed experimentally, testifies to an additional and more efficient mechanism determining the width of the EPR resonance line. The behavior of the intensities of lines 1 and 2 and the above arguments are sufficient grounds to conclude that lines 1 and 2 are interrelated.

§3. Discussion.

The described EPR spectrum of Fe^{3+} in kaolin has a number of features that must be considered separately:

1. First, we have to analyze the values of g factors of the resonance lines 1 and 2 which belong to the iron impurity ion. The Fe^{3+} ion has the configuration d^5. The spin of the ground state is S=5/2. For the most frequently encountered EPR spectra of Fe^{3+}, the typical g value is close to 2.

On the other hand, a resonance line with the g value close to 4.3 has been analyzed in a number of studies [12-15] of the EPR spectrum of iron ions in silicate glasses. There is no long-range order in the glasses as well as in the kaolin powder investigated by us. In kaolin, the lines 1 and 2 were observed by authors of [10, 11, 16]. Article [17] gives a detailed analysis of the EPR spectrum of iron ions in amorphous materials. It is assumed in this article that the spectrum consisting of two resonance lines with $g\cong 2$ and $g\cong 4.3$ belongs to different nonequivalent magnetic centers of the Fe^{3+} ion. The centers differ in the value of the low-symmetry component of the crystalline field acting on the magnetic ion. The authors of article [17] assume that the line with $g\cong 2$ corresponds to a center for which the low-symmetry component of the crystalline field is much less than the Zeeman energy. The line with

g≅4.3 corresponds to a center for which the low-symmetry component of the crystalline field is much larger than the Zeeman energy. Both cases are considered in items 2 and 3 in more detail.

2. If the electric field of the nearest environment of the magnetic ion Fe^{3+} is of the cubic symmetry or the low-symmetry component is much less than the Zeeman energy, then the Hamiltonian of the zero approximation will be in the form

$$H_0 = g_0 \cdot \beta \cdot \mathbf{H} \cdot \mathbf{S} \qquad (2)$$

where β is the Bohr magneton, g_0 is the g value of the ground-state multiplet S=5/2. The numerical value of g_0 is close to 2.0. The Hamiltonian of fine-structure splitting should be considered as a perturbation. In this case, the EPR spectrum of the magnetic center consists of five lines. The central resonance line does not, as a rule, depend on the direction of the magnetic field and corresponds to a transition +1/2 ⟷ -1/2. The other four resonance lines of the fine structure of the spectrum depend on the magnetic-field direction. In a "polycrystalline" sample, a single resonance line will be observed with the effective g value equal to that of the resonance transition +1/2 ⟷ -1/2 and having a value g≅ 2. The resonance lines of the other transitions of the fine structure of Fe^{3+} are averaged as a result of the orientational

disordering and will contribute to the line width.

3. If the low-symmetry component of the electric field of Fe^{3+} nearest neighbor environment is much greater than the Zeeman energy, then according to [17], the Hamiltonian of the zero-order approximation should be in the form

$$H_0 = D\cdot(S_z^2 - S(S+1)/3) + D\cdot(S_x^2 - S_y^2)/3 \qquad (3)$$

The Zeeman Hamiltonian (2) and the Hamiltonian of the fine-structure splitting (4):

$$H_1 = (E - D/3)\cdot(S_x^2 - S_y^2) \qquad (4)$$

should be considered as a perturbation. Here S_x, S_y, S_z are components of the spin operator; D, E are parameters of the zero splitting, which characterize the field of axial symmetry and the rhombic component of the field, respectively. The action of Hamiltonian (3) splits the spin multiplet S=5/2 into three Kramers doublets with energies $\varepsilon_1 = 0$; $\varepsilon_2 = 4\sqrt{7}\,D/3$; $\varepsilon_3 = -4\sqrt{7}\,D/3$. It has been estimated [17] that the lower and upper doublets have highly anisotropic g tensors, while the g value of the middle doublet is isotropic and approximately equal to $g \cong 4.3$. In a "polycrystalline" sample, the axes of symmetry of different magnetic centers are randomly oriented in different directions with respect to the magnetic field. As a result, the EPR spectrum of the doublets with the

anisotropic g tensors is "smeared" over a wide range of magnetic fields and can not be observed experimentally. Only resonance line 1 with g≅4.3 is observed.

4. The transition from the low-temperature spectrum to the high-temperature one occurs not in a jump-like manner, but gradually (Fig.6.3). Therefore, the structural phase transitions cannot cause the change in the intensity of the EPR spectral lines.

5. In articles [10, 11, 16, 17] it is assumed that the spectrum consisting of two resonance lines with g values g≅ 2 and g ≅ 4.3 belongs to different nonequivalent magnetic centers of the Fe^{3+} ion. It is believed [11] that line 1 corresponds to Fe^{3+} ions which are impurities in the kaolinite structure and substitute the Al^{3+} ions. Line 2 corresponds to Fe^{3+} ions which are in the structure of another mineral component of kaolin. Besides, in the kaolinite structure, there are two nonequivalent positions for the trivalent ion. Despite the magnetic ion having the ability to occupy nonequivalent positions, it is hardly probable that the temperature changes could induce real displacements of Fe^{3+} ions from one nonequivalent position to another.

6. In the high-field part of resonance line 2 of the EPR spectrum of Fig.6.3 (T=4.2, 9, 26K) one can see the maxima rather well. The

maxima are typical of the EPR spectrum which is averaged over directions of the magnetic field. Fig. 6.7 shows the structure of energy levels of the multiplet S=5/2 and the EPR spectrum for T=4.2K. The resulting form of line 2 averaged over magnetic field directions has 5 maxima. The central maximum corresponds to transition $1/2 \longleftrightarrow -1/2$. The other maxima correspond to another four transitions and appear as a background of the averaged line 2. The two high-field maxima correspond to transitions $-1/2 \longleftrightarrow -3/2$, $-3/2 \longleftrightarrow -5/2$. The two close maxima corresponding to transitions $-3/2 \longleftrightarrow -1/2$ and $3/2 \longleftrightarrow 1/2$ are near the field $H \approx 1$ kOe. The maxima on the high-field part of curve 2 permit one to estimate the parameter of the zero splitting $D = D_0 = 0.09$ см$^{-1}$ $D < h\nu$).

7. It should be noted that the three states of the Fe^{3+} magnetic ion are observed experimentally. In the first low-symmetry state, the parameter of spin Hamiltonian $D >> h\nu = 0.3$ см$^{-1}$. The presence of line 1 testifies to the existence of such a state. $D_0 \approx 0.09$ см$^{-1}$ is characteristic of the second state. It is characterized by the form of line 2 at T=4.2K ($D = D_0 < h\nu$). The third state is highly symmetric and it is defined by the spin Hamiltonian parameter $D << D_0 < h\nu$. The form of line 2 at

T=288K corresponds to this state.

The change in the form of line 2 with the temperature increase is not connected with the temperature dependence of the parameter of zero splitting D. Let us discuss this assertion. In the case of decrease in D, the width of line 2 should decrease with the rise of temperature. That is what we observe experimentally (Fig.6.3). However, in such a case, the maxima of transitions -1/2 $\longleftrightarrow$ -3/2, -3/2 $\longleftrightarrow$ -5/2 should displace to the central transition 1/2 $\longleftrightarrow$ -1/2 with the increase of temperature. In fact, the temperature increase results in a decrease of the intensity of contribution of the state with $D=D_0 \approx 0.09$ cm^{-1} in the absence of the displacement of corresponding maxima.

8. According to the temperature dependence of the EPR spectrum obtained in this paper, in kaolin the Fe^{3+} ions are distributed over states having different values of the low-symmetry component of the crystalline field. At low temperatures, the states with the low-symmetry component possessing much more than the Zeeman energy are mainly occupied. When the temperature is increased, the excited states with the low-symmetry component much less than the Zeeman energy are occupied. Since the total number of magnetic ions is constant, the transition of ions to the excited states results in the decrease of the

intensity of line 1 as the temperature is increased. Line 2 becomes more intense in this case (Fig.6.5).

We thus pay attention to the following three characteristics. First, the low-temperature states are characterized by the low-symmetry properties; while the excited states are typical of the properties of much higher symmetry. Secondly, a region exists in which the low- and high-symmetry spectra coexist. Third, a decrease of the intensity of the low-symmetry spectrum when the temperature is increased, and a corresponding increase of the intensity of the high-symmetry spectrum are observed. Such characteristics are inherent to the systems with the multiminimum potential. The best studied system with the multiminimum potential is the Jahn-Teller ion of a divalent copper ion in an octahedral environment. In such systems, the temperature-induced changes in the intensity of spectra, which correspond to the low- and high-symmetric states, are due to changes in the population of vibronic states [6, 7]. It should be noted that Fe^{3+} is an S-ion, and the appearance of the Jahn-Teller effect for this ion is hardly probable. In the present case, the ion plays the role of a paramagnetic probe enabling one to observe the unusual dynamics of the ligand environment. The coincidence of the temperature changes of the EPR spectrum of Fe^{3+} in

kaolin with similar temperature changes in systems with the multiminimum potential provides grounds to propose that the magnetic center under consideration possesses similar properties. In systems with multiminimum potentials, parameter E_0 (1) characterizes the height of barrier between the minima.

§4. Magnetic probe Fe^{3+} in nanocomposites of ultrahigh-molecular weight polyethylene with montmorillonite crystals.

4.1. Montmorillonite structure.

Montmorillonite and kaolinite structures refer to one and the same subclass of silicates. Their crystal structures are therefore very similar. But in montmorillonite and kaolinite structures the unit cell parameters and symmetry differ very much. The Montmorillonite chemical formula is $M_x(Al_{4-x}Mg_x)Si_8O_{20}(OH)_4$ (M = monovalent cation; x=degree of isomorphous substitution). The montmorillonite space group is monocline symmetry C_{2h}^3 – C2/m with the unit cell parameters $a_0 = 5.17Å$; $b_0 = 8.97Å$; $c_0 = 9.95Å$; $\beta = 99^0 54'$; Z=2. The iron content of montmorillonite is around 1 % and depends on the deposit of origin. The nearby environment of Fe^{3+} ions is in the form of octahedrons of two types. The magnetic Fe^{3+} ion substitutes the Al^{3+} ion isovalently. The

magnetic Fe^{3+} ion can be in two nonequivalent positions.

4.2. Experimental results.

An X-band radiospectrometer was used for the investigation of EPR spectra in microwave fields. The used radiospectrometer has a rectangular resonator with the size of one wavelength. The investigated sample is placed in the maximum of resonator magnetic field. The electrical field value is minimal in this case. With measuring vial of a small diameter the electrical field is close to zero.

Dependence of E and H values on distance can be determined by the equations:

For E-wave:

$$E_z = E_0 \sin(m\pi/a) x \sin(n\pi/b) y e^{jwt-\gamma z}$$

For H-wave:

$$H_z = H_0 \cos(m\pi/a) x \cos(n\pi/b) y e^{jwt-\gamma z}$$

Where m and n are integers, a and b - sides of resonator section.

By using the differential relations between x- and y-components of the electromagnetic field, that are taken from the above equations, we can find values of E_x, E_y and H_x, H_y for the waves of two types. It should be noted that in the resonator the maxima of the magnetic and electrical field are shifted by a quarter of the wavelength.

The EPR spectrum was investigated by using a spectrometer with the

microwave field frequency $\nu = 9.756 \pm 0.001$ GHz at T=77-450K. Primary attention was paid to the spectrum of the impurity Fe^{3+} ion. The form of the EPR spectrum is shown in Fig.4. The spectrum of the impurity Fe^{3+} ion consists of two resonance lines. Line 1 is anisotropic, it is described by the effective g-factor $g_1 = 4.13 \pm 0.16$. Resonance line 2 is described by the effective g-factor $g_2 = 2.15 \pm 0.1$. It is seen that when the temperature is increased, the intensity of resonance line 1 decreases, whereas line 2 becomes more intense. Investigation of Fe^{3+} EPR spectrum in montmorillonite single crystals demonstrated that the development of multi-minimum potential effect at high temperatures is expressed in the resolution of the EPR spectrum for both lines at T = 77-300K. Therefore, there is no need in liquid helium for the experiments. During the experiment, the value of x was set by the diameter of test tubes used. The test tubes were of two diameters. Tube 1 was of a smaller diameter. Hence, the electrical field value was lower. The EPR spectrum of Fe ions in montmorillonite crystals is shown in Fig. 6.8. Thick line denotes the EPR spectra for T=77K and T=295K measured in the test tube of smaller diameter. Thin line denotes spectra for T=115, 150, 200, 300 and 450K measured in the test tube of larger diameter. EPR spectra of Fe^{3+} ions in montmorillonite crystals in different test tubes are shown in Fig.6.9. In Fig.6.9, the temperatures are minimal for

the conducted experiments. One can see the difference in the shape and width of the line for different test tubes. Consequently, for these tubes the value of the electrical microwave field is also different. By this difference one can determine the value of the magnetic dipole moment.

4.3. Discussion. Non-centrality in the position of Fe^{3+} ions in the electric field.

In a number of organic and inorganic substances it has been experimentally found that Fe^{3+} magnetic centers show the properties typical of the centers with multiminimum potential. The existence of multiple minima is defined by a noncentral position of the magnetic ion. And the noncentral position of the magnetic ion results in the existence of the dipole moment. The dipole moment of the magnetic center and the low-symmetry component of the crystalline field are due to the spontaneous deformation of the environment, so they are interrelated. This characteristic property of the magnetic center may be displayed in optical and magnetic properties of the substances having such magnetic centers. Magnetic substances with Fe^{3+} ions are widely utilized, so it is important to study this newly-found characteristic property. Besides, the investigation of properties of the magnetic center with the multiminimum potential is, by itself, of high scientific importance. The reason is that such magnetic centers show unusual properties and have

not been studied enough.

In multiminimum potential wells, the dynamics is observed in peculiarities of the temperature dependence of physical properties. It depends on the height of barrier separating different wells on potential surface. Barrier height is an important parameter that determines many physical properties of magnetic centers with the multiminimum potential. To determine barrier height, the temperature dependence of the integral intensity of EPR spectrum resonance lines should be investigated.

The dipole moment present with magnetic centers may, on the one hand, be exhibited in the physical properties of substances. It also opens new possibilities for the investigation of such substances. A magnetic center possessing both the magnetic moment and electrical dipole moment can interact with the magnetic field and electrical field. Interaction with the magnetic field enables one to use the standard EPR method which is high-sensitive and informative. The electrical dipole moment widens the potentialities of investigations by using the EPR method.

§5. Conclusions.

Within the framework of the proposed model of the excited-state

population, it is possible to explain the character of the temperature dependence of the integral intensity of the EPR spectrum resonance lines, the width of resonance for line 2, and the rest of the features of the EPR spectrum.

At helium temperature, the ligands of the environment are "frozen" at the bottom of the potential well (or wells) which correspond to the largest value of the low-symmetry component of the crystalline field. Simultaneously, the anisotropy of the crystalline electrical field is maximum, and therefore line 1 is the most intense. As the temperature is increased, a number of magnetic centers pass to the excited vibronic states. The excited states of magnetic centers are less anisotropic than the ground states. In the case of the Jahn-Teller ion of copper, this property is connected with the averaging of deformation as a result of fast "hops" from one potential well to another. The resonance line 2 of the EPR spectrum results from the population of weakly anisotropic excited states (Fig.6.3). Increasing the number of magnetic centers in the excited states leads to a decrease of the number of magnetic centers in the ground state. It is the cause of the increase of the intensity of resonance line 1 when the temperature is raised.

The unusual temperature dependence of the width of resonance

line 2 (Fig.6.6) is due to the change in distribution of magnetic centers over the excited states.

At high temperatures, the greater part of the magnetic centers is found in the excited states for which $D << D_0 < h\nu$. The EPR spectrum of these centers is characterized by the g value of the transition $1/2 \longleftrightarrow -1/2$. The orientational averaging of the rest of transitions does not broaden the resonance line.

At low temperatures, a major portion of the magnetic centers is in states close to the ground state. The lower the excitation energy, the higher the value of the low-symmetry component of the crystalline field and the farther the resonance lines of transitions $\pm 5/2 \longleftrightarrow \pm 3/2$ are located from the line of the transition $1/2 \longleftrightarrow -1/2$. As a result of the orientational averaging over directions of the axes of symmetry, the contribution of the transitions $\pm 5/2 \longleftrightarrow \pm 3/2$ and $\pm 3/2 \longleftrightarrow \pm 1/2$ at low temperatures will result in the broadening of resonance line 2 (Fig. 6.3, 6.6).

The temperature-induced change in the EPR spectrum of the Fe^{3+} complex in kaolin is similar to that of the Fe^{3+} ion in nitroso-β-naphtol and polyaniline [6.5]. This coincidence of the properties of the EPR spectra of the magnetic centers, despite the substantial difference in the

ligand environment of the Fe^{3+} ion, evidences the presence of an effect which is common to those different substances.

In this article, it is shown that the investigated magnetic ion plays the role of a magnetic probe. This magnetic probe is an essential part of kaolinite, and this fact can be used for investigating the magnetic properties of kaolinite-clay.

§6. References.

1. E. G. Howard, R. D. Lipscomb, R. N. MacDonald, B.L. Glazar, C. W. Tullock and J. W. Collete, Homogeneous Composites of Ultrahigh Molecular Weight Polyethylene and Minerals. 1.Synthesis, Ind. Eng. Chem. Product. Research and Development **20**, 421-428 (1981).

2. Y. T. Lim and O. Ok Park, Rheological evidence for the microstructure of intercalated polymer/layered silicate nanocomposites, Macromol. Rapid Commun. **21**, 231-235 (2000).

3. M. Alexandre and P.Dubois, Polymer – layered silicate nanocomposites: preparation, properties and uses of a new class of materials, Materials Science and Engineering **28,** 1-63 (2000).

4. V. A. Beloshenko, G. V. Kozlov, V. N. Varyuhin and V. G. Slobodina, Properties of ultra-high-molecular polyethylene and related polimerization-filled composites produced by solid-state extrusion, Acta Polimer **48,** 181-187 (1997).

5. V. N. Vasyukov, V. P. Dyakonov, V. A. Shapovalov, E. I. Aksimentyeva, H. Szymczak and S. Piechota, Temperature-induced change in the ESR spectrum of the Fe^{3+} ion in polyaniline, Low Temperature Physics **26**, 265-269 (2000).

6. V. N. Vasyukov, Dependence of the low temperature EPR spectrum of Cu^{2+} ion on the microwave field frequency and temperature, Physica status solidi (b) **137**, 623-631. (1986).

7. V. N. Vasyukov and B. Ya. Suharevskii, Energy spectrum of vibronic states of a Jahn-Teller ion, Low Temperature Physics **20** (8), 644-652 (1994).

8. A. V. Leontyeva, G. A. Marinin and A. Yu. Prohorov, Influence of intermoleculari interaction features on inelastic properties of crystalline methane, Zurn. Fiz. Himii **68,** 975-978 (1994) (in Russian).

9. G.B. Bokii, Kristallohimiya, pp. 255, "Nauka", Moskva (1971) (in

Russian).

10. V. N. Mank, F. D. Ovcharenko and L. S. Sonkin, Study of the state of iron in kaoline by the EPR method, DAN SSSR **233,** 675-678 (1977).

11. V. V. Mank, F. D. Ovcharenko, L. V. Golovko, N. G. Vasilyev and A. Ya. Karushkina, On nature of stable radicals in kaolin, DAN SSSR **223**, 389-392 (1975).

12. E. Burzo, M. Chipara, D. Ungur and I. Ardelean, Electron Paramagnetic Resonance Study of xFe_2O_3 (1-x)[B_2O_3 PbO] Glasses, Phys. Stat. Solidi (b) **124**, K117-K120 (1984).

13. R. Singh, Effect of Fe ions on electrical conductivity and ESR in tellurium-vanadate glasses, J. Phys.D: Appl. Phys **17**, L57-L60 (1984).

14. C. S. Sunandana and R. Jagannathan, ESR and Messbauer Studies of Fe^{3+} ion in calcium boro-aluminate glasses, Solid State Communications **53**, 985-988 (1985).

15. A. Montenero, M. Friggeri, D.C. Giori, N. Belkhiria and L.D. Pye, Iron-soda-silica glasses: preparation, properties, structure, J. Non-Crystalline Solids **84**, 45-60 (1986).

16. J. Komnsinski, L. Stoch and S.M. Dubiel, Application of Electron Paramagnetic Resonance and Mossbauer Spectroscopy in the Investigation of Kaolinite-group Minerals, Clays and Clay Miner. **29,** 23-30 (1981).

17. Ya. G. Klyava, EPR spectroscopy of disordered solids, pp. 320, "Zinatne", Riga (1988).

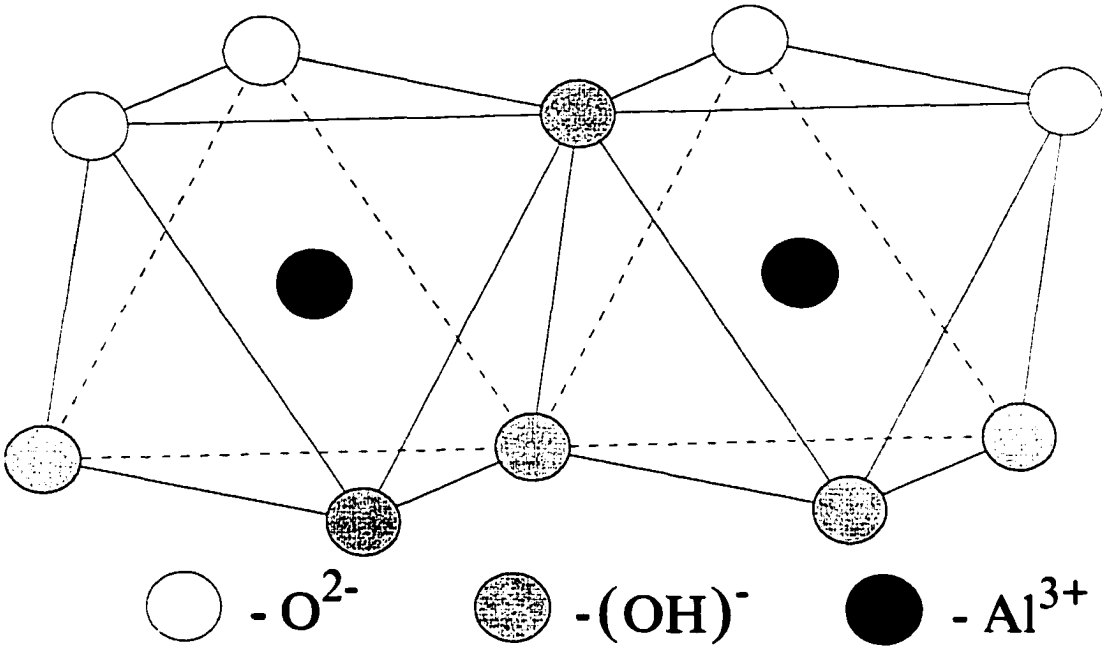

Figure 6.1. The nearby environment of Al^{3+} ions in structure of kaolinite $Al_2[Si_2O_5](OH)_4$. The magnetic Fe^{3+} ion substitutes the Al^{3+} ion isovalently. It is seen that the magnetic Fe^{3+} ion can be in two nonequivalent positions.

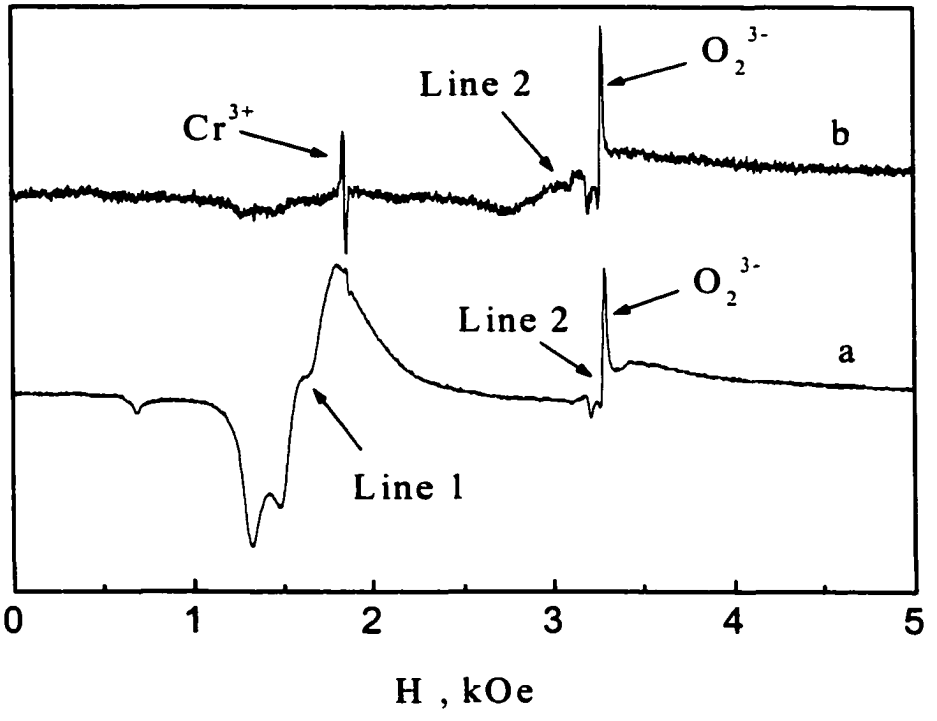

Figure 6.2. Fe^{3+} EPR spectrum in kaolinite: a) T=4.2K, b) T=288K. The narrow line (ΔH=I7 Oe) with the effective g-value g = 3.5 pertains to the Cr^{3+} ion which was used to calibrate the magnetic field. The narrow line with $g \approx 2$ corresponds to the O_2^{3-} ion existing on the cleavage plane of the mineral. Two broad lines 1 and 2 pertain to the Fe^{3+} ion, which is usually present in mineral kaolin as an impurity. A partial splitting of line 1 is apparently connected with the two nonequivalent positions of the magnetic ion.

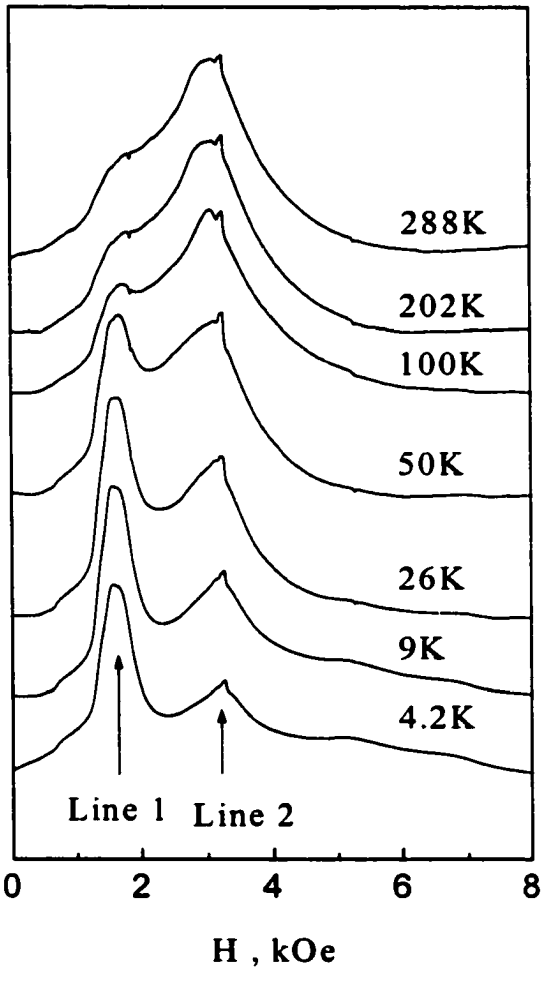

Figure 6.3. Temperature-induced change of the form of the EPR spectrum in kaolinite in the form of the absorption curve for the temperatures T = 4.2, 9, 26, 50, 100, 202 and 288 K. It is seen that when the temperature is increased, the intensity of resonance line 1 decreases, whereas line 2 becomes more intense. The g-values for the resonance lines do not depend strongly on temperature.

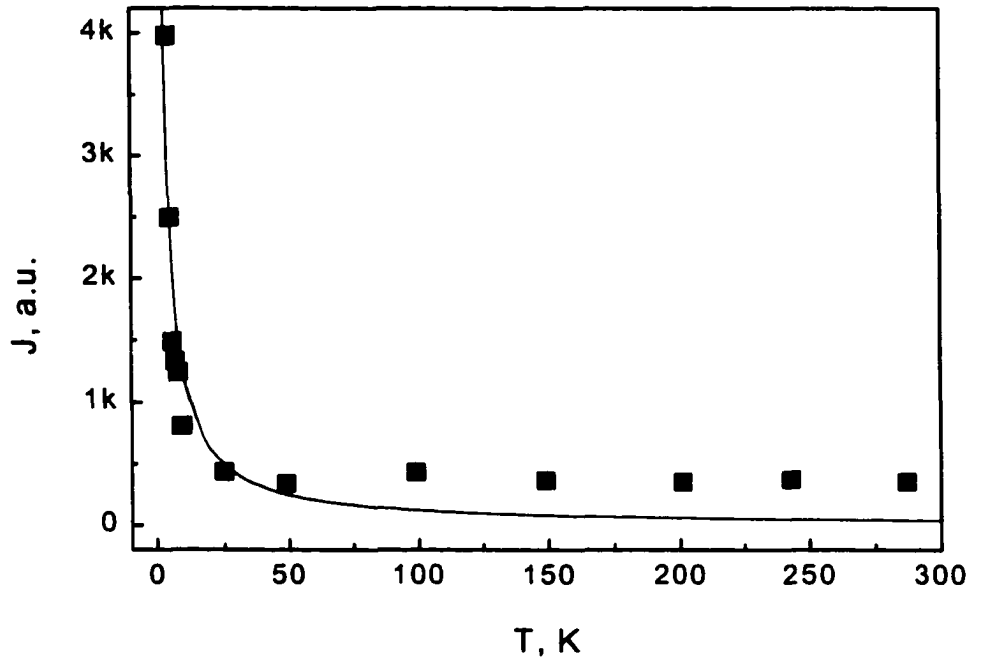

Figure 6.4. Temperature dependence of the total integral intensity of resonance lines 1 and 2 in the EPR spectrum of Fe^{3+} in kaolinite. This dependence describes the first mechanism of temperature change in the EPR spectrum. The first mechanism is determined by the temperature dependence of the difference of the population in the resonance states. The solid line describes the dependence $I(T) = I_0 \tanh(h\nu/2kT)$.

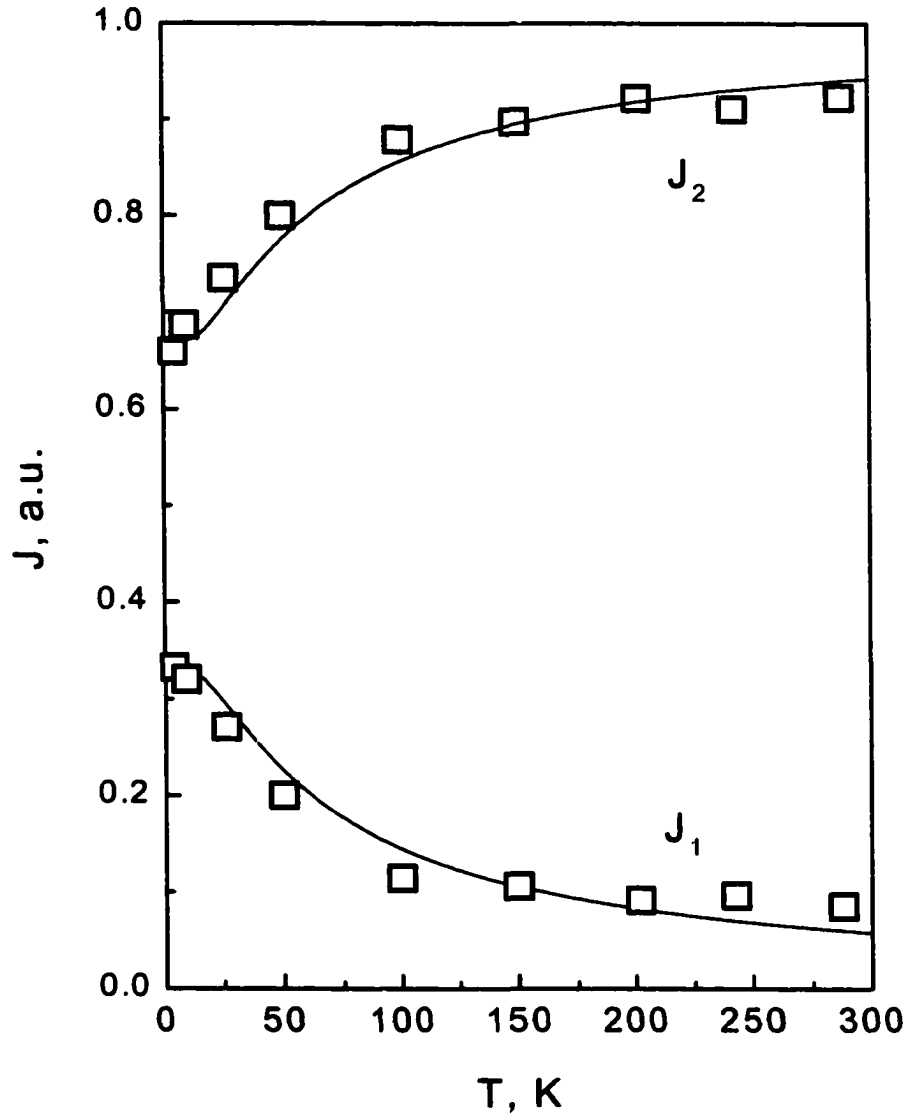

Figure 6.5. Temperature dependence of the relative integral intensities of lines 1 and 2. This dependence describes the second mechanism of temperature change in the EPR spectrum which describes the process of the integral intensity redistribution between lines 1 and 2.

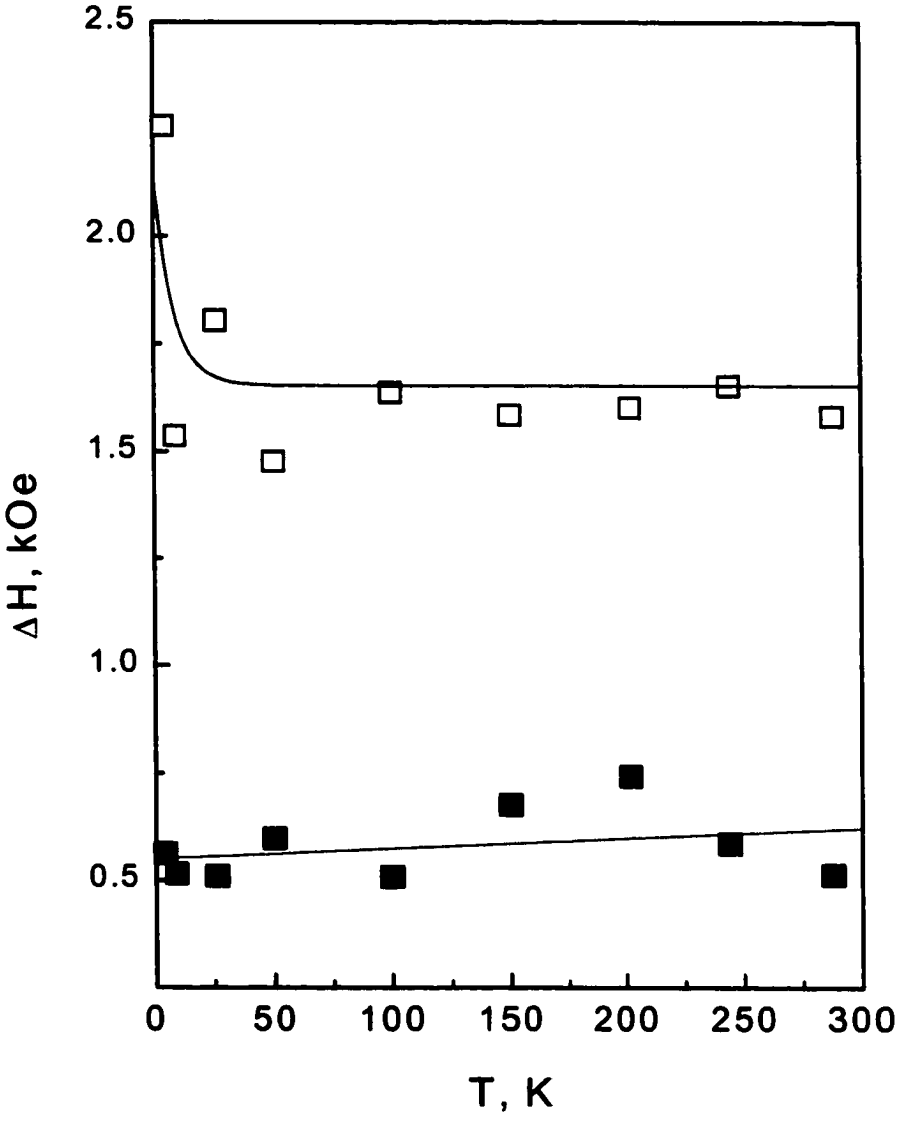

Figure 6.6. Temperature dependence of the width of resonance lines. The width of line 1, ΔH_1 does not depend on temperature. When the temperature is decreased, the width of line 2 grows exponentially.

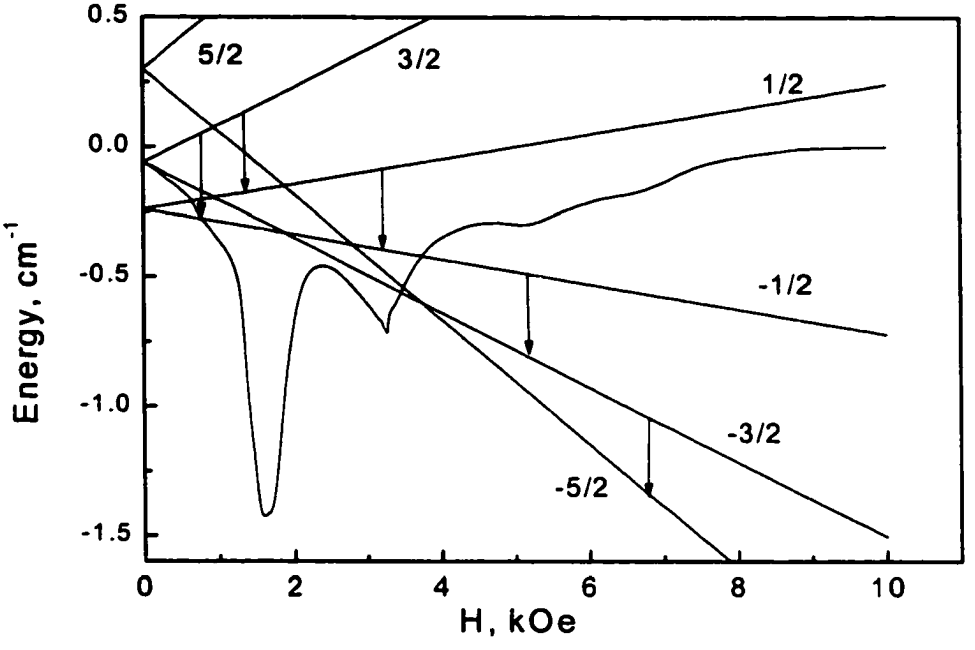

Figure 6.7. Structure of the energy states of the spin multiplet S=5/2 and a form of the EPR spectrum at T=4.2K. The resulting form of line 2 has 5 maxima. The central maximum corresponds to transition 1/2 ⟷ -1/2. The two high-field maxima correspond to transitions -1/2 ⟷ -3/2, -3/2 ⟷-5/2. The two close maxima corresponding to transitions -5/2 ⟷ -3/2 and 3/2 ⟷ 1/2 are near the field H ≈ 1kOe.

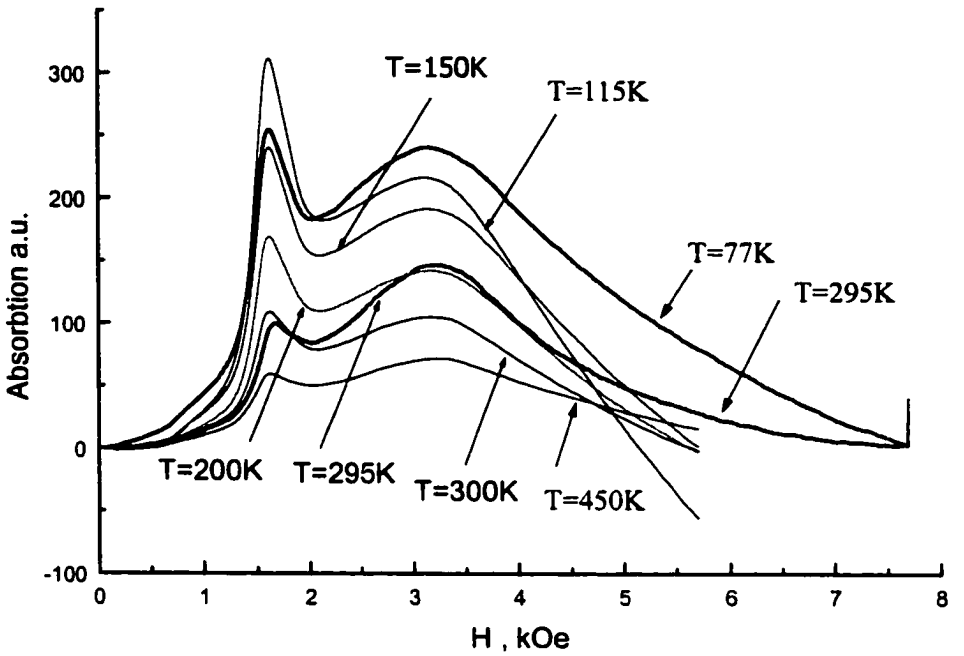

Figure 6.8. Fe^{3+} EPR spectrum in monmorillonite: T=77, 115, 150, 200, 295, 300 and T=450K.

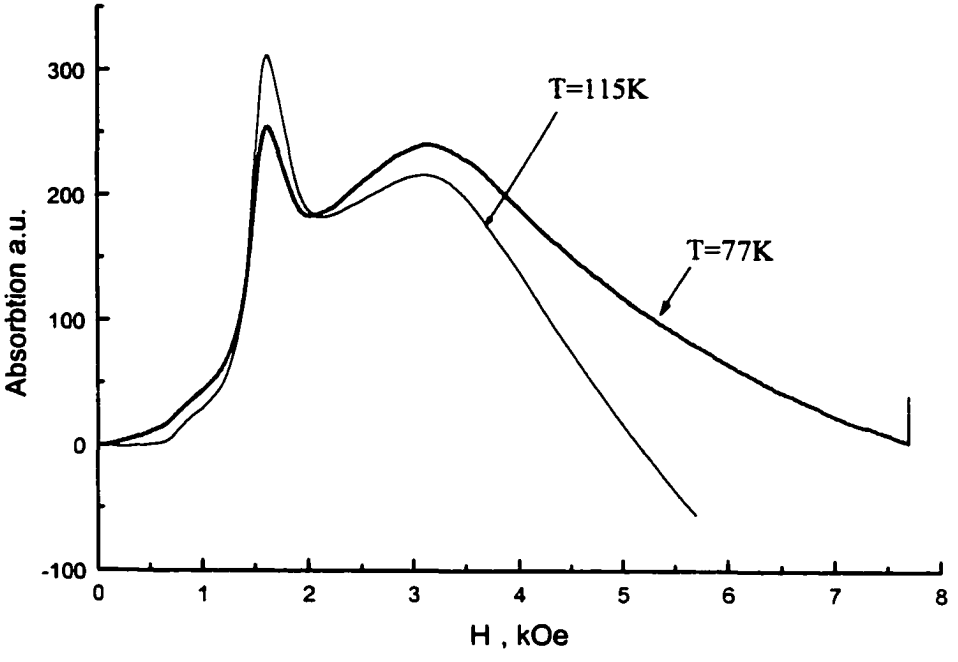

Figure 6.9. Noncentrality in position of Fe^{3+} ion in the electrical field. Fe^{3+} EPR spectrum in monmorillonite: T=77K and T=115K.

Chapter 7.

Plastic deformation-induced orientation of kaolinite crystals in ultrahigh-molecular polyethylene

§1. Introduction.

Kaolin is widely used for producing the filled polymeric systems [1-4]. Kaolin additions reduce the relative fraction of polymer in final product, thus reducing the cost of articles and enabling one to create materials with a new complex of properties. Some of the properties depend on the relative orientation of kaolinite crystals which are in the form of thin plates [5].The problem of investigating the location of kaolinite crystals in polymer matrix seems rather urgent. It was the subject of articles [1-3]. One of the prospective methods of producing the polymer materials with a preset orientation of filler crystals is the solid-phase extrusion [4] under which the orientational drawing is realized under high hydrostatic pressure. Articles [6-10] were the first which dealt with the investigation of high-pressure effect on polymers. Principal regularities in the behavior of polymer materials during the deformation under high pressures are set forth in articles [11-15].

This article is aimed at studying the orientation of kaolinite crystal

plates in ultrahigh-molecular polyethylene (UHMPE) induced by solid-phase extrusion by means of the X-ray diffraction and EPR spectroscopy methods.

§2. Method of sample preparation.

Polymeric composite material based on UHMPE with the 27% content of kaolin-clay is investigated in this article. The initial powder material was prepared by means of polymerization filling [16]. In this case, monomer polymerization occurs on the surface of filler (kaolinite). As a result, kaolinite single crystals are covered with a polymer layer of controllable thickness. The uniformity in polymer distribution on kaolinite surface provides the uniform distribution of filler in polymeric matrix.

The investigation samples were produced by the plunger extrusion method using a setup mounted on the basis of a 100-ton vertical hydraulic press. The setup included a deforming die located in the bottom of container bore. The plunger velocity was 2 mm/s. Billets for the extrusion were produced by compacting the powder in a mould.

Next, the billets were loaded in the high-pressure container. Prior to the extrusion, the container with billet and the die were heated to

T=393K that corresponded to $0.9T_m$, where T_m is the temperature of ultrahigh-molecular polyethylene melting. The temperature of extrusion was fitted empirically proceeding from the fact that qualitative specimens could not be produced at a lower or a higher temperature.

The extrusion ratio is the ratio between cross-section areas of the billet (container bore) and die opening found by the relation $\lambda = d^2_b / d^2_d$. Specimens with λ=7 were investigated.

§3. Kaolinite structure.

According to [5], the crystalline structure of kaolinite $Al_2[Si_2O_5]\cdot(OH)_4$ consists of two-layer packets with one tetrahedral silicon-oxygen layer of composition $[Si_{2n}O_{5n}]^{2n-}$ and one octahedral alumo-oxygen-hydroxylic layer of composition $[Al_{2n}(OH)_{4n}]^{2n+}$ (Fig. 7.1). The both layers form a packet by means of common oxygen atoms from the silicon-oxygen layer. Kaolinite space group is $C_i^1(P\bar{1})$. Unit cell parameters are: a = 5.14; b = 8.93; c = 7.37 Å; $\alpha = 91.8°$; $\beta = 104.5°$.

In kaolinite, the paramagnetic impurity Fe^{3+} ions substitute the Al^{3+} ions isovalently. The iron content of kaolin varies usually from 0.3 to 1.1% depending on a deposit [17]. In Fig. 7.1 it is seen that the existence of two nonequivalent positions of the magnetic Fe^{3+} ion is

possible. In those positions the environment is represented by octahedra of two types with two oxygen atoms and four OH-groups.

§4. Experimental results. The X-ray diffraction analysis.

The X-ray diffraction analysis of the kaolinite-plate orientation in extruded specimens was done at T=295K. A spectrograph was used to investigate the diffuse scattering of the low-intensity X-rays in a wide range of the X-ray scattering angles ($\theta = 5^0 \div 80^0$) with a high resolution of diffraction maxima that was provided by application of the Debye method and the use of a soft CrK_α-radiation, $\lambda = 2.29092$ Å.

The X-ray diffraction patterns of Fig. 7.2 corresponds to powder sample with the maximally disordered kaolinite plates. Fig. 7.3 shows the X-ray from the lateral surface of the extrudate and Fig. 7.4 –from its face.

The X-ray diffraction patterns are characteristic of the presence of two regions differing in the values of intensities and the width of Debye lines. The first region makes an interval of angles $\Delta\theta_1 = 9 \div 20^0$. Here the lines are more intensive as compared to those of the second region. The second region makes an interval of angles $\Delta\theta_2 = 20 \div 80^0$. For the X-ray diffraction patterns of Figs(7.2, 7.3, 7.4) the comparison of the

intensities and widths of Debye lines in the two regions shows that:

1. In the case of powder specimen the Debye lines are wide. They are low-resolved for all diffraction angles. For the first region the maximum intensity of lines is $J_{max} = J_{0(1)} \approx 35$ a.u. That of the second region is $J_{max} = J_{0(2)} \approx 8$ a.u.

2. The X-ray diffraction patterns from the first region correspond to the lateral surface of the extruded specimen, they are the most narrow and intensive (Fig. 7.3), $J_{max} = J_{||(1)} \approx 70$ a.u. In the second region $J_{max} = J_{||(2)} \approx 6$ a.u. Width of the most intensive lines of 001 and $1\bar{1}0$ from the corresponding basal planes makes 0.45^0.

3. For extrudate face (Fig. 7.4) the diffraction lines in the first region are less intensive than those from the lateral surface (($J_{max} = J_{\perp(1)} \approx 35$ a.u.). In the second region the lines are more intensive ($J_{max} = J_{\perp(2)} \approx 15$ a.u.).

Also, it should be noted that in all the investigated cases the second regions are different. Near $\theta \approx 70^0$ the X-ray diffraction patterns for both the powder and the extrudate (Figs 7.2, 7.4) has a maximum which is the sum of diffraction lines of kaolinite plates with high indices hkl and diffuse incoherent scattering. And also, in the case of complete

misorientation (powder) the value of this maximum is less than that of the extrudate (face) since the deformation-induced displacements of structure elements result in the increase in the intensity of incoherent large-angle θ scattering (background).

In the second region of angles, there is no such a broad maximum for the lateral surface (Fig. 7.3). Thus, in the lateral surface layer the structure is more ordered than in the face layer. Also, the results indicate that in the lateral surface layer of the extrudate there has been a reorientation in the set of planes: $(1\bar{1}\bar{1})\rightarrow(1\bar{1}0)$.

One should pay attention to indices of lines from planes giving reflections in the region of small angles ($\theta < 20^0$), see Fig. 7.3. In case of diffraction from the initial powder the maximum intensity is for the diagonal planes of the $(1\bar{1}\bar{1})$ type. For the basal planes of the (001) type the intensity is three times as less (Fig. 7.2). A similar pattern but with a more narrow lines (Fig. 7.4) is observed for extrudate face. On the diffraction pattern from the lateral surface layer of the extrudate the $1\bar{1}\bar{1}$ line (the insert of Fig. 7.3) is very faint. At the same time, the most intensive are reflections from the basal planes of (001) and $(1\bar{1}0)$ which are, respectively, parallel and normal to the (**ab**)-plane, Fig. 7.1.

From the obtained results it can be concluded that:

1. The solid-phase extrusion of the composite material has resulted in the appearance of volume anisotropy in kaolinite. This is evidenced by differences in the intensities of Debye lines $J_{||}$ from the lateral surface layer of the extruded specimen and $J_{\perp}$ from the face surface layer. In the first region of angles $J_{||(1)} / J_{\perp(1)} = 2$. In the second region of angles $J_{||(2)}/J_{\perp(2)} = 0.4$.

2. There is a preferable turn of kaolinite planes of low hkl indices along cylinder axis. This is proved by a higher value of $J_{||}/J_{\perp}$ ratio for the first region of angles as compared to that for the second region. For the first region $J_{||(1)}/J_{0(1)} = 2$ and for the second one $J_{||(2)}/J_{0(2)} = 0.75$.

After the extrusion the $(1\bar{1}0)$ and (001) planes of kaolinite plates take the preferential direction which is parallel to cylindrical specimen axis. This is evidenced by the maximum value of the intensities of lines from the $(1\bar{1}0)$ and (001) planes.

§5. Experimental results. Investigation of the EPR spectrum.

The EPR spectrum was investigated by using an spectrometer with the microwave field frequency $\nu = 9.247 \pm 0.001$ GHz at T=4.2 K. Under investigation, the main attention was attracted to studying the spectrum

pertaining to the impurity Fe^{3+} ion, a component of kaolinite mineral.

EPR spectrum form is shown in Fig. 7.5. Spectrum of the impurity Fe^{3+} ion consists of two resonance lines. Line 1 at T= 4.2K is anisotropic, it is described by the effective g-factor $g_1 = 4.13 \pm 0.16$. Resonance line 2 is described by the effective g-factor $g_2 = 2.15 \pm 0.1$. At T=4.2 K it has the width $\Delta H_{2pp} = 0.36$ kOe.

In the EPR spectrum there are, apart from the resonance lines pertaining to the impurity Fe^{3+} ion, more narrow ($\Delta H \approx 17$Oe) resonance lines of the Cr^{3+} ion and O_2^- ion. The Cr^{3+} EPR spectrum was used for magnetic field calibration. (Cr^{3+}- ions are not kaolinite components). According to [17], O_2^- ions are located on cleavage planes of the mineral. O_2^- EPR spectrum is in the form of narrow line described by g-factor equal to 2.

Dependence of the EPR spectrum on magnetic-field orientation has been investigated in two planes, that is normal to extrudate axis and parallel to the same. In the first case, the dependence of the EPR spectrum on magnetic field orientation was not found. In the second case, the dependence is that of the resonance field of line 1 on the angle of rotation (Fig. 7.6).

The angular dependence of Fig. 7.6 contains the two groups of

conjugate maxima. The maxima A1 and A2 shifted by 180^0 relatively each other pertain to the first group. The maxima B1 and B2, which are 180^0-shifted too pertain to the second group. Those conjugate maxima of the angular dependence of the resonance field define the directions along which the axes of Fe^{3+} magnetic centers are preferably oriented.

It should be noted that the axes of symmetry of the magnetic centers corresponding to the maxima (A1, A2) and (B1, B2) are turned by angles other than 90^0. Angles between the axes make 96^0 and 84^0. This is because of peculiarities in orientation of kaolinite plates in the extruded specimen. The observed angular dependence of Fe^{3+} EPR spectrum shown in Fig. 7.6 needs additional discussion, and this is done in Section 6.

§6. Discussion of the results.

The Fe^{3+} ion has a configuration $3d^5$. Spin of the ground state S=5/2. The most frequently met Fe^{3+} EPR spectra are typical of g-factor value close to $g \cong 2$.

The observed EPR spectrum has, on the one hand, features typical of a powder or an amorphous substance. On the other hand, the angular dependence indicates that in the extruded specimen the axes of

symmetry of the magnetic centers are to a considerable degree oriented along the specific directions. From this viewpoint, the obtained EPR spectrum should be considered as partially averaged with respect to directions of the magnetic center axes of symmetry.

In article [18] a detailed review is given of the results of EPR spectra investigation for the ions of iron in substances with the misoriented directions of the axes of symmetry of magnetic centers. It is assumed that the spectrum consisting of two resonance lines with $g \cong 2$ and $g \cong 4.3$ pertains to different nonequivalent magnetic centers of Fe^{3+} ion. The difference is in values of the low-symmetry component of the crystal field affecting the magnetic ion. The authors [18] of the above-mentioned article believe that the line with $g \cong 2$ corresponds to the center with the low-symmetry component of the crystal field much less than the Zeeman energy. Line with $g \cong 4.3$ corresponds to the center with the low-symmetry component of the crystal field much larger than the Zeeman energy.

In kaolinite there are two nonequivalent positions of the magnetic ion (Fig. 7.1). On the other hand, in mineral kaolin the magnetic centers may be accidentally deformed. In the totality of magnetic centers, one part may be deformed weakly, so that for those centers parameter of the

zero splitting D will be smaller than microwave field quantum ($D<h\nu$). Such magnetic centers will contribute to the resonance line 2. The rest magnetic centers contribute to the formation of line 1. Apart from the above mechanisms of formation of the two resonance lines in Fe^{3+} EPR spectrum, a third mechanism should be realized. It is defined by peculiarities of dynamic deformations of magnetic-ion crystalline environment. The mechanism is described in article [19] in more detail.

The spin Hamiltonian of the magnetic ion is represented as

$$H_0 = g_0 \cdot \beta \cdot \mathbf{H} \cdot \mathbf{S} + D \cdot (S_z^2 - S(S+1)/3) + E \cdot (S_x^2 - S_y^2) \qquad (1)$$

where β - is the Borh magneton, g_0 is the g-factor of ground multiplet S=5/2. The value of g_0 is close to 2.0; S_x, S_y, S_z- are spin-operator components; D, E are parameters of the zero splitting. D characterizes the field of axial symmetry. E characterizes the rhombic component of the field.

Value of the effective g-factor and the angular dependence of the EPR spectrum of the resonance line 1 of Fe^{3+} magnetic centers are described in article [18]. According to [18], the effective g-factor of the resonance line 1 is described by the relationship

$$g=\frac{30}{7}\left\{1+\frac{4}{7}q(\lambda_z^2-\lambda_y^2)+\frac{4}{49}(15q^2+4p^2)(\lambda_y^2+\lambda_z^2)-\frac{2}{49}(4q^2+5p^2)(\lambda_y^2-\lambda_z^2)-\right.$$
$$\left.-\frac{24}{343}(17q^2+4p^2)\right\} \qquad (2)$$

where $q=\frac{D-3E}{D+E}$, $p=\frac{g\mu_B H}{D+E}$, $\lambda_x=\sin\theta\cdot\cos\varphi$, $\lambda_y=\sin\theta\cdot\sin\varphi$, $\lambda_z=\cos\theta$.

Angles θ, φ assign the direction of external magnetic field in the spherical system of coordinates.

For the octahedral environment, the principal axis of symmetry of the magnetic center, as a rule, coincides with one of the fourth-order axes of the ligand octahedron. In Fig. 7.1, such magnetic axis is denoted by vector **m**. For the regular octahedron this angle makes 57° with respect to axis Z normal to the (**ab**)-plane which coincides with the most developed cut plane of kaolinite crystal. In the case of rhombic or a lower symmetry of the magnetic center, the magnetic axis of symmetry can deviate from the axis of distorted ligand octahedron by an angle larger than 10°. Angle α=0° of Fig.7.6 corresponds to direction of the external magnetic field along the axis of the extruded sample. According to the angular dependence of Fig. 7.6, the magnetic axis is directed at an angle of 48^0 to axis Z (Fig. 7.1). From the analysis of the experimental angular dependence shown in Fig. 7.6 and of the dependence for the

effective g-factor (2) it can be concluded that the Z-axis of each kaolinite plate is preferably oriented normal to extrudate axis. That is, the (**ab**)-planes of kaolinite plates are preferably oriented along the axis of the extruded specimen.

Fig. 7.7 schematically shows the arrangement of four kaolinite plates oriented along extrudate axis. In all the cases, the Z-axis is normal to cylinder axis. The upper portion of Fig. 7.7 illustrates the two plates. Their location differs in the orientation along axis a. The plates are displaced by an angle of 180° around the axis Z. Their magnetic axes are displaced with respect to cylinder axis through angles of 42° and 138°, respectively (Figs.7.6, 7.7). The plates contribute to the EPR spectrum and form the maxima A1 and B1 of the angular dependence (Fig. 7.6). In the same way, the two low-lying kaolinite plates contribute to the EPR spectrum and form the maxima A2 and B2 of the angular dependence.

Any other orientations of kaolinite plates associated with the displacement of axis **a** with respect to the Z-axis result in a partial averaging of the angular dependence, but do not change the directions of the maxima of the resulting angular dependence. In the plane orthogonal to extrudate axis, the Z-axis of different kaolinite plates may take

different orientations. The same as the a-axis, this will result in partial averaging of the angular dependence without changes in the directions of maxima of the resulting angular dependence.

By the X-ray diffraction investigations it was found that the (**ab**)-planes of kaolinite plates take a preferential direction which is parallel to the axis of the specimen. That is, the Z-axis turns out to be located along the face layer of the specimen, thus fitting the EPR data.

§7. Conclusion.

The obtained results allow us to conclude that the solid-phase extrusion results in the ordering of kaolinite plates in ultrahigh-molecular polyethylene. This is possible due to the availability of the developed cut plane in kaolinite crystal. The character of the kaolinite-plate orientation is defined by the direction of deformation gradient and its value.

§8. References.

1. E. G. Howard, R. D. Lipscomb, R.N. MacDonald, B. L. Glazar, C.W. Tullock and J.W. Collete, Homogenious Composites of Ultrahigh Moleqular Weight Polyethilene and Minerals.1.Synthesis, Ind. Eng. Chem. Product. Research and Development **20**, 421-428 (1981).

2. Y. T. Lim and O. Ok Park, Rheological evidence for the microstructure of intercalated polymer/layered silicate nanocomposites, Macromol. Rapid Commun. **21**, 231-235 (2000).

3. M. Alexandre and P.Dubois, Polymer – layered silicate nanocomposites: preparation, properties and uses of a new class of materials, Materials Science and Engineering **28,** 1-63 (2000).

4. V. A. Beloshenko, G. V. Kozlov, V. N. Varyuhin and V. G. Slobodina, Properties of ultra -high-molecular polyethylene and related polimerization-filled composites produced by solid-state extrusion, Acta Polimer **48,** 181-187 (1997).

5. V. A. Druts and A. A. Kashaev, X-ray diffraction investigation of kaolinite single crystal, Kristallographiya **5**, 224-227 (1960).

6. R. B. Dow, Inhibition of crystallization of rubber by high pressure, J. Chem. Phys. **7,** 201-206 (1939).

7. W. Parks and R. B. Richards, The effect of pressure on the volume thermodynamic properties and crystallinity of polyethylene, Trans. Faradey Soc. **45**, 203-211 (1949).

8. C. E. Weir, Compressibility of natural and synthetic high polymers at high pressure, J. Res. Natl. Bur. Stand. **46**, 207-212 (1951).

9. C. E. Weir, Transitions and phases of polytetrafluoroethylene, J. Res. Natl. Bur. Stand. **50**, 95-97 (1953).

10. P. W. Bridgman, The effect of pressure on the tensile properties of several metals and other materials, J. Appl. Phys. **24**, 560-570 (1953).

11. K. D. Pae and S. K. Bhateja, The effect of hydrostatic pressure on the mechanical behavior of polymers, J. Macromol. Sci. C **13**, 1-75 (1975).

12. S. K. Bhateja and K. D. Pae, The effect of hydrostatic pressure on the compressibility, crystallization and melting of polymers, J. Macromol. Sci. C **13**, 77-133 (1975).

13. K. Kishore and R. Vasanthakumari, A comprehensive review of the effect of pressure on polymer crystallization, High Temp. – High Pres. **16**, 241-268 (1984).

14. E. V. Prut, Application of high pressure in polymer processing, High – pressure Chemistry and Physics of Polymers (Ed. by A. L. Kovarskii), Bosa Raton: CRC Press, P.P. 341-346 (1994).

15. Ultra – high modulus polymers. Edited by A. Ciferri and I. M. Ward. Applied Science Publishers. London, P.P.271 (1979).

16. R. L. Adelman, E. G. Howard. Pat. 41511226, USA.

17. V. V. Mank, F. D. Ovcharenko, L. V. Golovko, N. G. Vasilyev and A. Ya. Karushkina, On nature of stable radicals in kaolin, DAN SSSR **223**, 389-392 (1975).

18. Ya. G. Klyava, EPR spectroscopy of disordered solids, "Zinatne", Riga, P.P. 320 (1988).

19. V. N. Vasyukov, V. P. Dyakonov, V. A. Shapovalov, E. I. Aksimentyeva, H. Szymczak and S. Piechota, Low Temperature Physics **26**, 265-269 (2000).

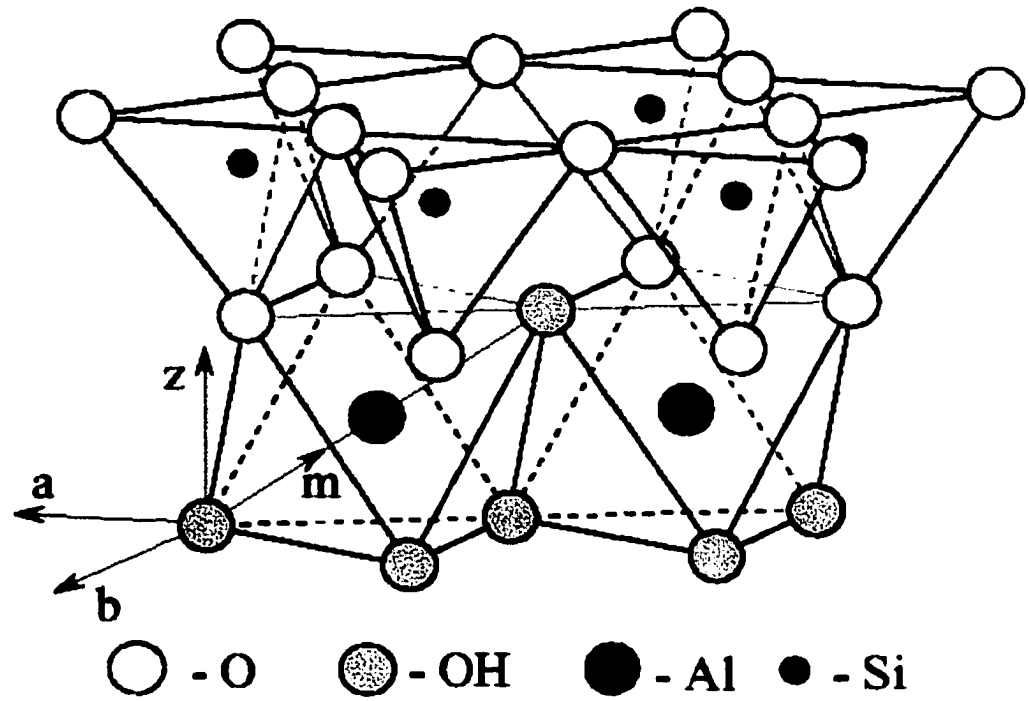

Figure 7.1. Structure of kaolinite $Al_2[Si_2O_5](OH)_4$: a, b – crystallographic axes; m – magnetic axis; Z – axis perpendicular to the (ab)-plane.

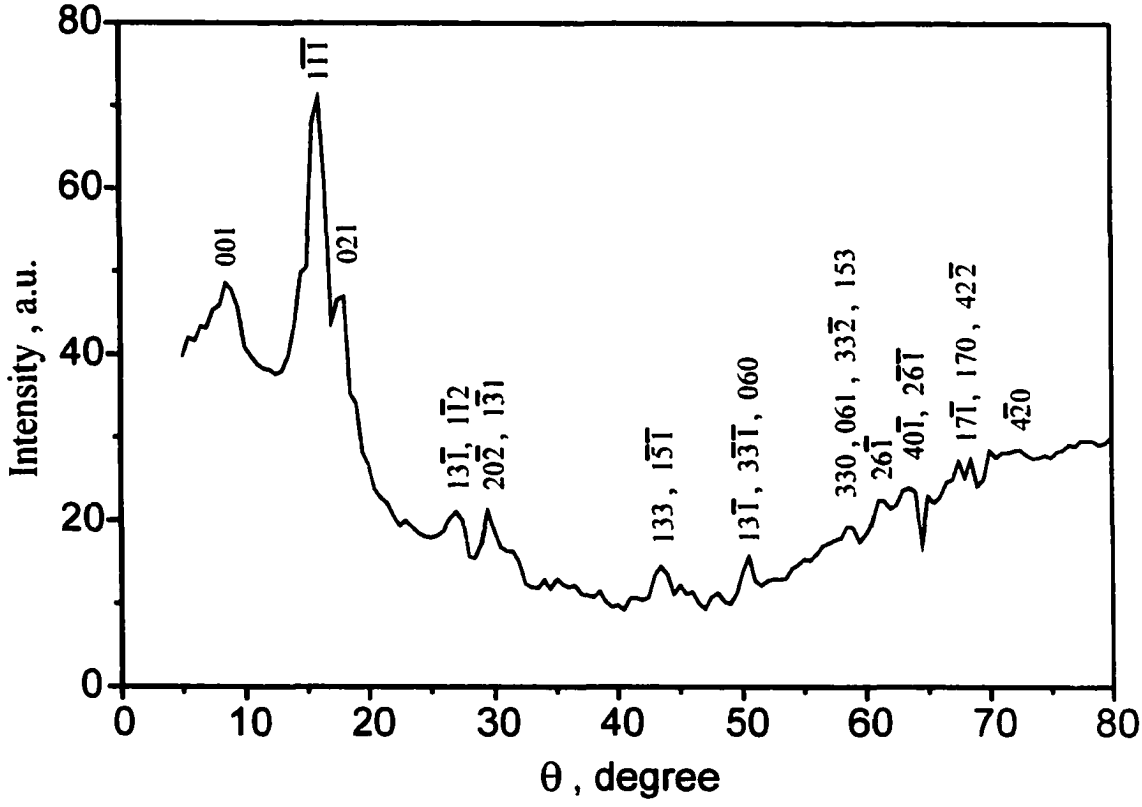

Figure 7.2. X-ray diffraction pattern of powder sample.

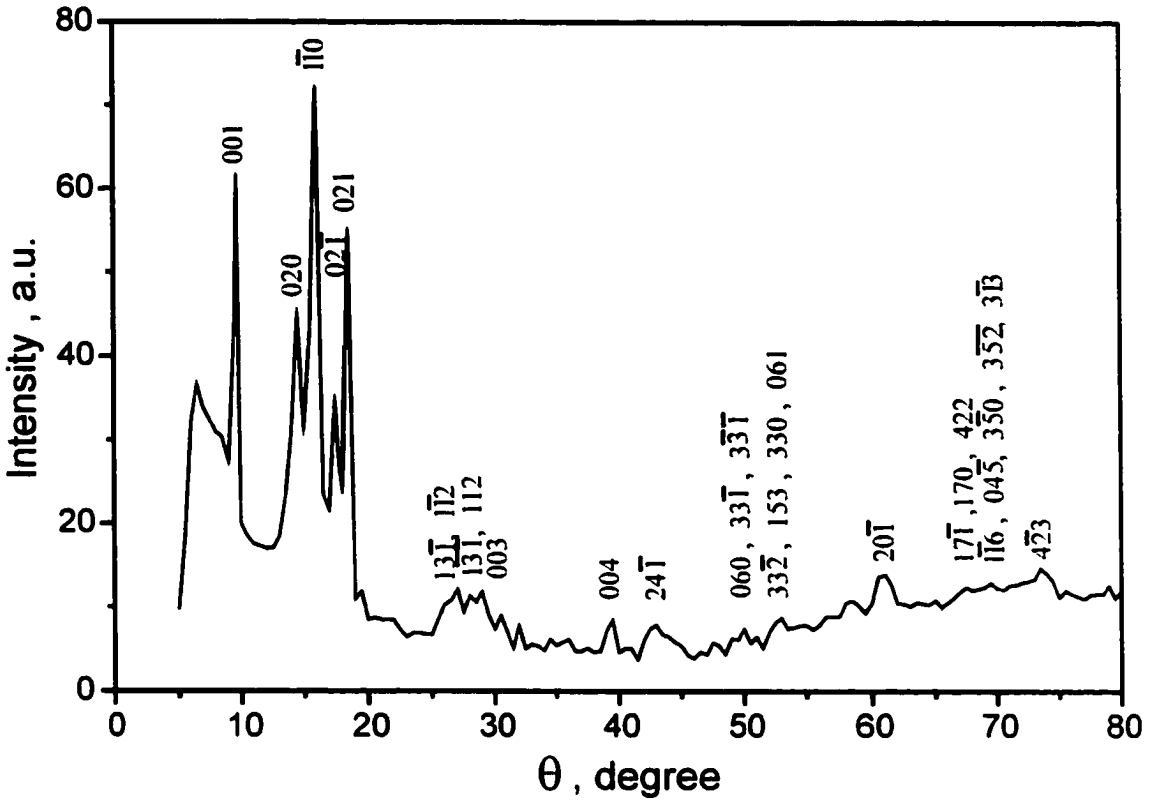

Figure 7.3. X-ray diffraction pattern of the lateral surface of the extrudated sample. In the insert - a portion of diffraction pattern at $\Delta\theta_1 = 9 \div 20^0$.

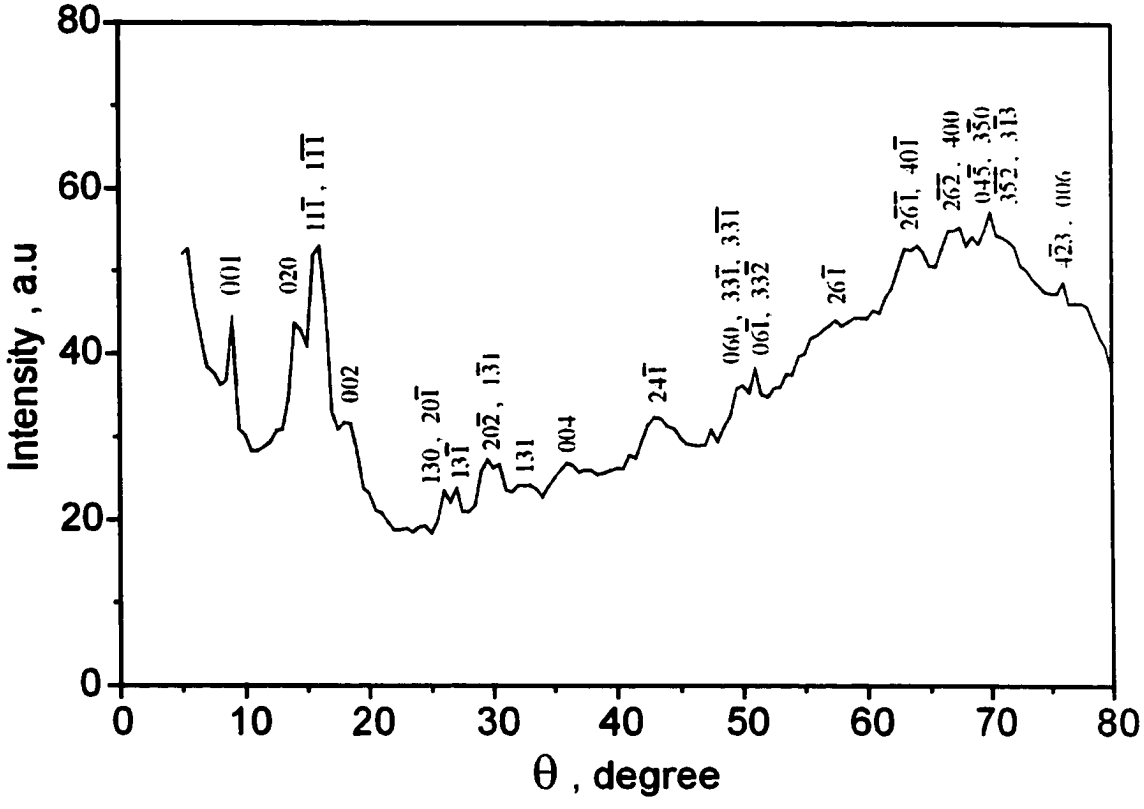

Figure 7.4. X-ray diffraction pattern of the face of extrudated sample.

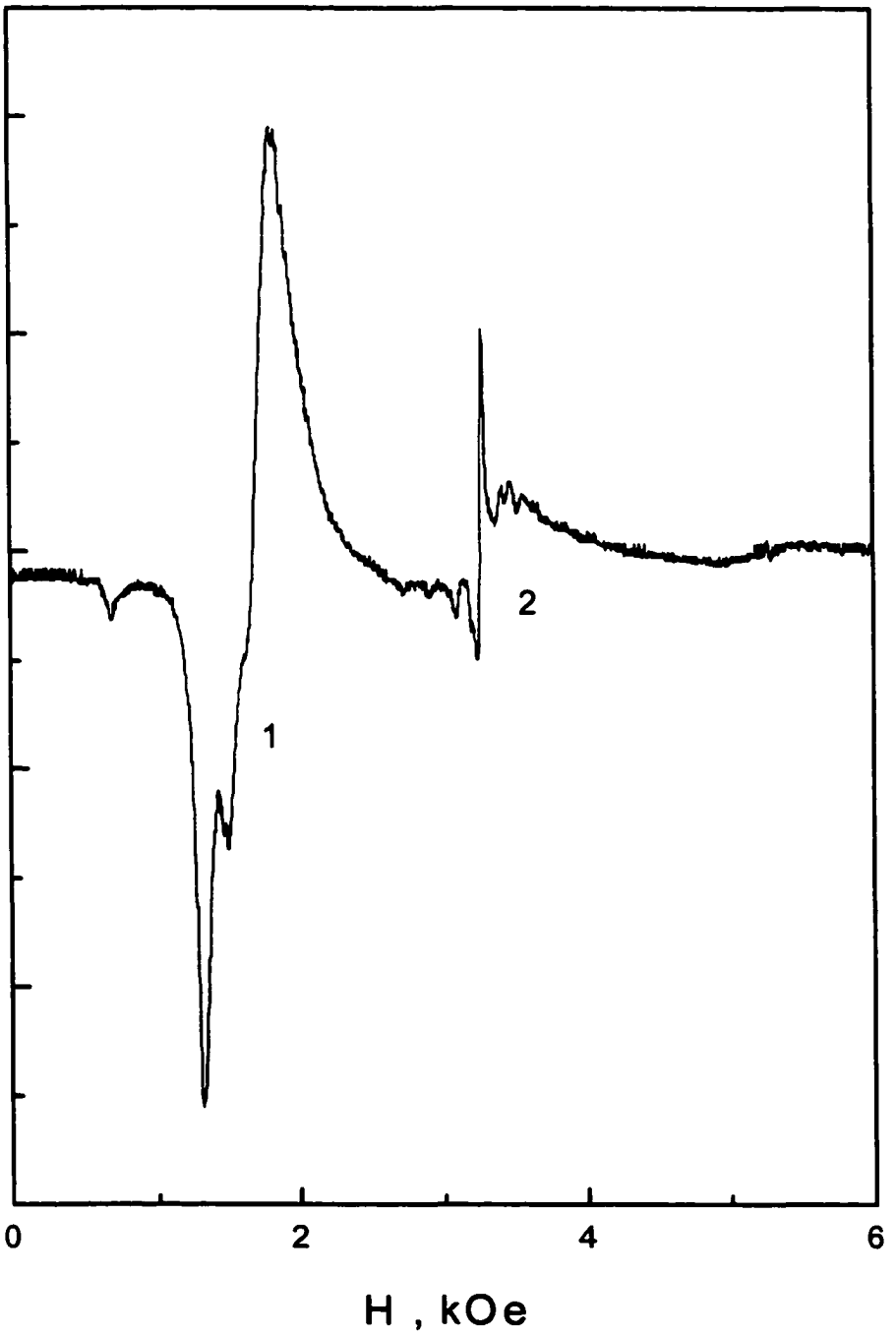

Figure 7.5. Fe^{3+} EPR spectrum in kaolinite: T=4.2K, H // Z.

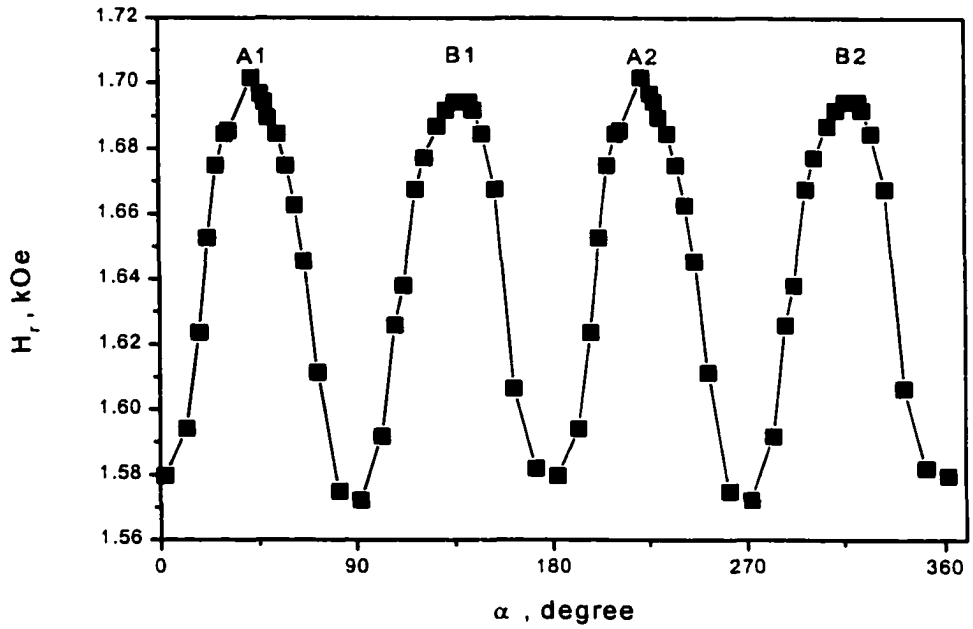

Figure 7.6. Angular dependence of the resonance field of line 1 at T=4.2K in the plane parallel to cylinder axis.

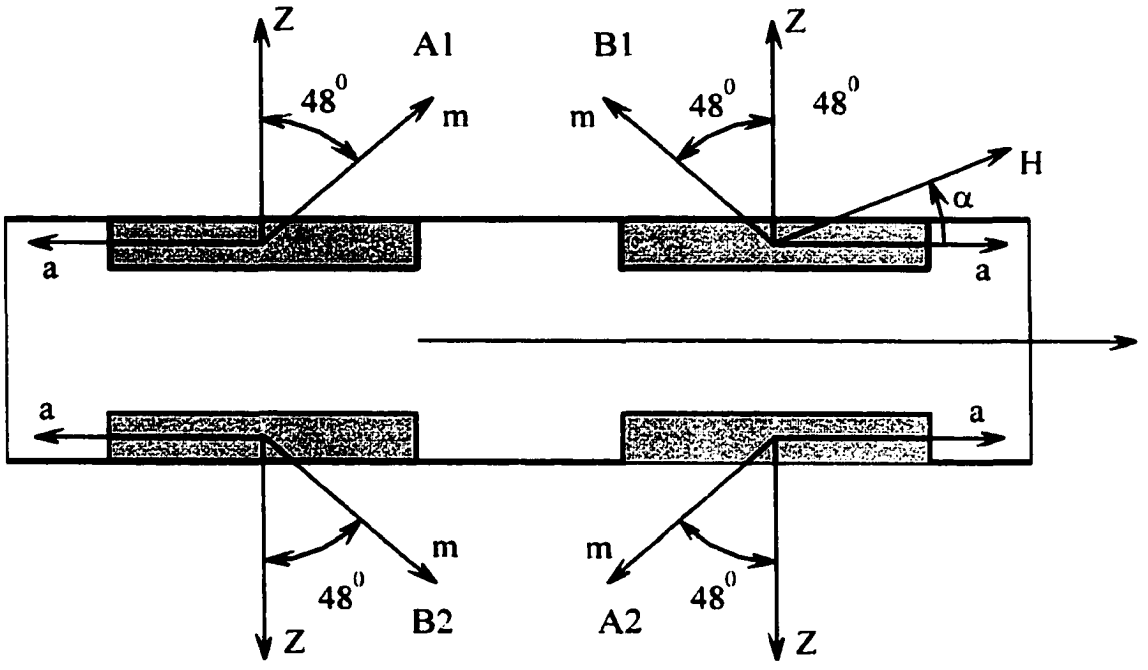

Figure 7.7. Scheme of the kaolinite-plate location along the axis of extrudated sample.

Conclusion

Experimental investigations in this dissertation makes it possible to conclude that:

1. The investigations are aimed at predicting and characterizing the thickness of nanocomposite films and measuring the thickness and physical properties of ultrathin polymer films. For this purpose we have used the SIMS method to measure surface coverage in ultra-thin films.

   AFM, SIMS, and X-ray reflectivity studies indicate that, at a dPS molecular weight of 690,000, the films approach a limiting thickness of approximately 30 Å, and then develop holes, or microvoids, with diameters on the order of 0.1 μm. Silicon is exposed within these microvoids. Spin casting represents an economical and straightforward means of creating such a nanostructured film.

2. The effects of solute concentration (in toluene), spin rate and the time of spinning on polystyrene/clay nanocomposite film thickness were examined. For uniform films ranging in thickness from 0.2μm to 10μm, thickness follows a power-law dependence on spin rate and on spinning time. For thickness versus spin rate, the power varies from -7×10^{-5} to -5×10^{-5} at low concentrations of

clay and varies around -1×10^{-4} at high concentrations of clay. The experimental time dependence of the film thickness demonstrates that solutions without clay form a dry film within 15 seconds, and for solutions with clay the drying process takes more than a minute. The dependence of solution viscosity on spin rate and on polystyrene and clay concentrations, as well as the dependence of solvent evaporation rate on polystyrene concentration, were also investigated in order to understand and model the physics of process of the nanocomposite film formation. Viscosity-concentration dependence indicates the presence of two physically different regimes (dilute and concentrated solutions). Evaporation rate-concentration dependence shows two modes of evaporation (free surface evaporation and through-crust evaporation). Addition of clay greatly reduces the evaporation rate. Numerical analysis has shown that evaporation is a dominating mechanism determining the final film thickness. Effects of viscosity are much smaller.

3. Possibilities of the EPR spectroscopy and X-ray diffraction are shown to be a new method for investigating the orientation of single crystals in the filled polymers.
4. EPR spectra of iron ions in dielectric kaolinite single crystals were investigated over a wide range (from the helium to room

temperatures). It has been shown that such temperature transformation of Fe^{3+} EPR spectrum is typical of the multiminimum systems.

5. Experimental investigation of a new model multiminimum system of Cu^{2+} in $LiGa_5O_8$ single crystals has been performed.
6. It is shown that filler crystals can be oriented in a polymer by means of hydrostatic extrusion.
7. The angular dependence of the Fe^{3+} EPR spectrum in the polymer/kaolinite nanocomposite has been for the first time investigated. A preferred direction of the kaolinite-plate orientation is observed, made visible by the direction of maxima in the angular dependence of the resonance field of EPR spectral lines.
8. A new technique of creating and investigating a preset orientation of filler crystals in polymers has been developed. To clarify the magnetic probe properties revealed in the filled polymers, a quantum-mechanical approach was applied. Properties of the magnetic probes were dependent on the nature and degree of the magnetic probe orientation in the samples of filled polymers. This has made it possible to produce samples with a preset character and degree of filler orientation.

In summary, SIMS-EPR-based methods of physical

characterization of nanolayers and nanocomposites in polymers at engineered interfaces have been developed. The EPR data are consistent with the results of X-ray diffraction obtained from the surface layers of the samples. Properties of such nanocomposites, which are widely utilized in industry, depend on the orientation of the crystals.

Bibliography.

General bibliography.

1. V. Shapovalov, F. Choudhery, Y. Strzhemechny, S. Schwarz, S. Ge, M. Rafailovich, J. Sokolov. Microvoid formation in ultrathin spin-cast polystyrene films. Abstract. Materials of Fall 1998 Materials Research Society Meeting, Boston, USA. p. 432 (1998).

2. V. Shapovalov, Y. Strzhemechny, F. Choudhery, S. A. Schwarz, S. Ge, K. Shin, J. Sokolov, and M. H. Rafailovich. Nanostructure formation in spin-cast polystyrene films. Polymer International, v. 49, p.p. 432-436 (2000).

3. V. V. Shapovalov, H. Szymczak, S. Piechota. Jahn-Teller effect in copper-doped spinel group. 7th International Conference on ferrites 1996 (Bordeaux, France, 3-6 September 1996). Abstracts, p.114 (1996).

4. V. V. Shapovalov, H. Szymczak, S. Piechota. Jahn-Teller effect in copper-doped spinel group. Journal de Physique IV, France, vol.7, p.p. C1-243÷C1-244 (1997).

5. V. N. Vasyukov, V. V. Shapovalov, H. Szymczak, S. Piechota, V. A. Shapovalov. Peculiarities of manifestation of the Jahn-Teller effect of EPR spectrum of $LiGa_5O_8:Cu^{2+}$ crystall. International symposium: Radiospectroscopy of condenced materials. Kiev, Ukraine, 17-18 June 1998. Abstracts. Kiev: NAN Ukraine, p.7 (1998).

6. V. N. Vasyukov, V. V. Shapovalov, H. Szymczak, S. Piechota, V. A. Shapovalov. Peculiarities of the Jahn-Teller effect development in the EPR spectrum of $LiGa_5O_8:Cu^{2+}$ single crystal. In the book: Radiospectroscopy of Condensed Matter (a collective monograph in two parts). Kiev, chapter 1, p. 209 (1998).

7. V. V. Shapovalov, V. Vasyukov, V. Dyakonov, V. A. Shapovalov, H. Szymczak, S. Piechota, M. M. Lukina. Observation of the Jahn-Teller temperature dependence of the integral intensity of EPR spectrum of $LiGa_5O_8:Cu^{2+}$. Abstracts of the First Regional Conference on Magnetic and Superconducting Materials (MSM-99). Sharif University of Technology, Tehran, Iran (27-30 September, 1999, p.114).

8. V. V. Shapovalov, V. Vasyukov, S. Piechota, V. A. Shapovalov, H. Szymczak, M. Ziatdinov. Tunnel split of Cu^{2+} - ion in $LiGa_5O_8$ crystal. Abstracts of II Asia-Pasific EPR/ESR Symposium (APES'99). Zhejiang University Hangzhou. China (31 October - 4 November), p. 167 (1999).

9. V. V. Shapovalov, V. N. Vasyukov, H. Szymczak, S. Piechota, V. A. Shapovalov, V. P. Dyakonov and M. M. Lukina. Development of local deformations of crystal in EPR spectrum of Cu^{2+} ion. Phys. and Techn. High. Pres., v.10, N2, 37-42, (2000) (In Ukraine).

10. E. I. Aksimentjeva, V. P. Dyakonov, V. V. Shapovalov, S. Piechota. Features of structure and physico-chemical properties of the iron (II) - 1- nitroso-2-naphtol complex. Zhurnal Obshej Khimii, v.70, N10, p.p. 1680-1684 (2000) (In Russian).

11. V. V. Shapovalov, V. Vasyukov, S. Piechota, V. A. Shapovalov, H. Szymczak, M. Ziatdinov. Tunnel split of Cu^{2+} -ion in $LiGa_5O_8$ crystal. Applied Magnetic Resonance. (In press).

12. V. N. Vasyukov, V. V. Shapovalov, S. A. Schwarz, M.H. Rafailovich, J. C. Sokolov, V. A. Shapovalov, V. A. Beloshenko. Temperature-induced changes in the EPR spectrum of the magnetic center in kaolin. Journal of Magnetic Resonance **154**, 15-21 (2002).

13. V. V. Shapovalov, V. N. Vasyukov, M. H. Rafailovich, J. C. Sokolov, S. A. Schwarz, N.-L. Yang, M.-H. Cui, V. A. Shapovalov, V. A. Beloshenko. Plastic deformation-induced orientation of kaolinite crystals in ultrahigh-molecular polyethylene. (Journal Magnetic Resonance, in press-2002).

14. V. V. Shapovalov, V. N. Vasyukov, V. A. Shapovalov. Tranzition from the low-temperature EPR spectrum to the high-temperature one for Cu^{2+} and Fe^{3+} ions in $ZnAl_2O_4$ single crystal. Abstracts "Scientific Conference of 2001", National Academy of Sciences of Ukraine, Donetsk Physics&Technical Institute, Donetsk, Ukraine (9-11 January, 2002, p.4).

Bibliography for the Preface.

1. Gleiter H. Materials with ultrafine grain size. // In: Proceeding Second Riso International Symposium on Metallurgy and Materials Science / Eds. N. Hansen, T. Leffers and H. Lilholt. Roskilde: Denmark, p.p. 15-21 (1981).

2. Birringer R., Herr U., Gleiter H., Nanocrystalline materials – a first report // Suppl. Trans. Japan. Inst. Metals, v.27. p.p.43-52 (1986).

3. Siegel R., Hahn H., Nanocrystalline Materials. In: Current Trends in the physics of Materials / Ed. M. Yussouff. Singapore: World scientific, p.403-420 (1987).

4. Siegel R., Ramasamy S., Hahn H. et. al. Synthesis, characterization and properties of nanocrystalline TiO_2 // J. Mater. Res., v.3. p. 1367-1372 (1988).

Bibliography for Chapter 1.

1. S.A. Schwarz, R.A.L. Jones, E.J. Kramer, M.H. Rafailovich, and J.C. Sokolov. SIMS depth profiling study of surface enrichment in blends of deuterated and protonated polystyrene. In book Proceedings of the Seventh International Conference on Secondary Ion Mass Spectrometry (SIMS VII). P.P.355-358 (1989).

2. S. A. Schwarz, B. J. Wilkens, M. A. A. Pudensi, M. H. Rafailovich, J. Sokolov, X. Zhao, W. Zhao, X. Zheng, T. P. Russell, R. A. L. Jones. Studies of surface and interface segregation in polymer blends by secondary ion mass spectrometry. Molecular physics, Vol. 76, No. 4, 937-950 (1992).

3. E. J. Kramer. Physica B, Vol. 173, 189 (1991).

4. P. J. Mills, P. F. Green, C. J. Palmstrom, J. W. Mayer and E. J. Kramer. Appl. Phys. Lett., Vol. 45, 958 (1984).

5. J. Sokolov, M. H. Rafailovich, R. A. L. Jones and Kramer. Appl. Phys. Lett., Vol. 54, 590 (1989).

6. S. K. Sinha. Physica B, Vol. 173, 25 (1991).

7. R. Chujo. Polym. J., Vol. 23, 367 (1991).

8. Y. M. Strzhemechny, S. A.; Schwarz, J. Schachter, M. H. Rafailovich, J. Sokolov. Secondary Ion Mass Spectrometry Study of Silicon Surface Preparation and the Polystyrene/Silicon Interface *J. Vac. Sci. Technol.*, A 15: 894-898 (1997).

9. Abragam A. and Bleaney B. Electron Paramagnetic Resonance of Transitions Ions. Clarendon Press, Oxford (1970).

10. Pryce H.M.L. Proc. Phys. Soc., A63, 25 (1950).

11. Abragam A. and Pryce H. M. L. Proc. Phys. Soc., A205, 135 (1951).

Bibliography for Chapter 2.

1. C. W. Frank, V. Rao, M. M. Despotopoulou, R. F. W. Pease, W. D. Hinsberg, R. D. Miller, and J. F. Rabolt, Structure in Thin and Ultrathin Spin-Cast Polymer Films. *Science* **273**: 912-15 (1996)

2. C. W. Extrand, Spin Coating of Very Thin Polymer Films. *Polym. Eng. Sci.* 34: 390-394 (1994)

3. L. L. Spangler, J. M. Torkelson, and J. S. Royal, Influence of Solvent and Molecular Weight on Thickness and Surface Topology of Spin-Coated Polymer Films. *Polym. Eng. Sci.* **30**: 644-653 (1990)

4. D. B. Hall, P. Underhill, and J. M. Torkelson. Spin Coating of Thin and Ultrathin Polymer Films. *Polym. Eng. Sci.* 38: 2039-2045 (1998).

5. T. G. Stange, R. Mathew, and D.F. Evans. Scanning Tunneling Microscopy and Atomic Force Microscopy Characterization of Polystyrene Spin-Coated onto Silicon Surfaces. *Langmuir* **8**: 920-926 (1992).

6. Y. M. Strzhemechny, S. A.; Schwarz, J. Schachter, M. H. Rafailovich, J. Sokolov. Secondary Ion Mass Spectrometry Study of Silicon Surface Preparation and

the Polystyrene/Silicon Interface *J. Vac. Sci. Technol.*, **A 15:** 894-898 (1997).

7. S.A. Schwarz, B.J. Wilkens, M.A.A. Pudensi, M.H. Rafailovich, J. Sokolov, X. Zhao, W. Zhao, X. Zheng, T.P. Russell, and R.A.L. Jones. Studies of Surface and Interface Segregation in Polymer Blends by Secondary Ion Mass Spectroscopy. *Molec. Phys.* **76:** 937-950 (1992).

8. J. Gu, M. D. Bullwinkel, and G. A. Campbell. Measurement and Modeling of Solvent Removal for Spin Coating. *Polym. Eng. Sci.* **36:** 1019-1026 (1996).

9. G. R. Strolb. The Physics of Polymers. Springer -Vetrlag , New York. p 64-65 (1996).

10. M.Daoud, J.P.Cotton, B.Farnoux, G.Jannink, G.Sarma, H.Benoit, R.Duplessix, C.Picot, and P.G. de Genne. Solution of Flexible Polymers. Neutron Experiments and Interpretation. *Macromolecules* 8: 804-818 (1975).

Bibliography for Chapter 3.

1. V. Shapovalov, V. S. Zaitsev, Yu. Strzhemechny, F. Choudhery, W.Zhao, S. A. Schwarz, S. Ge, K.-W. Shin, J. C. Sokolov, M. H.Rafailovich. Nanostructure Formation in Spin-Cast Polystyrene Films. *Polymer International* **49**: 432-436 (2000)

2.C. W. Frank, V. Rao, M. M. Despotopoulou, R. F. W. Pease, W. D. Hinsberg, R. D. Miller, and J. F. Rabolt, Structure in Thin and Ultrathin Spin-Cast Polymer Films. *Science* **273**: 912-15 (1996)

3.L.L.Spangler, J.M.Torkelson, and J.S.Royal, Influence of Solvent and Molecular Weight on Thickness and Surface Topology of Spin-Coated Polymer Films. *Polym.Eng.Sci.* **30**: 644-653 (1990)

4. M. Alexandre, P. Dubois. Polymer-layered silicate nanocomposites: preparation, properties and uses of a new class of materials. *Materials Science and Engineering*, **28**: 1-63 (2000).

5. R.K. Yonkoski, D.S. Soane. Model for spin coating in microelectronic applications. *J. Appl. Phys.* **72** (2), 725-740

6. J.R. Fried. *Polymer Science and Technology*. Prentice Hall, NJ, 1995. pp. 392-394, 412.

7. P.C. Painter, M.M. Coleman. *Fundamentals of Polymer Science*. Technomic Publishing Company, PA, 1994. pp. 387-391

8. P. D. de Gennes. Solvent evaporation of spin cast films: "crust" effects. *The European Physical Journal E*. **7**: 31-34 (2002)

9. D.E.Haas, J.N. Quaijada, S.J. Picone, D.P. Birnie. Effects of solvent evaporation rate on "skin" formation during spin coating of complex solutions. In SPIE Proc. 3943, Sol-Gel Optics V, B.Dunn, E. Pope, H. K. Schmidt, and M. Yamane, Editors, (2000) 280- 284

10. D.Meerhofer. Characteristics of resist films produced by spinning. *J. Appl. Phys.*, **49**(7), July 1978, pp. 3993-3997.

11. C.W.Extrand, Spin Coating of Very Thin Polymer Films. *Polym.Eng.Sci.* **34**: 390-394 (1994)

Bibliography for Chapter 4.

1. Shapovalov V., Szymczak H., Piechota C., Borowiec M. Jahn-Teller effect in $LiGa_5O_8$ spinel. Molec. Phys. Rep. **5**, 256-260 (1994).

2. Bersuker I.B. Spin inversion levels in a magnetic field and the EPR spectrum of octahedral Cu^{2+} ion complexes. Zh. Exp. Theor. Phys. **44**, 1239-1247 (1963).

3. Ham F. S. : Effect of Linear Jahn-Teller Coupling on Paramagnetic Resonance in ^2E State. Phys.Rev. **166**, 307 (1968).

4. Abragam A., Bleaney B. : Electron paramagnetic resonance of transition ions. (Clarendon Press, Oxford), **V.2,** P.P.350 (1970).

5. Bersuker I. B. : Spin Inversion Levels in a Magnetic Field and the EPR Spectrum of Octahedral Cu^{2+} Ion Complexes. Zh. Exp. Theor. Phys. **44**, 1239 (1963).

6. O'Brien M. C. M. : The Dynamic Jahn-Teller Effect in Octahedrally Co-ordinated d^9 ions. Proc. Roy. Soc. **281**, 323 (1964).

7. Lukin S. N. : Influence of linear compression and temperature at EPR of the Jahn-Teller's sistem Cu^{2+}: $ZnSiF_6 \times 6H_2O$. FTT **339**, 47 (1991).

8. Moate C. P., O'Brien M. C. M., Dunn J. L., Bates C. A., Liu Y. M. and Polinger V. Z. : $H \otimes h$ a Jahn-Teller Coupling that Really does Reduce the Degeneracy of the Ground State. Phys. Rev. Lett., **77**, 4362 (1996).

9. Kozhukhar A. Yu., Lukin S. N. and Tsintsadze G. A. : Exchange pairs of Cu^{2+} ions in zinc fluosilicate. Fiz. Nizk. Temp., **1**, 1535 (1975).

10. Joubert J. C., Brunel M., Waintal A.: A. Durif Comp. Rend. **256**, 5324 (1963).

11. Vasyukov V. N.: Dependence of the Low Temperature EPR Spectrum of Cu^{2+} Ion on the Microwave Field Frequency and Temperature. Phys. stat. sol. (b) **137**, 623 (1986).

12. Vasyukov V. N., Suharevskij B. Ya. : The Energy Spectrum of Vibronic States of Jahn-Teller's Ion. Fiz. Nizk. Temp. **20**, 821 (1994).

Bibliography for Chapter 5.

1. E. G. Howard, R. D. Lipscomb, R. N. MacDonald, B. L. Glazar, C. W. Tullock and J. W. Collete, Homogeneous Composites of Ultrahigh Molecular Weight Polyethylene and Minerals. 1.Synthesis, Ind. Eng. Chem. Product. Research and Development **20**, 421-428 (1981).

2. Y. T. Lim and O. Ok Park, Rheological evidence for the microstructure of intercalated polymer/layered silicate nanocomposites, Macromol. Rapid Commun. **21**, 231-235 (2000).

3. M. Alexandre and P.Dubois, Polymer – layered silicate nanocomposites: preparation, properties and uses of a new class of materials, Materials Science and Engineering **28,** 1-63 (2000).

4. V. A. Beloshenko, G. V. Kozlov, V. N. Varyuhin and V. G. Slobodina, Properties of ultra - high-molecular polyethylene and related polimerization-filled composites produced by solid-state extrusion, Acta Polimer **48,** 181-187 (1997).

5. Ultra – high modulus polymers. Edited by a Ciferri and I. M. Ward. Applied Science Publishers. London. (1979).

6. Hugo Strunz, Mineralogische tabellen, Leipzig, Academische Verlagsgesellschaft Geest, Portig K.-G., P.P. 532 (1957).

7. Alexander Newton Winchell and Horace Winchell. The microscopical characters of artificial inorganic solid substances: optical properties of artificial minerals. Academic Press, New York and London, P.P. 402 (1964).

8. R. L. Adelman, E. G. Howard, Pat. 41511226, USA.

9.V.V. Mank, F.D. Ovcharenko, L.V. Golovko, N.G. Vasilyev and A.Ya. Karushkina, On nature of stable radicals in kaolin, DAN SSSR **223**, 389-392 (1975).

10. V. N. Vasyukov, V. V. Shapovalov, S. A. Schwarz, M.H. Rafailovich, J. C. Sokolov, V. A. Shapovalov, V. A. Beloshenko. Temperature-induced changes in the EPR spectrum of the magnetic center in kaolin. Journal of Magnetic Resonance **154**, 15-21 (2002).

11. V. V. Shapovalov, V. N. Vasyukov, M. H. Rafailovich, J. C. Sokolov, S. A. Schwarz, Nan-Loh Yang, V. A. Shapovalov, V. A. Beloshenko. Plastic deformation-induced orientation of kaolinite crystals in ultrahigh-molecular polyethylene. (Journal Magnetic Resonance, in press-2002).

Bibliography for Chapter 6.

1. E. G. Howard, R. D. Lipscomb, R. N. MacDonald, B.L. Glazar, C. W. Tullock and J. W. Collete, Homogeneous Composites of Ultrahigh Molecular Weight Polyethylene and Minerals. 1.Synthesis, Ind. Eng. Chem. Product. Research and Development **20**, 421-428 (1981).

2. Y. T. Lim and O. Ok Park, Rheological evidence for the microstructure of intercalated polymer/layered silicate nanocomposites, Macromol. Rapid Commun. **21**, 231-235 (2000).

3. M. Alexandre and P.Dubois, Polymer – layered silicate nanocomposites: preparation, properties and uses of a new class of materials, Materials Science and Engineering **28,** 1-63 (2000).

4. V. A. Beloshenko, G. V. Kozlov, V. N. Varyuhin and V. G. Slobodina, Properties of ultra-high-molecular polyethylene and related polimerization-filled composites produced by solid-state extrusion, Acta Polimer **48,** 181-187 (1997).

5. V. N. Vasyukov, V. P. Dyakonov, V. A. Shapovalov, E. I. Aksimentyeva, H. Szymczak and S. Piechota, Temperature-induced change in the ESR spectrum of the Fe^{3+} ion in polyaniline, Low Temperature Physics **26**, 265-269 (2000).

6. V. N. Vasyukov, Dependence of the low temperature EPR spectrum of Cu^{2+} ion on the microwave field frequency and temperature, Physica status solidi (b) **137**, 623-631. (1986).

7. V. N. Vasyukov and B. Ya. Suharevskii, Energy spectrum of vibronic states of a Jahn-Teller ion, Low Temperature Physics **20** (8), 644-652 (1994).

8. A. V. Leontyeva, G. A. Marinin and A. Yu. Prohorov, Influence of intermoleculari interaction features on inelastic properties of crystalline methane, Zurn. Fiz. Himii **68,** 975-978 (1994) (in Russian).

9. G.B. Bokii, Kristallohimiya, pp. 255, "Nauka", Moskva (1971) (in Russian).

10. V. N. Mank, F. D. Ovcharenko and L. S. Sonkin, Study of the state of iron in kaoline by the EPR method, DAN SSSR **233,** 675-678 (1977).

11. V. V. Mank, F. D. Ovcharenko, L. V. Golovko, N. G. Vasilyev and A. Ya. Karushkina, On nature of stable radicals in kaolin, DAN SSSR **223**, 389-392 (1975).

12. E. Burzo, M. Chipara, D. Ungur and I. Ardelean, Electron Paramagnetic Resonance Study of xFe_2O_3 (1-x)[B_2O_3 PbO] Glasses, Phys. Stat. Solidi (b) **124**, K117-K120 (1984).

13. R. Singh, Effect of Fe ions on electrical conductivity and ESR in tellurium-vanadate glasses, J. Phys.D: Appl. Phys **17**, L57-L60 (1984).

14. C. S. Sunandana and R. Jagannathan, ESR and Messbauer Studies of Fe^{3+} ion in calcium boro-aluminate glasses, Solid State Communications **53**, 985-988 (1985).

15. A. Montenero, M. Friggeri, D.C. Giori, N. Belkhiria and L.D. Pye, Iron-soda-silica glasses: preparation, properties, structure, J. Non-Crystalline Solids **84**, 45-60 (1986).

16. J. Komnsinski, L. Stoch and S.M. Dubiel, Application of Electron Paramagnetic Resonance and Mossbauer Spectroscopy in the Investigation of Kaolinite-group Minerals, Clays and Clay Miner. **29,** 23-30 (1981).

17. Ya. G. Klyava, EPR spectroscopy of disordered solids, pp. 320, "Zinatne", Riga (1988).

Bibliography for Chapter 7.

1. E. G. Howard, R. D. Lipscomb, R.N. MacDonald, B. L. Glazar, C.W. Tullock and J.W. Collete, Homogenious Composites of Ultrahigh Moleqular Weight Polyethilene and Minerals.1.Synthesis, Ind. Eng. Chem. Product. Research and Development **20**, 421-428 (1981).

2. Y. T. Lim and O. Ok Park, Rheological evidence for the microstructure of intercalated polymer/layered silicate nanocomposites, Macromol. Rapid Commun. **21**, 231-235 (2000).

3. M. Alexandre and P.Dubois, Polymer – layered silicate nanocomposites: preparation, properties and uses of a new class of materials, Materials Science and Engineering **28,** 1-63 (2000).

4. V. A. Beloshenko, G. V. Kozlov, V. N. Varyuhin and V. G. Slobodina, Properties of ultra -high-molecular polyethylene and related polimerization-filled composites produced by solid-state extrusion, Acta Polimer **48,** 181-187 (1997).

5. V. A. Druts and A. A. Kashaev, X-ray diffraction investigation of kaolinite single crystal, Kristallographiya **5**, 224-227 (1960).

6. R. B. Dow, Inhibition of crystallization of rubber by high pressure, J. Chem. Phys. **7,** 201-206 (1939).

7. W. Parks and R. B. Richards, The effect of pressure on the volume thermodynamic properties and crystallinity of polyethylene, Trans. Faradey Soc. **45**, 203-211 (1949).

8. C. E. Weir, Compressibility of natural and synthetic high polymers at high pressure, J. Res. Natl. Bur. Stand. **46**, 207-212 (1951).

9. C. E. Weir, Transitions and phases of polytetrafluoroethylene, J. Res. Natl. Bur. Stand. **50**, 95-97 (1953).

10. P. W. Bridgman, The effect of pressure on the tensile properties of several metals and other materials, J. Appl. Phys. **24**, 560-570 (1953).

11. K. D. Pae and S. K. Bhateja, The effect of hydrostatic pressure on the mechanical behavior of polymers, J. Macromol. Sci. C **13**, 1-75 (1975).

12. S. K. Bhateja and K. D. Pae, The effect of hydrostatic pressure on the compressibility, crystallization and melting of polymers, J. Macromol. Sci. C **13**, 77-133 (1975).

13. K. Kishore and R. Vasanthakumari, A comprehensive review of the effect of pressure on polymer crystallization, High Temp. – High Pres. **16**, 241-268 (1984).

14. E. V. Prut, Application of high pressure in polymer processing, High – pressure Chemistry and Physics of Polymers (Ed. by A. L. Kovarskii), Bosa Raton: CRC Press, P.P. 341-346 (1994).

15. Ultra – high modulus polymers. Edited by A. Ciferri and I. M. Ward. Applied Science Publishers. London, P.P.271 (1979).

16. R. L. Adelman, E. G. Howard. Pat. 41511226, USA.

17. V. V. Mank, F. D. Ovcharenko, L. V. Golovko, N. G. Vasilyev and A. Ya. Karushkina, On nature of stable radicals in kaolin, DAN SSSR **223**, 389-392 (1975).

18. Ya. G. Klyava, EPR spectroscopy of disordered solids, "Zinatne", Riga, P.P. 320 (1988).

19. V. N. Vasyukov, V. P. Dyakonov, V. A. Shapovalov, E. I. Aksimentyeva, H. Szymczak and S. Piechota, Low Temperature Physics **26**, 265-269 (2000).